Supplementary Information

Magnetic Hysteresis and Large Coercivity in Bisbenzimidazole Radical-Bridged Dilanthanide Complexes

Florian Benner,[a] Léo La Droitte,[b] Olivier Cador,[b] Boris Le Guennic,[b] and Selvan Demir[a]*

[a]Department of Chemistry, Michigan State University, 578 South Shaw Lane, East Lansing, Michigan 48824, USA.
[b]Univ Rennes, CNRS, ISCR (Institut des Sciences Chimiques de Rennes) - UMR 6226, F-35000 Rennes, France.

*Correspondence to: sdemir@chemistry.msu.edu

Chem. Sci.

Table of Contents

Crystallographic Data and Structural Refinements

Table S1. Crystallographic Data and Structural Refinement of $[(Cp^*_2Gd)_2(\mu\text{-Bbim})] \bullet x$ toluene, **1-Ln** (Ln = Gd, Tb, x = 2; Ln = Dy, x =1).

	1-Gd	**1-Tb**	**1-Dy**
Empirical formula	$C_{68}H_{84}Gd_2N_4$	$C_{68}H_{84}N_4Tb_2$	$C_{61}H_{76}Dy_2N_4$
Formula weight (g/mol)	1271.89	1275.23	1190.25
Temperature (K)	99.99(10)	100.00(10)	173.15
Crystal system	monoclinic	monoclinic	triclinic
Space group	*C*2/m	*C*2/m	*P*−1
a (Å)	15.5900(2)	27.9083(18)	10.5529(6)
b (Å)	13.65900(10)	13.6251(2)	11.0230(6)
c (Å)	15.5654(2)	15.5343(10)	12.4361(7)
α (°)	90	90	67.7720(10)
β (°)	116.3370(10)	149.942(18)	87.5370(10)
γ (°)	90	90	79.1990(10)
Volume (Å^3)	2970.50(6)	2958.7(8)	1314.78(13)
Z	2	2	1
ρ_{calc} (g/cm^3)	1.422	1.431	1.503
μ (mm^{-1})	14.601	11.915	2.862
F(000)	1296.0	1300.0	602.0
Crystal size (mm^3)	0.122 × 0.1 × 0.035	0.113 × 0.055 × 0.055	0.277 × 0.157 × 0.153
Radiation	CuK_α (λ = 1.54184)	CuK_α (λ = 1.54184)	MoK_α (λ = 0.71073)
2*Θ* range for data collection (°)	6.336 to 154.026	6.348 to 154.416	3.54 to 52.8
Index ranges	−19 ≤ *h* ≤ 19, −14 ≤ *k* ≤ 17, −19 ≤ *l* ≤ 19	−35 ≤ *h* ≤ 35, −17 ≤ *k* ≤ 13, −19 ≤ *l* ≤ 19	−13 ≤ *h* ≤ 13, −13 ≤ *k* ≤ 13, −15 ≤ *l* ≤ 15
Reflections collected	10923	11155	10374
Independent reflections	3184 [R_{int} = 0.0244, R_σ = 0.0231]	3155 [R_{int} = 0.0256, R_σ = 0.0230]	5366 [R_{int} = 0.0137, R_σ = 0.0191]
Data/restraints/parameters	3184/0/243	3155/0/243	5366/0/310
Goodness-of-fit on F^2	1.103	1.100	1.074
Final *R* indexes [*I*>=2*σ* (*I*)]	R_1 = 0.0240, wR_2 = 0.0610	R_1 = 0.0251, wR_2 = 0.0617	R_1 = 0.0194, wR_2 = 0.0464
Final *R* indexes [all data]	R_1 = 0.0246, wR_2 = 0.0613	R_1 = 0.0258, wR_2 = 0.0620	R_1 = 0.0205, wR_2 = 0.0475
Largest diff. peak/hole (e Å^{-3})	0.40/-0.62	0.44/-0.85	1.38/−0.59

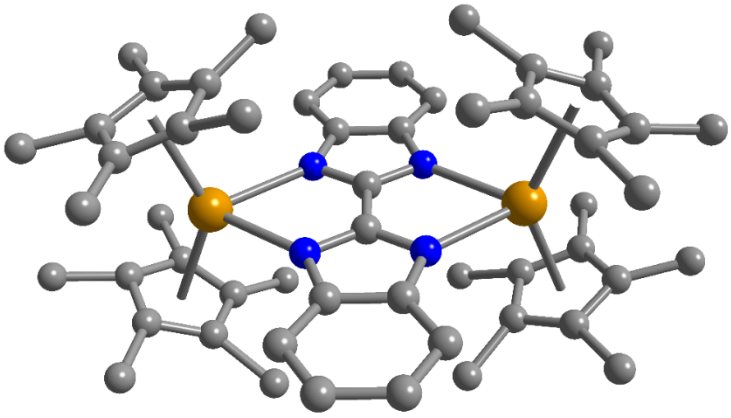

Figure S1. Structure of **1-Gd.** Orange, gray, and blue spheres represent gadolinium, carbon, and nitrogen atoms, respectively. All hydrogen atoms, toluene solvent molecules and disorder parts on the Cp* ligands are omitted for clarity.

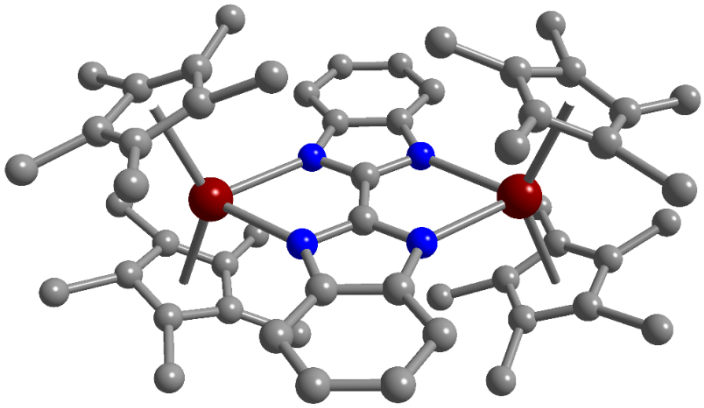

Figure S2. Structure of **1-Tb.** Dark red, grey, and blue spheres represent gadolinium, carbon, and nitrogen atoms, respectively. All hydrogen atoms, toluene solvent molecules and disorder parts on the Cp* ligands are omitted for clarity.

Table S2. Crystallographic Data and Structural Refinement of [K(crypt-222)][(Cp*$_2$Ln)$_2$(μ-Bbim$^{\bullet}$)] • 3 THF, **2-Ln** (Ln = Gd, Tb, Dy).

	2-Gd	**2-Tb**	**2-Dy**
Empirical formula	$C_{84}H_{128}Gd_2KN_6O_9$	$C_{84}H_{127}KN_6O_9Tb_2$	$C_{84}H_{128}Dy_2KN_6O_9$
Formula weight (g/mol)	1719.52	1721.85	1730.02
Temperature (K)	100.15	100.00(10)	173(2)
Crystal system	triclinic	triclinic	triclinic
Space group	*P*–1	*P*–1	*P*–1
a (Å)	13.00780(10)	12.99810(10)	13.0586(2)
b (Å)	18.0377(2)	18.0236(2)	18.1083(3)
c (Å)	18.9498(2)	18.9237(2)	18.9686(2)
α (°)	81.5150(10)	81.6460(10)	81.4010(10)
β (°)	81.5720(10)	81.5260(10)	80.9190(10)
γ (°)	74.8530(10)	74.9200(10)	74.9370(10)
Volume (Å^3)	4217.51(8)	4207.27(8)	4249.30(11)
Z	2	2	2
ρ_{calc} (g/cm^3)	1.354	1.359	1.352
μ (mm^{-1})	1.665	1.773	1.850
F(000)	1786.0	1788.0	1794.0
Crystal size (mm^3)	0.59 × 0.313 × 0.269	0.362 × 0.159 × 0.131	0.159 × 0.148 × 0.144
Radiation	MoK$_\alpha$ (λ = 0.71073)	MoK$_\alpha$ (λ = 0.71073)	MoK$_\alpha$ (λ = 0.71073)
2Θ range for data collection (°)	4.932 to 61.91	4.136 to 62.004	3.256 to 52.744
Index ranges	−18 ≤ *h* ≤ 18, −26 ≤ *k* ≤ 25, −27 ≤ *l* ≤ 27	−17 ≤ *h* ≤ 18, −24 ≤ *k* ≤ 26, −27 ≤ *l* ≤ 23	−16 ≤ *h* ≤ 16, −22 ≤ *k* ≤ 22, −23 ≤ *l* ≤ 23
Reflections collected	78556	79545	73354
Independent reflections	21844 [R_{int} = 0.0360, R_σ = 0.0362]	21689 [R_{int} = 0.0359, R_σ = 0.0366]	17324 [R_{int} = 0.0354, R_σ = 0.0233]
Data/restraints/parameters	21844/42/978	21689/0/921	17324/33/856
Goodness-of-fit on F^2	1.063	1.117	1.103
Final *R* indexes [*I*>=2σ (*I*)]	R_1 = 0.0402, wR_2 = 0.1003	R_1 = 0.0575, wR_2 = 0.1417	R_1 = 0.0513, wR_2 = 0.1308
Final *R* indexes [all data]	R_1 = 0.0483, wR_2 = 0.1047	R_1 = 0.0698, wR_2 = 0.1584	R_1 = 0.0561, wR_2 = 0.1338
Largest diff. peak/hole (e Å^{-3})	4.83/−2.51	9.65/−6.48	2.11/−0.80

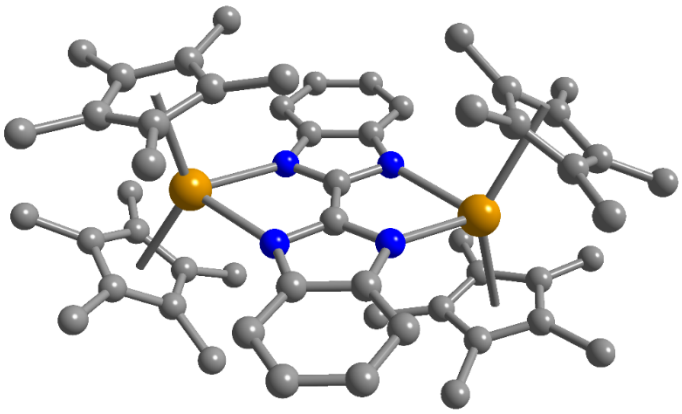

Figure S3. Structure of the $[(Cp^*_2Gd)_2(\mu\text{-}Bbim^{\bullet})]^-$ anion in a crystal of **2-Gd**. Orange, gray, and blue spheres represent gadolinium, carbon, and nitrogen atoms, respectively. All hydrogen atoms, THF solvent molecules and the $[K(crypt\text{-}222)]^+$ counterion are omitted for clarity.

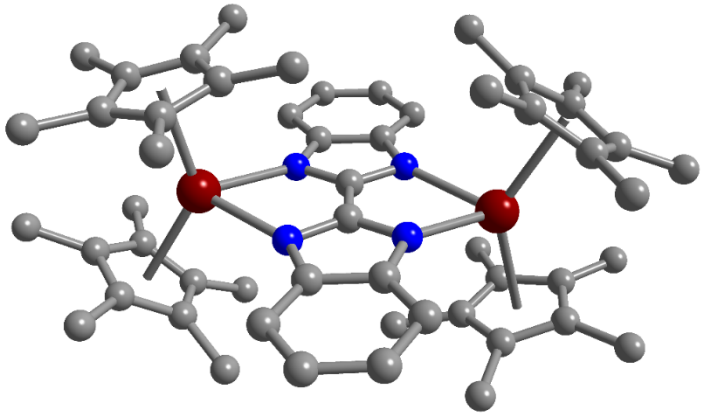

Figure S4. Structure of the $[(Cp^*_2Tb)_2(\mu\text{-}Bbim^{\bullet})]^-$ anion in a crystal of **2-Tb**. Dark red, gray, and blue spheres represent terbium, carbon, and nitrogen atoms, respectively. All hydrogen atoms, THF solvent molecules and the $[K(crypt\text{-}222)]^+$ counterion are omitted for clarity.

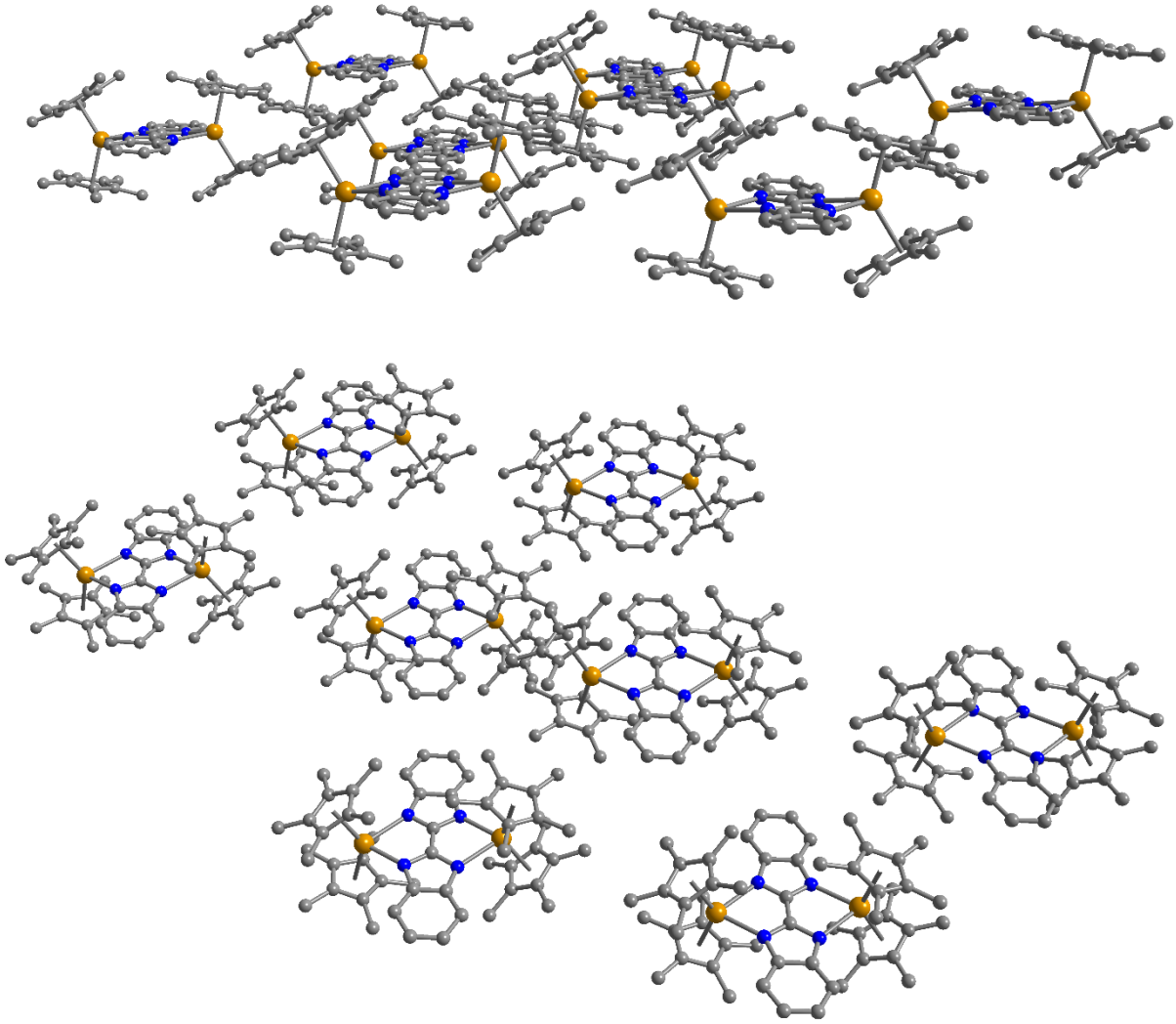

Figure S5. Packing diagram of the $[(Cp^*_2Gd)_2(\mu\text{-}Bbim^{\bullet})]^-$ anions in a crystal of **2-Gd** in front (top) and top view (bottom). Orange, gray, and blue spheres represent gadolinium, carbon, and nitrogen atoms, respectively. All hydrogen atoms, THF solvent molecules and the $[K(crypt\text{-}222)]^+$ counterion are omitted for clarity.

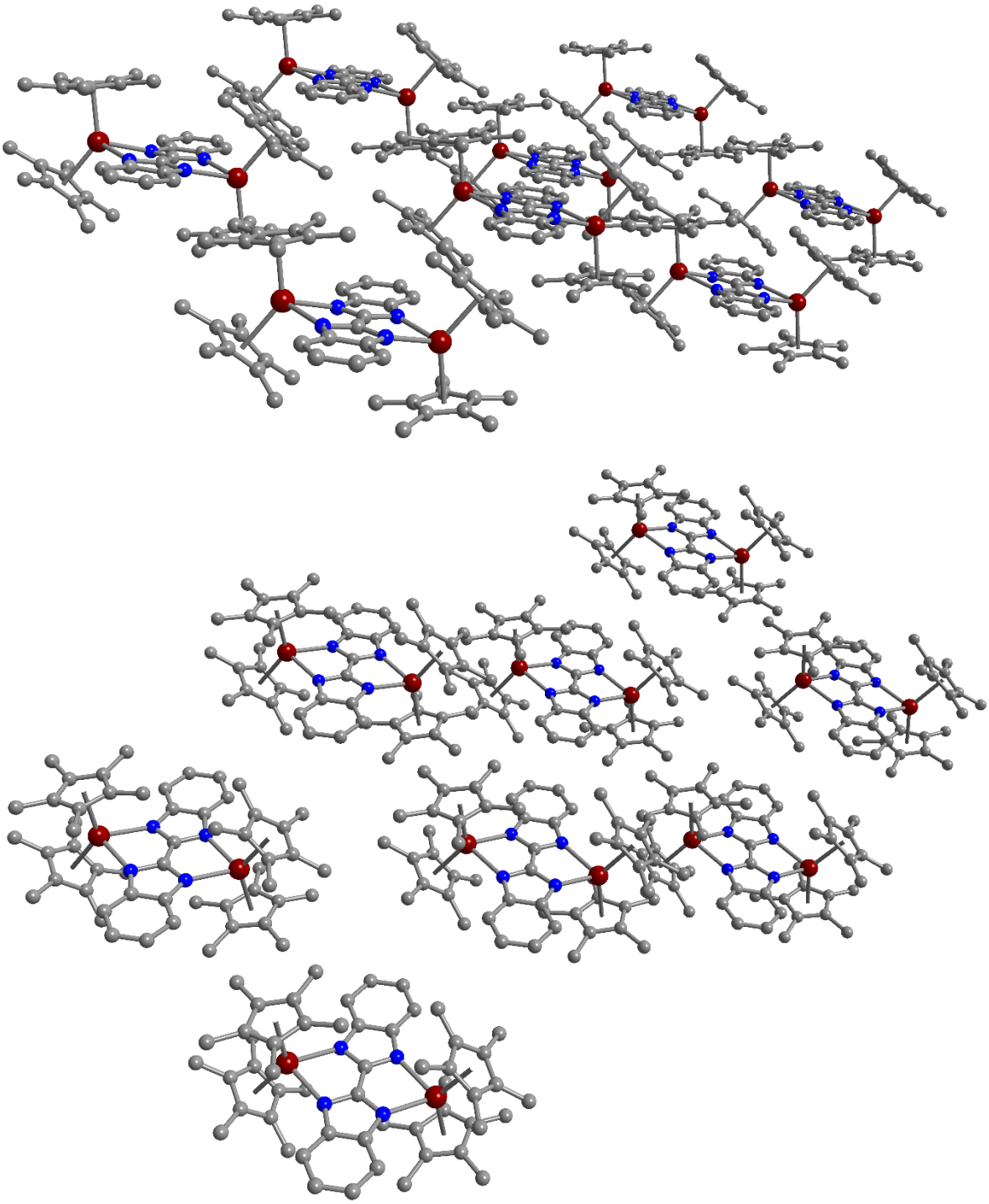

Figure S6. Packing diagram of the $[(Cp^*_2Tb)_2(\mu\text{-}Bbim^{\bullet})]^-$ anions in a crystal of **2-Tb** in front (top) and top view (bottom). Red, gray, and blue spheres represent terbium, carbon, and nitrogen atoms, respectively. All hydrogen atoms, THF solvent molecules and the $[K(crypt\text{-}222)]^+$ counterion are omitted for clarity.

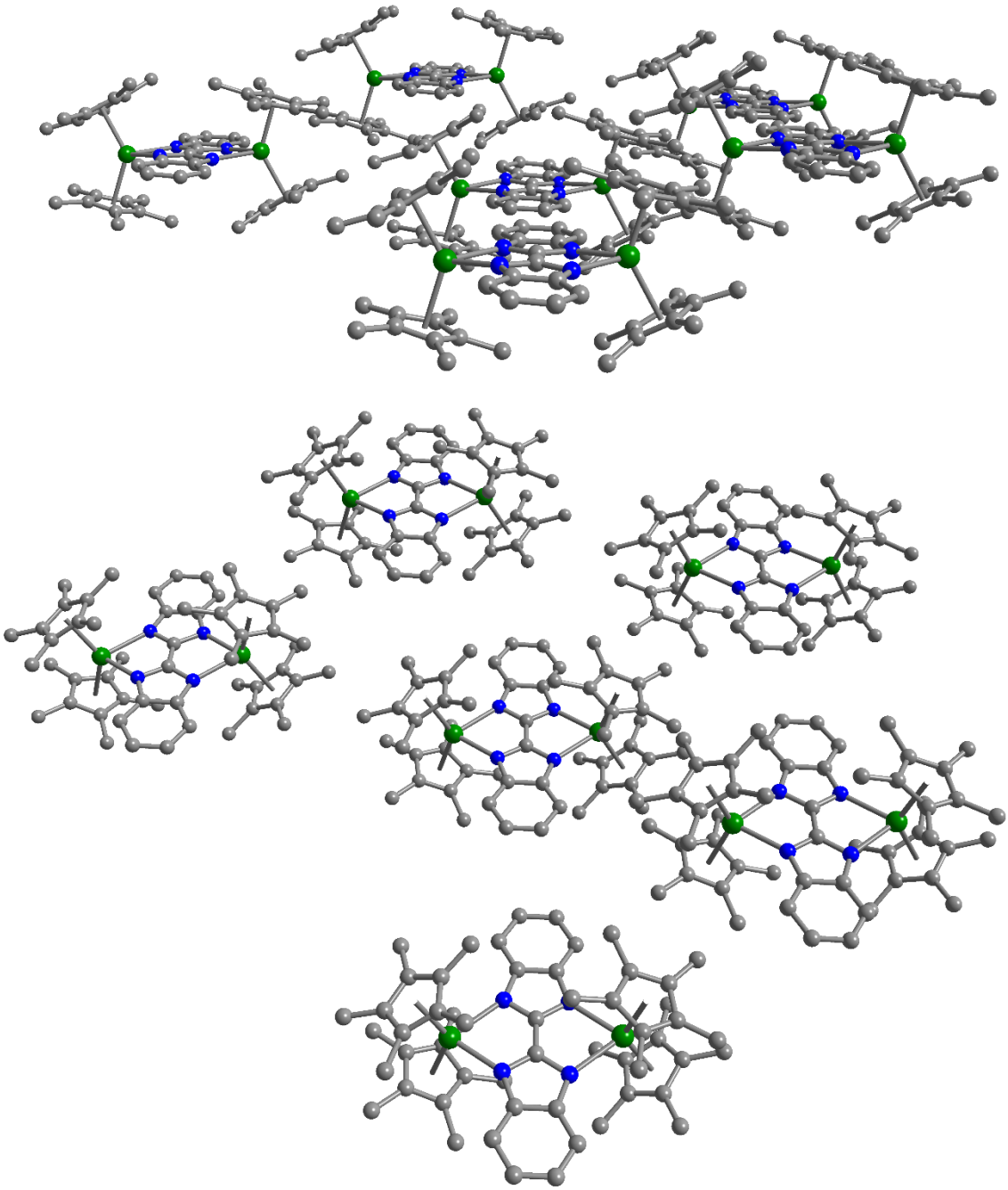

Figure S7. Packing diagram of the $[(Cp^*_2Dy)_2(\mu\text{-}Bbim^{\bullet})]^{-}$ anions in a crystal of **2-Dy** in front (top) and top view (bottom). Green, gray, and blue spheres represent dysprosium, carbon, and nitrogen atoms, respectively. All hydrogen atoms, THF solvent molecules and the $[K(crypt\text{-}222)]^{+}$ counterion are omitted for clarity.

IR Spectroscopy

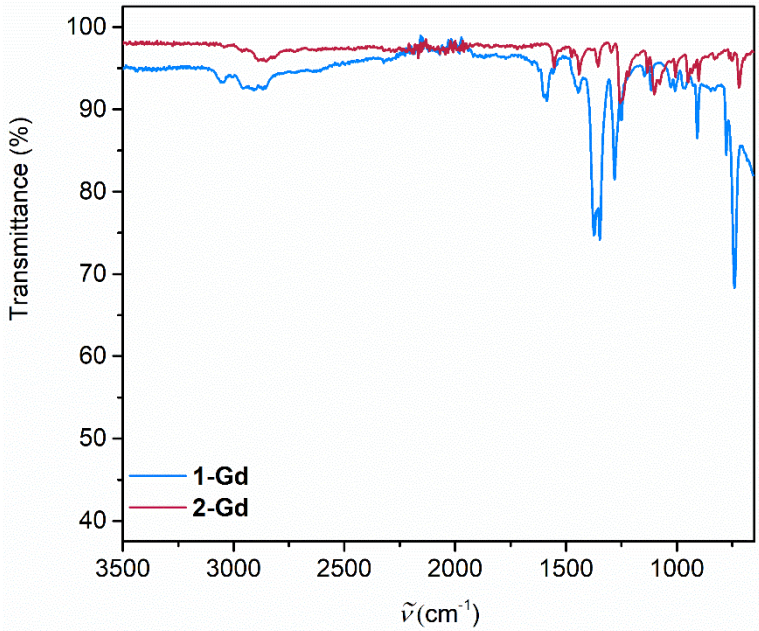

Figure S8. FTIR spectra of [(Cp*$_2$Gd)$_2$(μ-Bbim)], **1-Gd** (blue) and [K(crypt-222)][(Cp*$_2$Gd)$_2$(μ-Bbim$^{\bullet}$)], **2-Gd**, (red).

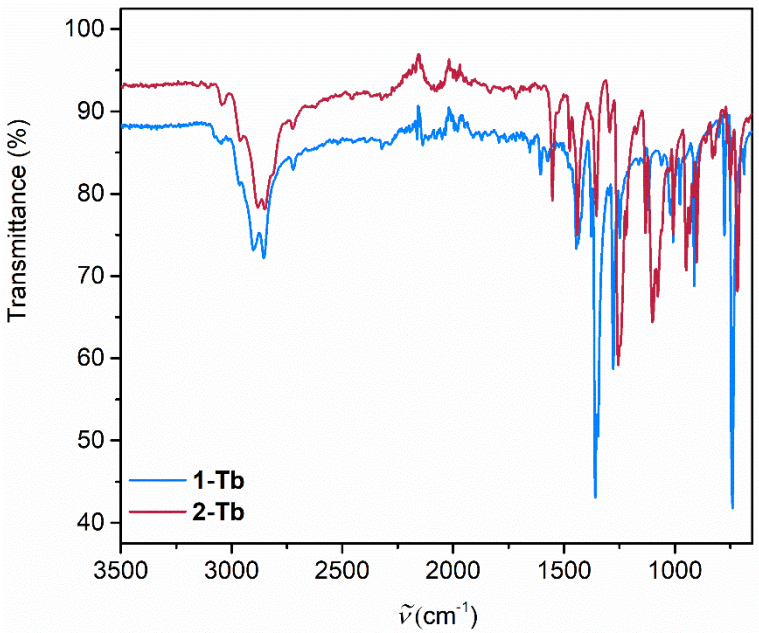

Figure S9. FTIR spectra of [(Cp*$_2$Tb)$_2$(μ-Bbim)], **1-Tb** (blue) and [K(crypt-222)][(Cp*$_2$Tb)$_2$(μ-Bbim$^{\bullet}$)], **2-Tb**, (red).

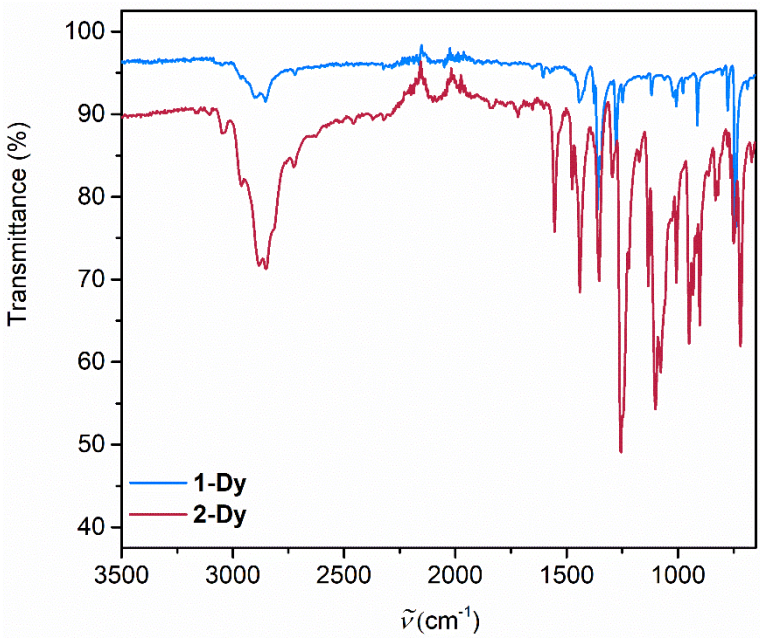

Figure S10. FTIR spectra of [(Cp*$_2$Dy)$_2$(μ-Bbim)], **1-Dy** (blue) and [K(crypt-222)][(Cp*$_2$Dy)$_2$(μ-Bbim$^{\bullet}$)], **2-Dy**, (red).

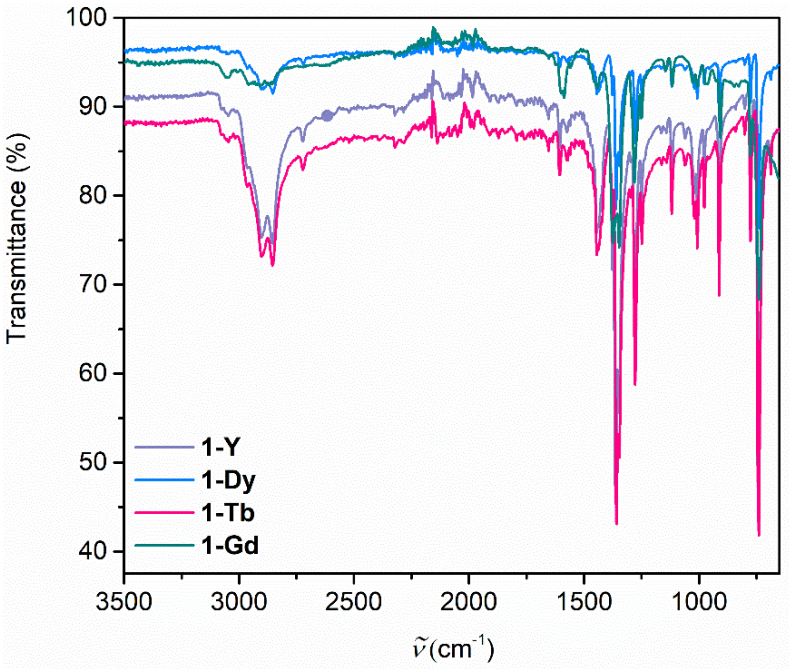

Figure S11. Stacked FTIR spectra of [(Cp*$_2$Ln)$_2$(μ-Bbim)], **1-Ln** (Ln = Y (gray),[1] Gd (turquoise), Tb (pink), Dy (blue)).

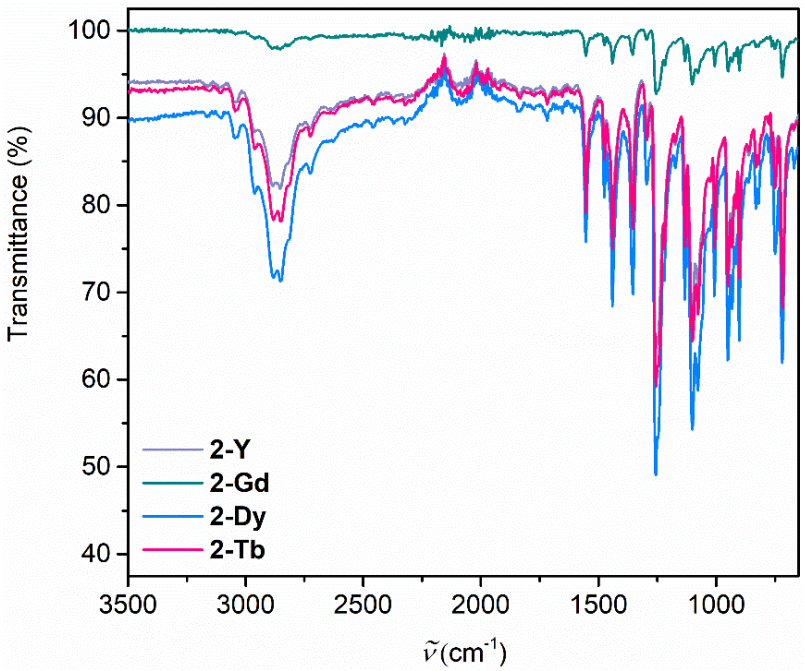

Figure S12. Stacked FTIR spectra [K(crypt-222)][(Cp*$_2$Ln)$_2$(μ-Bbim$^{•}$)], **2-Ln** (Ln = Y (gray),[1] Gd (turquoise), Tb (pink), Dy (blue)).

UV/Vis Spectroscopy

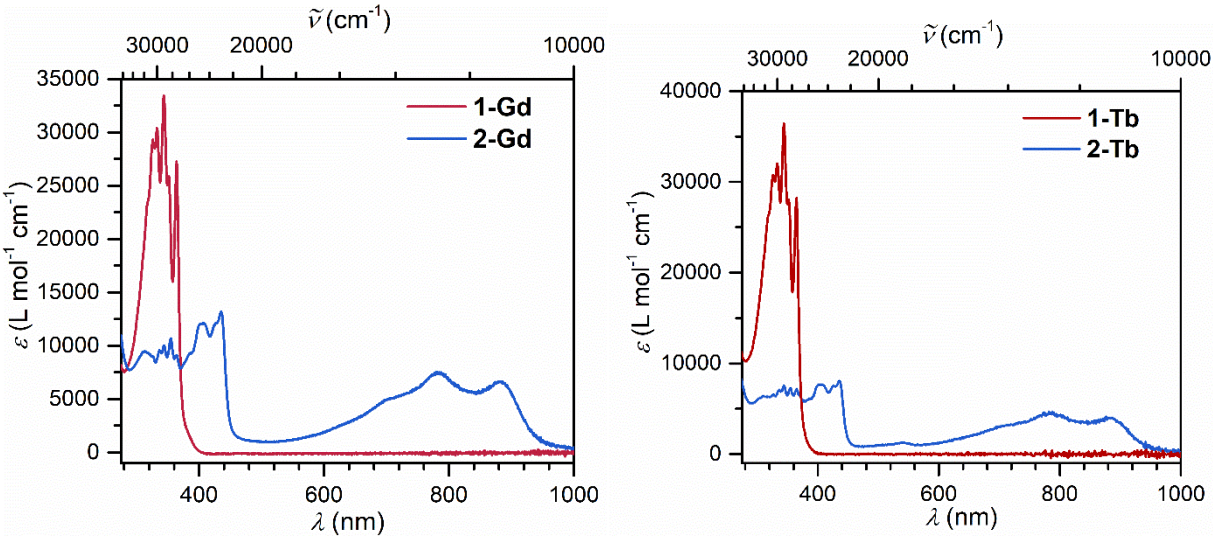

Figure S13. Left: UV/Vis spectra of [(Cp*$_2$Gd)$_2$(μ-Bbim)] (**1-Gd**, in blue) and [K(crypt-222)][(Cp*$_2$Gd)$_2$(μ-Bbim$^•$)] (**2-Gd**, in red), taken in THF. Right: UV/Vis spectra of [(Cp*$_2$Tb)$_2$(μ-Bbim$^•$)] (**1-Tb**, in blue) and [K(crypt-222)][(Cp*$_2$Tb)$_2$(μ-Bbim$^•$)] (**2-Tb**, in red), taken in THF. Concentrations: **1-Gd**: 2.636 x 10^{-5} mol/L, **1-Tb**: 1.389x 10^{-5} mol/L, **2-Gd**: 3.198 x 10^{-5} mol/L, **2-Tb**: 2.307 x 10^{-5} mol/L.

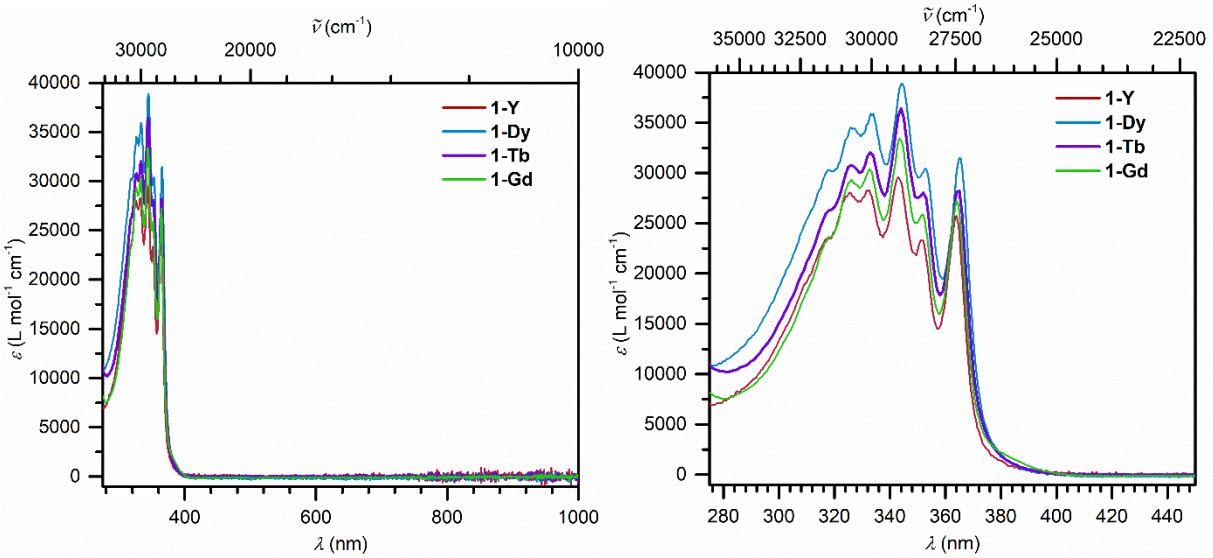

Figure S14. Left: Superimposed UV/Vis spectra of [(Cp*$_2$Ln)$_2$(μ-Bbim)] (**1-Ln**, Y (red),[1] Gd (green), Tb (purple), Dy(blue)). Right: Magnification of superimposed UV/Vis spectra of [(Cp*$_2$Ln)$_2$(μ-Bbim)] (**1-Ln**, Y (red), Gd (green), Tb (purple), Dy(blue)). Concentrations: **1-Y**: 8.054 x 10^{-6} mol/L, **1-Gd**: 2.636 x 10^{-5} mol/L, **1-Tb**: 1.389x 10^{-5} mol/L, **1-Dy**: 1.353 x 10^{-5} mol/L.

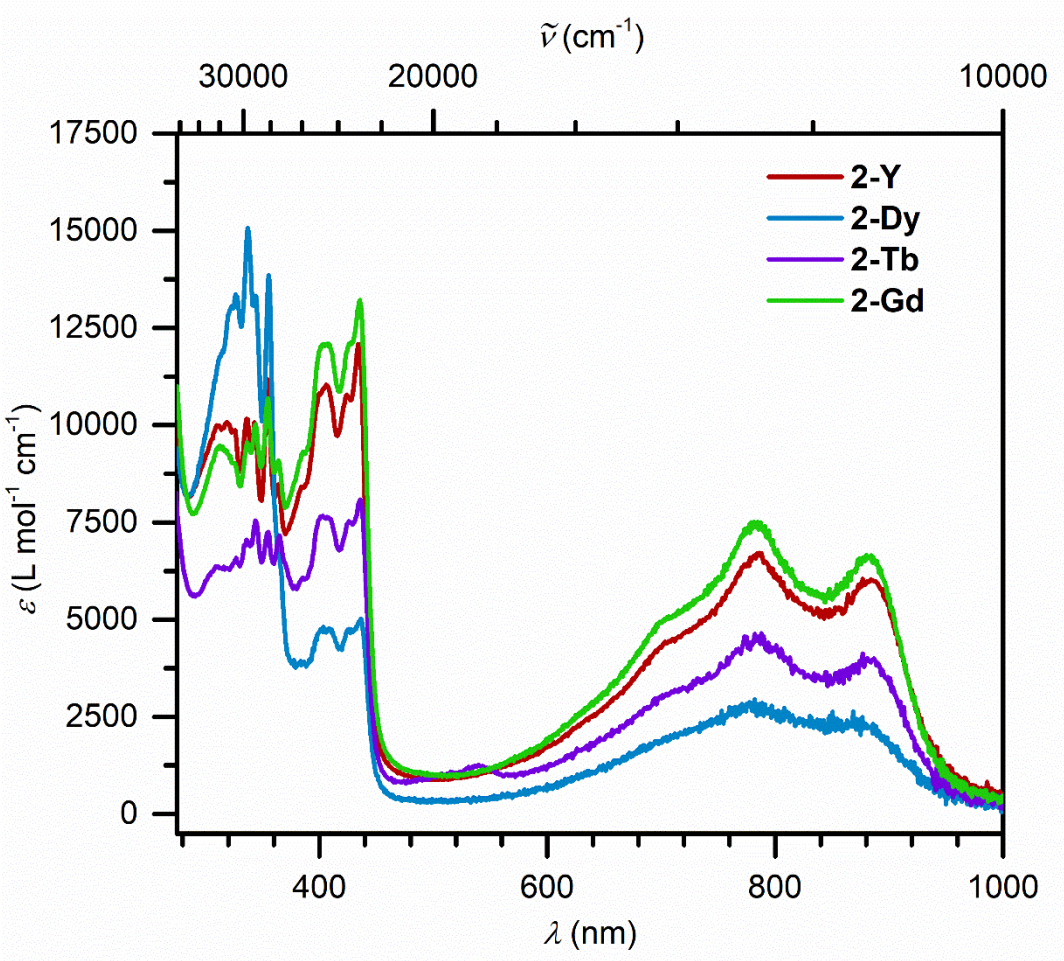

Figure S15. Superimposed UV/Vis spectra of [K(crypt-222)][(Cp*$_2$Ln)$_2$(μ-Bbim$^•$)] (**2-Ln**, Y (red),[1] Gd (green), Tb (purple), Dy (blue)). Concentrations: **2-Y**: 5.091 x 10^{-5} mol/L, **2-Gd**: 3.198 x 10^{-5} mol/L, **2-Tb**: 2.307 x 10^{-5} mol/L, **2-Dy**: 1.114 x 10^{-4} mol/L.

Cyclic Voltammetry

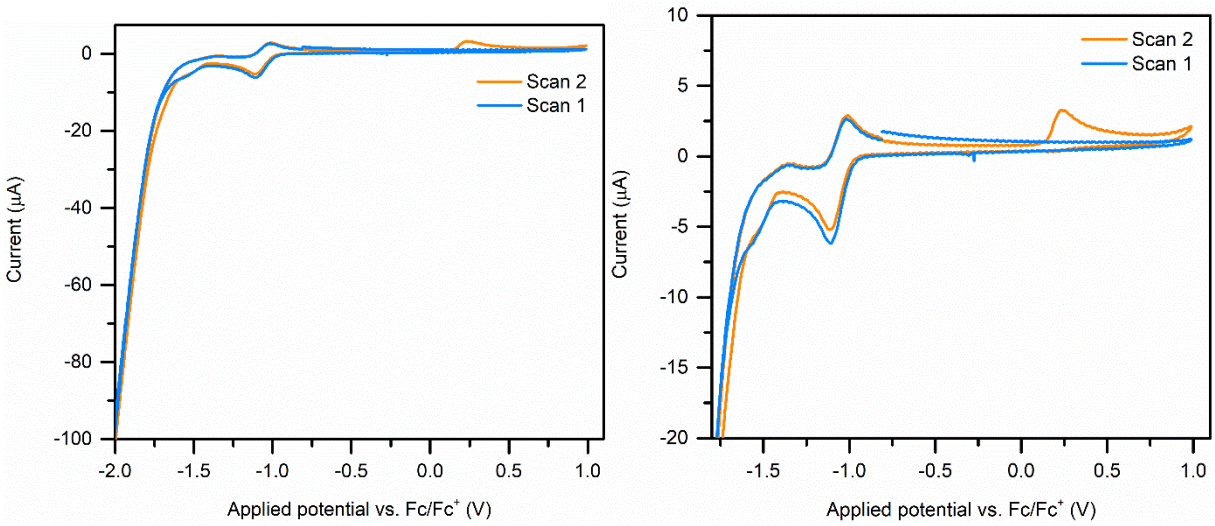

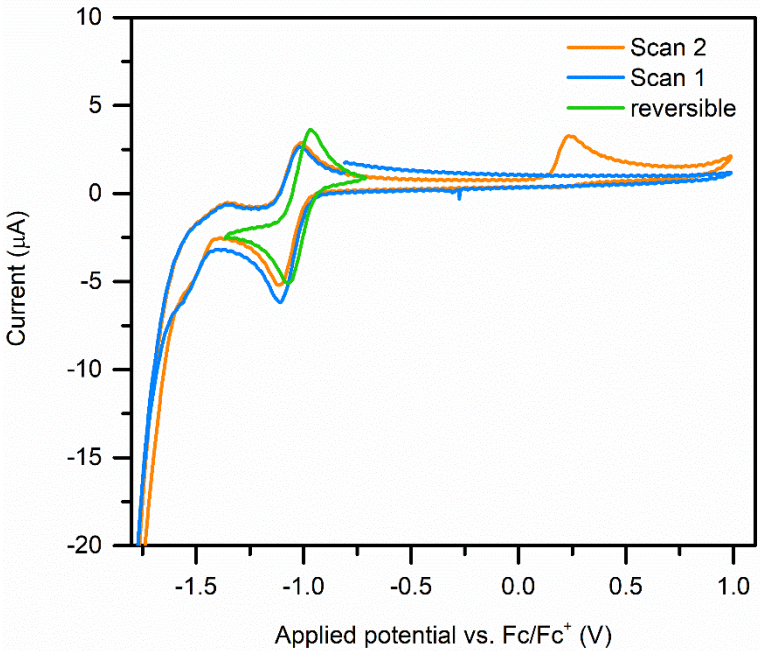

Figure S16. Top left: Full cyclic voltammogram of [K(crypt-222)][(Cp*$_2$Dy)$_2$(µ-Bbim$^{\bullet}$)], **2-Dy**, measured in THF at 300 K with 0.25 M (^{n}Bu$_4$N)PF$_6$ supporting electrolyte and 1.7 mmol/L analyte concentration. The initial scan is depicted in blue, the second scan is depicted in orange. Top right: Magnification of the area between −1.8 and 1.1 V for the first and second scan. Bottom: Magnified scans superimposed with the reversible scan depicted in the main text.

Magnetism

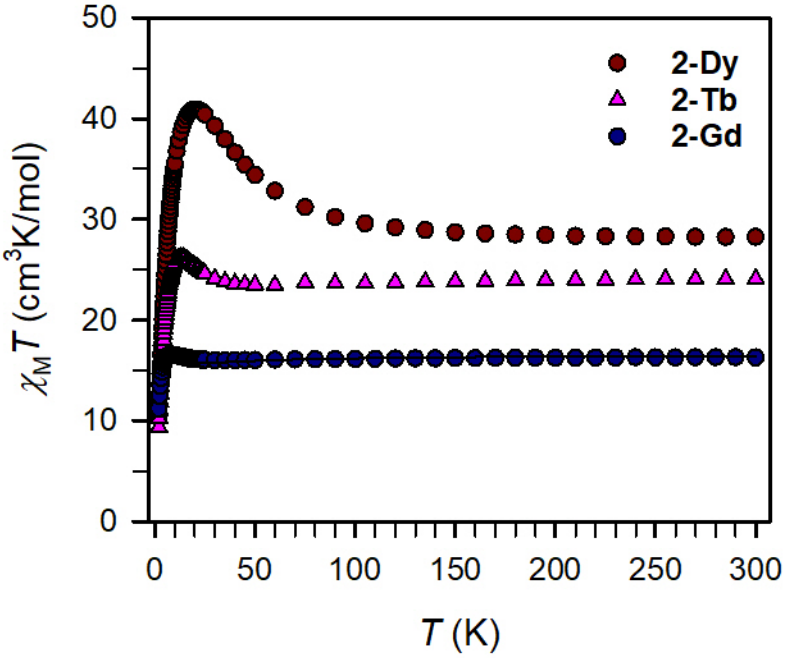

Figure S17. Variable-temperature dc magnetic susceptibility data for restrained polycrystalline samples of **2-Dy** (dark red circles), **2-Tb** (pink triangles) and **2-Gd** (dark blue circles) collected under a 1 T applied dc field. The black line represents a fit to the data for **2-Gd** giving rise to J = −1.85(4) cm^{-1} and g = 2.03(1).

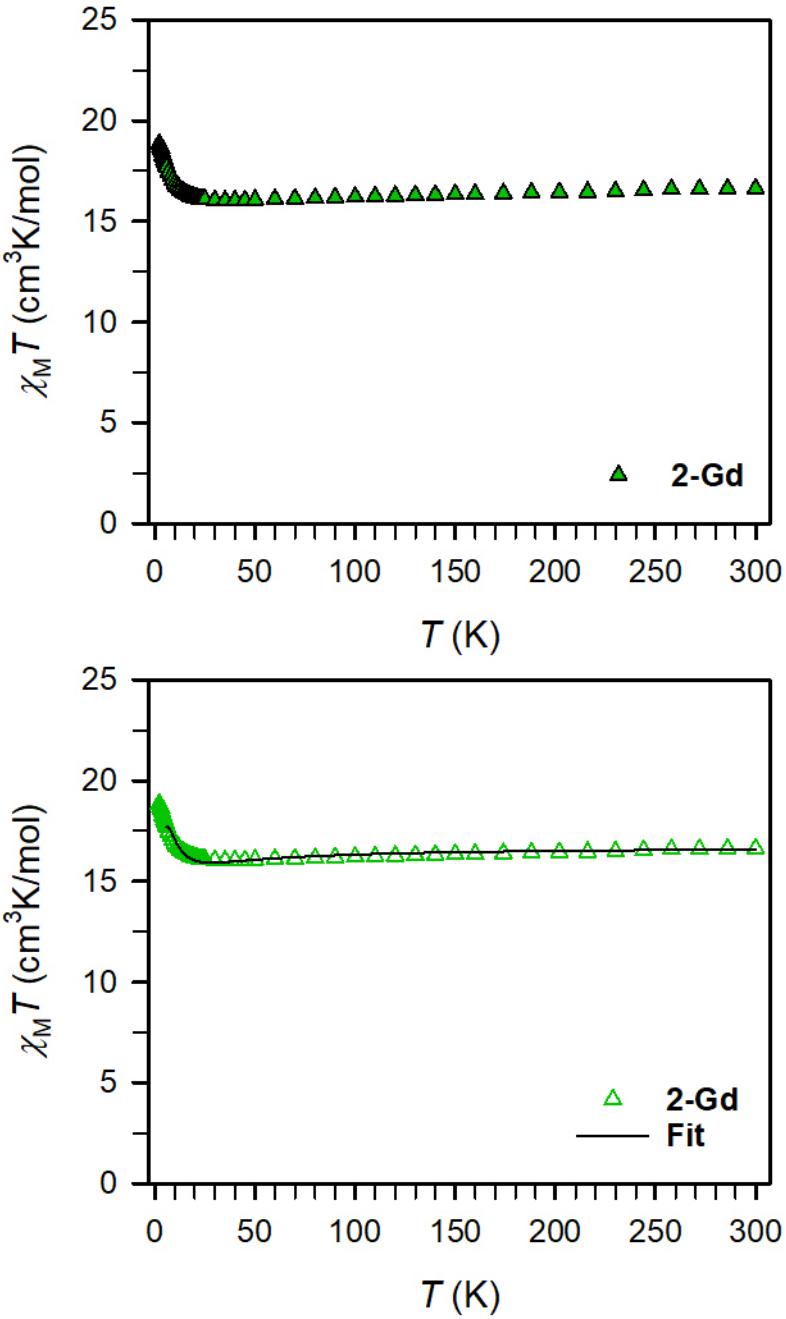

Figure S18. Variable-temperature dc magnetic susceptibility data for a restrained polycrystalline sample of **2-Gd** collected under a 0.1 T applied dc field (top and bottom). The black line represents a fit to the data giving rise to J = 1.96(2) cm^{-1} and g = 2.03(1).

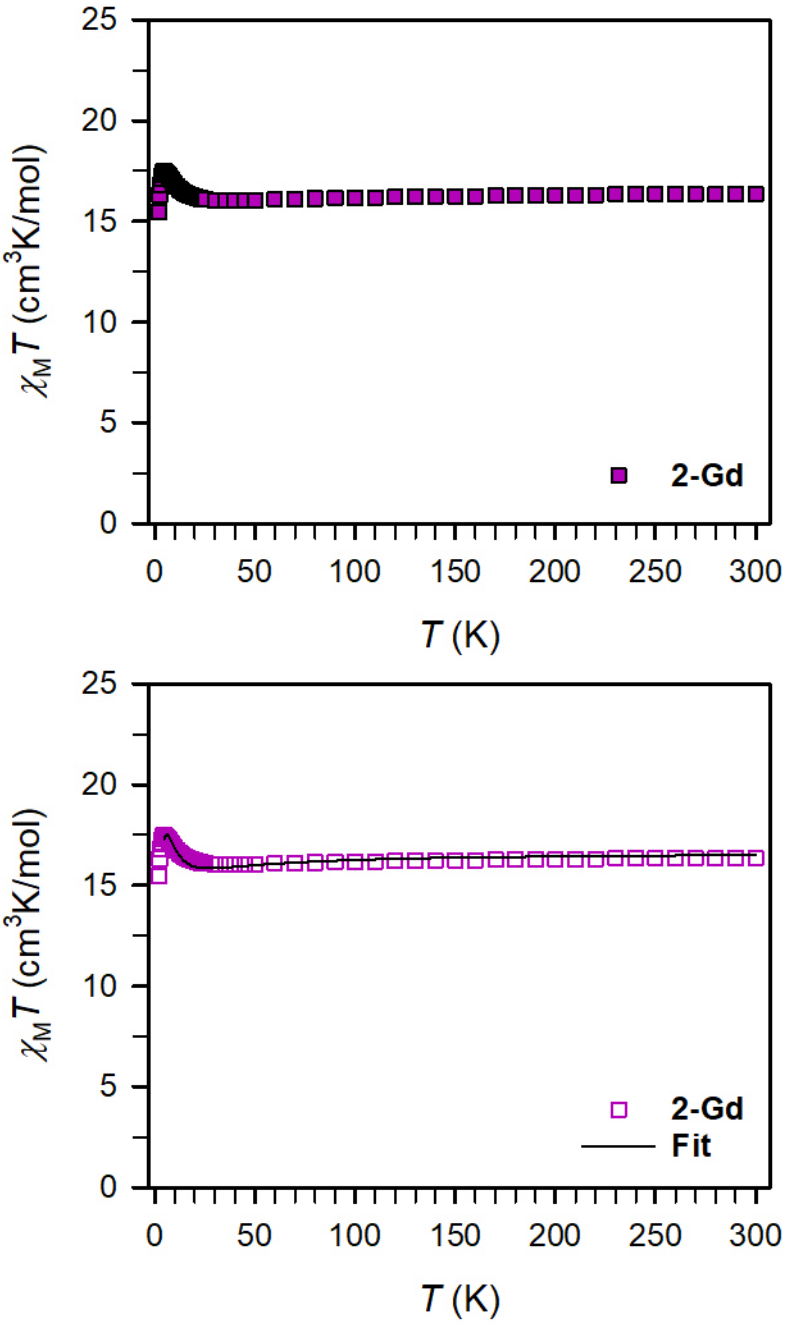

Figure S19. Variable-temperature dc magnetic susceptibility data for a restrained polycrystalline sample of **2-Gd** collected under a 0.5 T applied dc field (top and bottom). The black line represents a fit to the data for **2-Gd** giving rise to J = −1.88(2) cm^{-1} and g = 2.037(1).

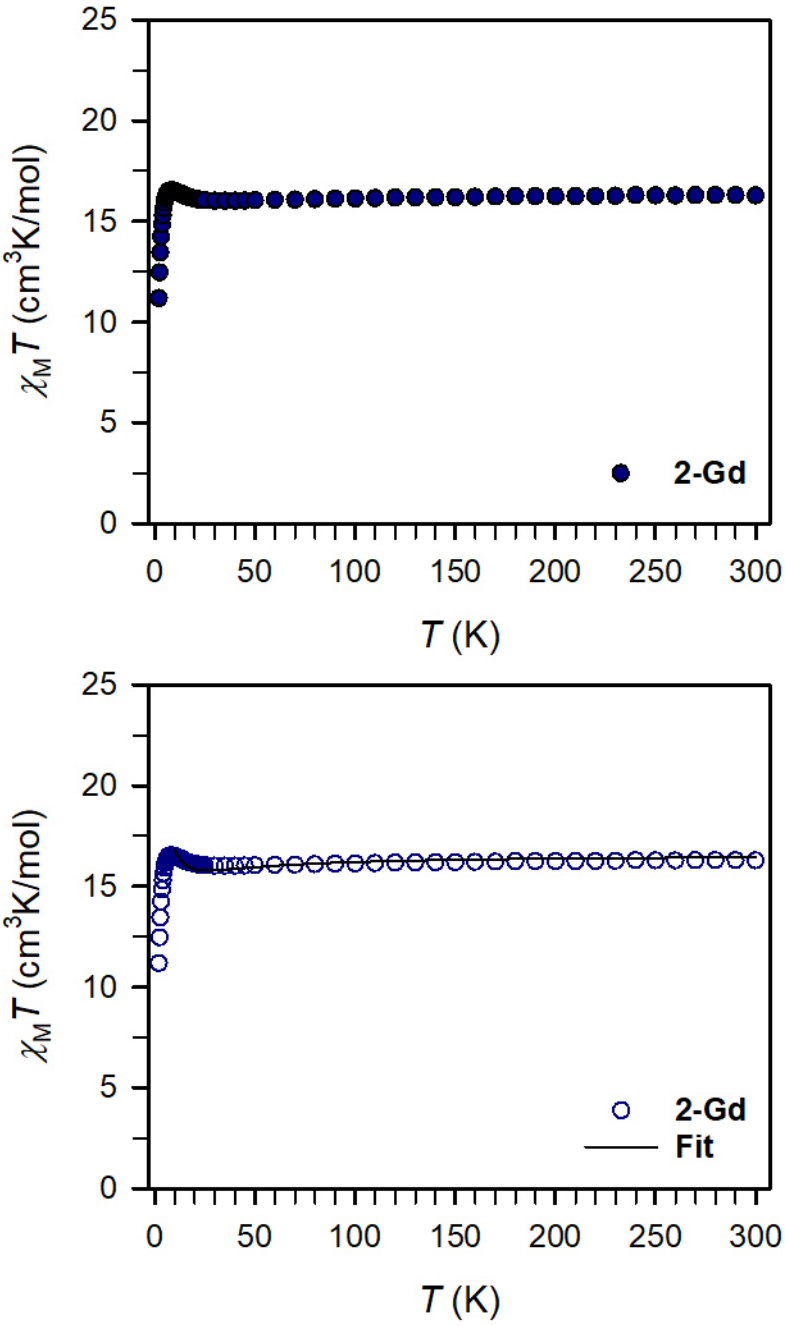

Figure S20. Variable-temperature dc magnetic susceptibility data for a restrained polycrystalline sample of **2-Gd** collected under a 1 T applied dc field (top and bottom). The black line represents a fit to the data for **2-Gd** giving rise to J = −1.85(1) cm^{-1} and g = 2.03(1).

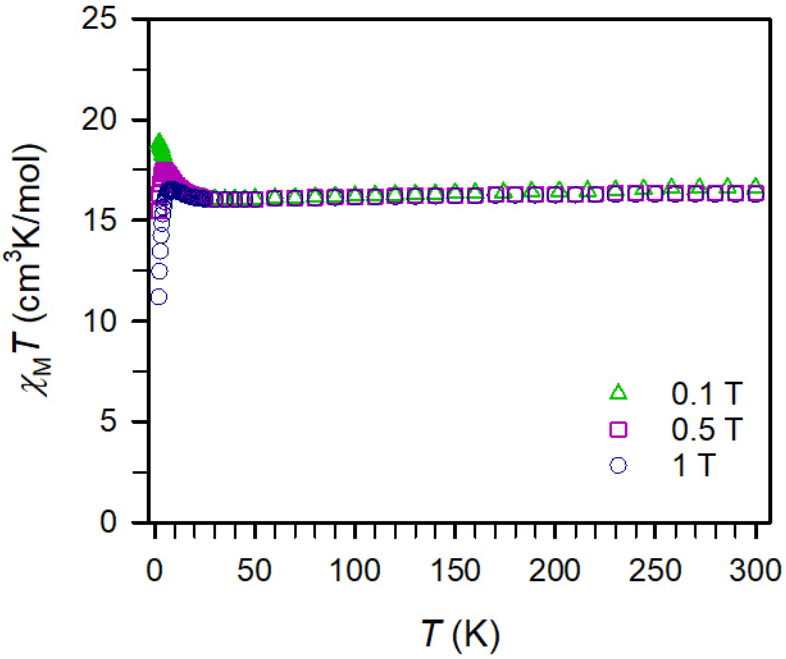

Figure S21. Superimposed variable-temperature dc susceptibility data of polycrystalline **2-Gd** collected under 0.1 T (green triangles), 0.5 T (purple squares), 1 T (blue circles) applied dc field.

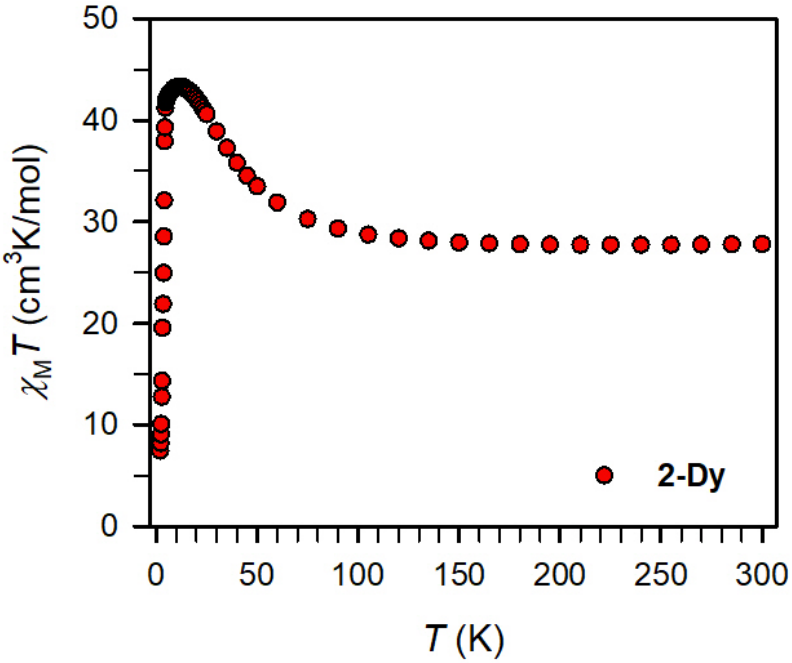

Figure S22. Variable-temperature dc magnetic susceptibility data for a restrained polycrystalline sample of **2-Dy** collected under a 0.1 T applied dc field.

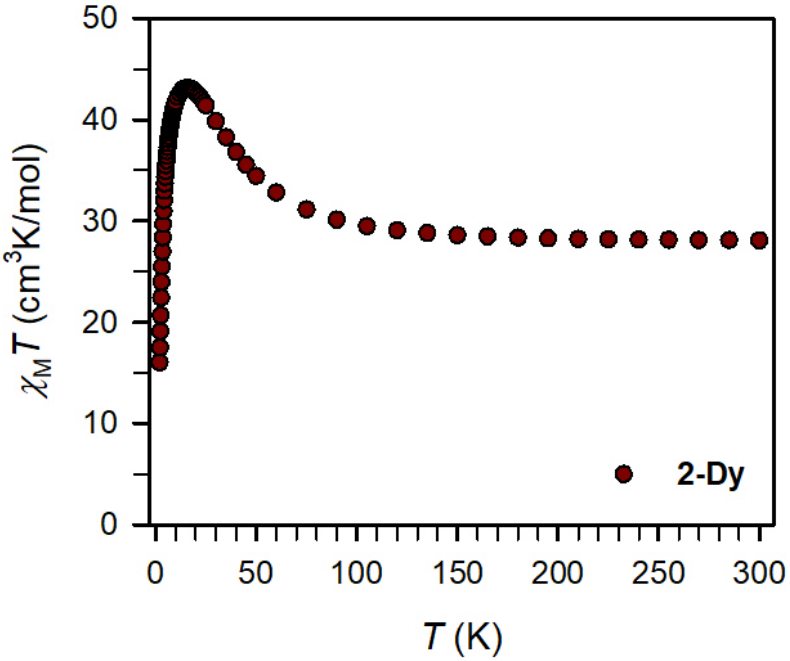

Figure S23. Variable-temperature dc magnetic susceptibility data for a restrained polycrystalline sample of **2-Dy** collected under a 0.5 T applied dc field.

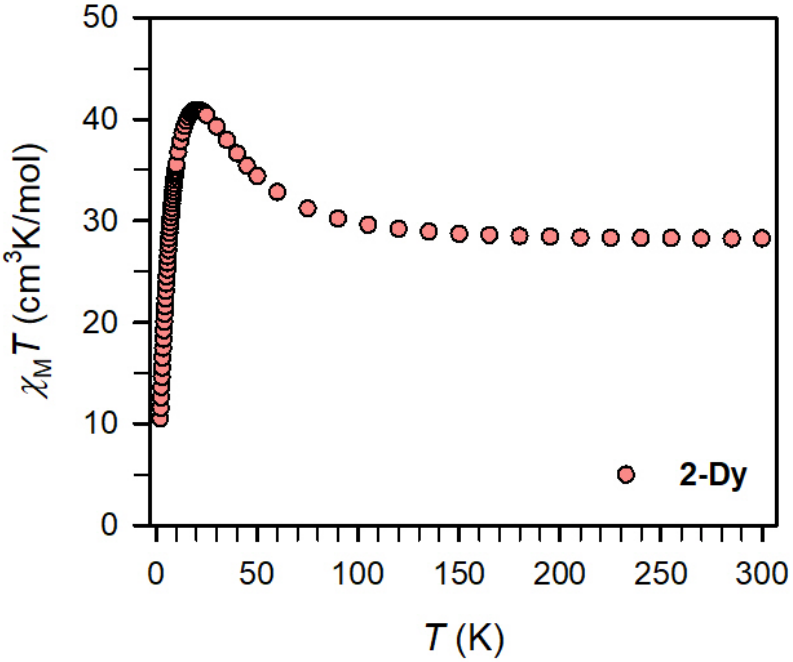

Figure S24. Variable-temperature dc magnetic susceptibility data for a restrained polycrystalline sample of **2-Dy** collected under a 1 T applied dc field.

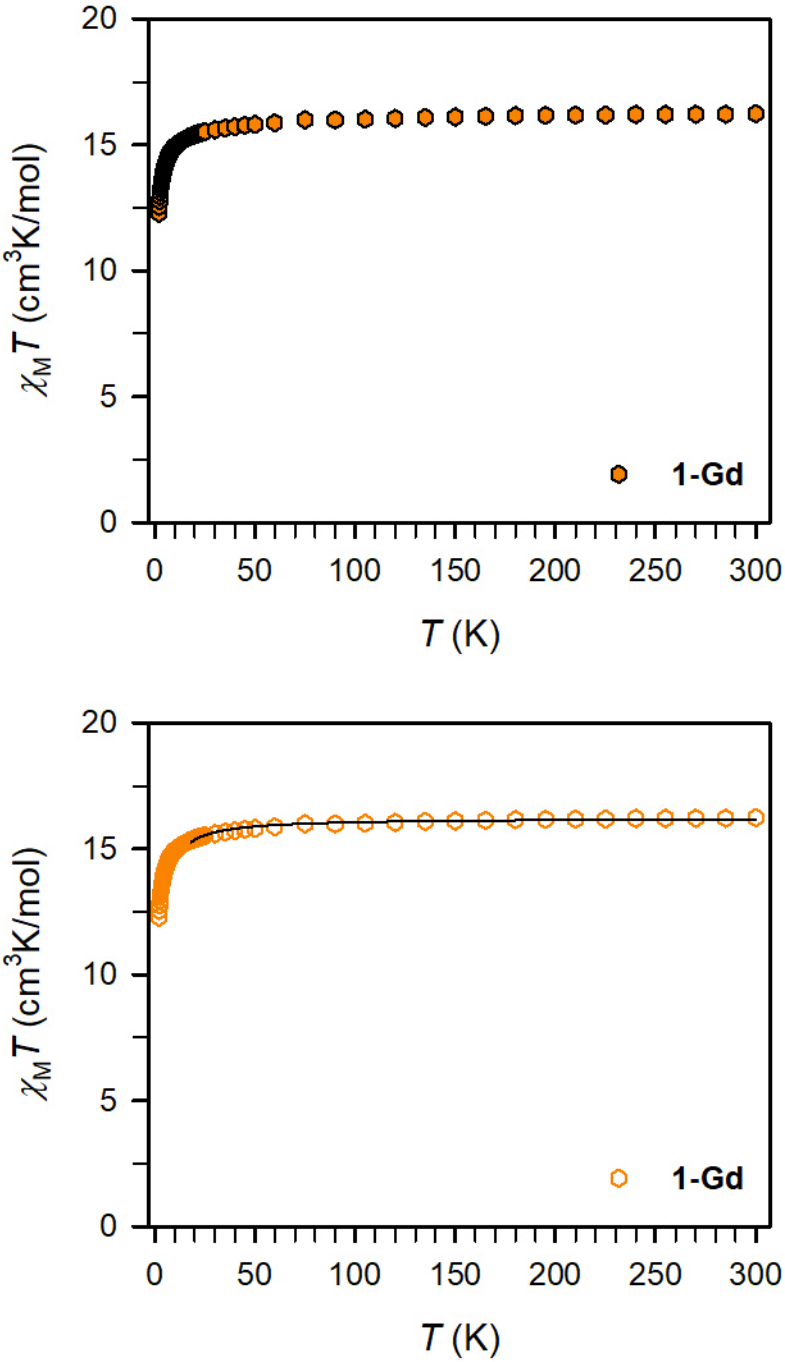

Figure S25. Variable-temperature dc magnetic susceptibility data for a restrained polycrystalline sample of **1-Gd** collected under a 0.1 T applied dc field. The black line represents a fit to the data for **1-Gd** giving rise to J = −0.064(2) cm^{-1} and g = 2.029(1).

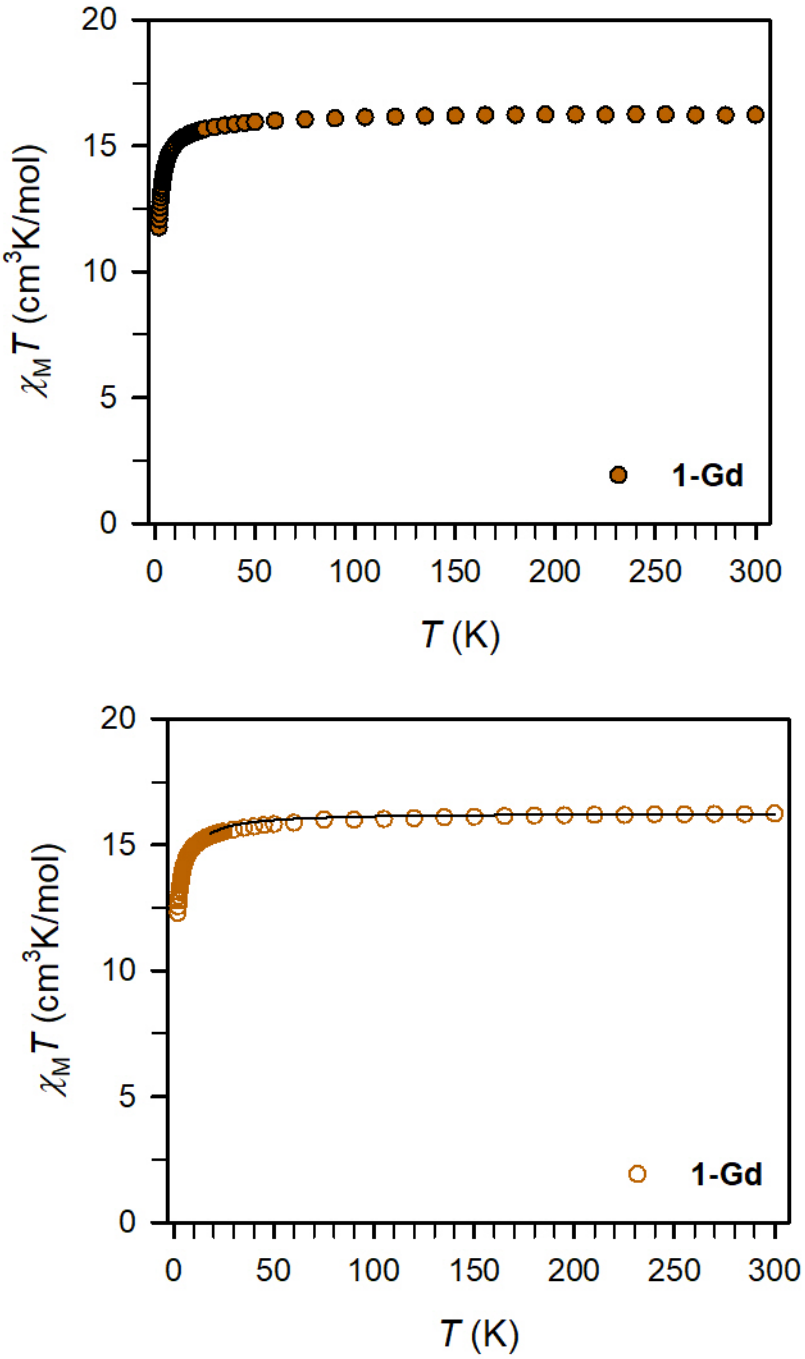

Figure S26. Variable-temperature dc magnetic susceptibility data for a restrained polycrystalline sample of **1-Gd** collected under a 0.5 T applied dc field. The black line represents a fit to the data for **1-Gd** giving rise to J = −0.056(1) cm^{-1} and g = 2.032(1).

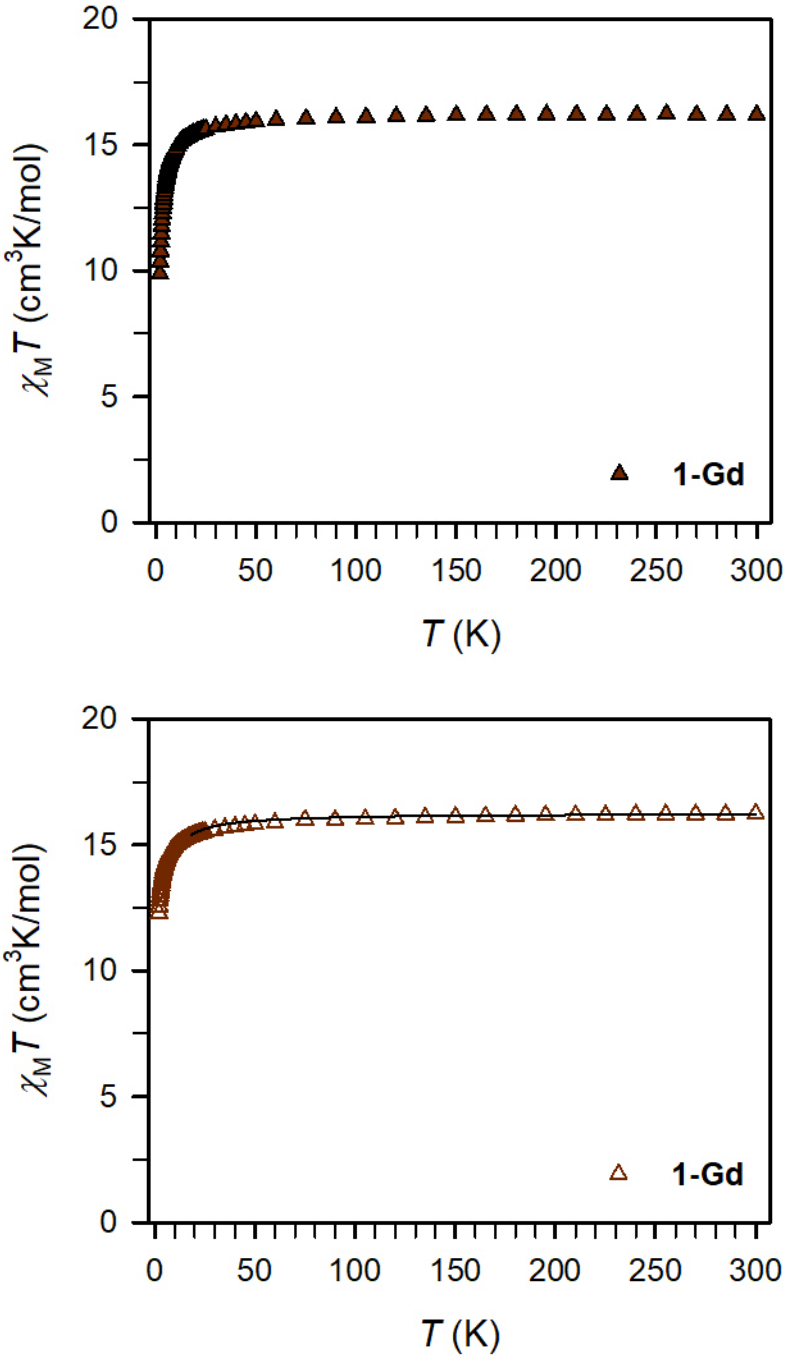

Figure S27. Variable-temperature dc magnetic susceptibility data for a restrained polycrystalline sample of **1-Gd** collected under a 1 T applied dc field. The black line represents a fit to the data for **1-Gd** giving rise to J = −0.058(1) cm^{-1} and g = 2.031(1).

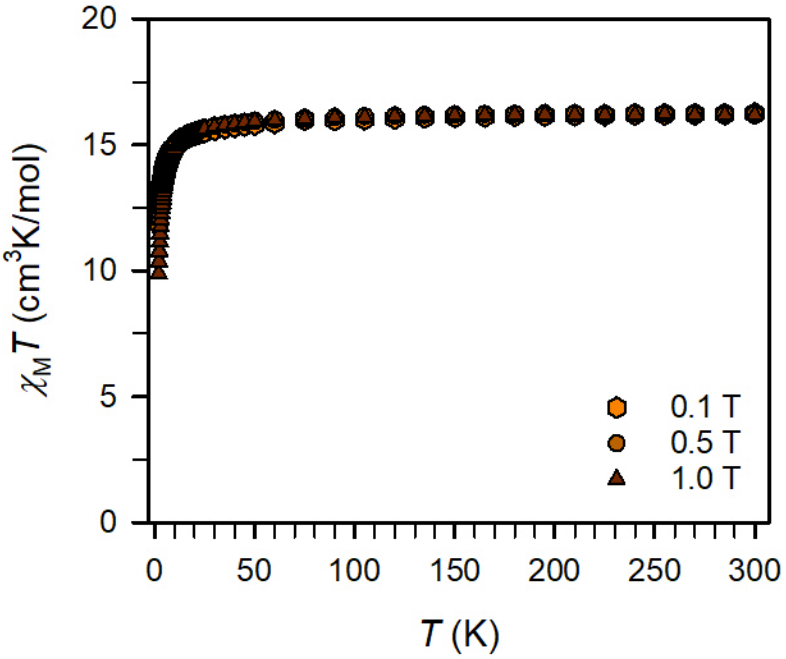

Figure S28. Variable-temperature dc magnetic susceptibility data for a restrained polycrystalline sample of **1-Gd** collected under 0.1, 0.5, and 1 T applied dc fields.

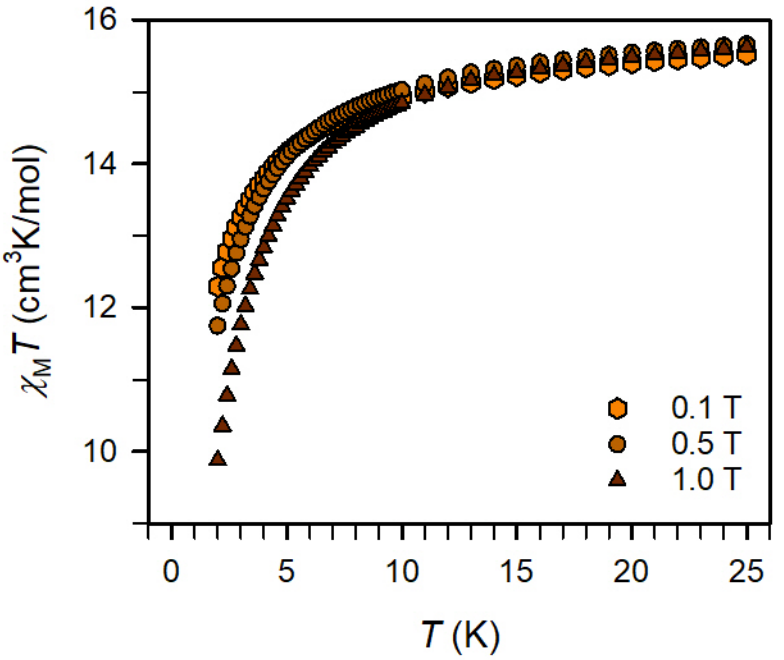

Figure S29. Enlarged plot of variable-temperature dc magnetic susceptibility data for a restrained polycrystalline sample of **1-Gd** collected under 0.1, 0.5, and 1 T applied dc fields.

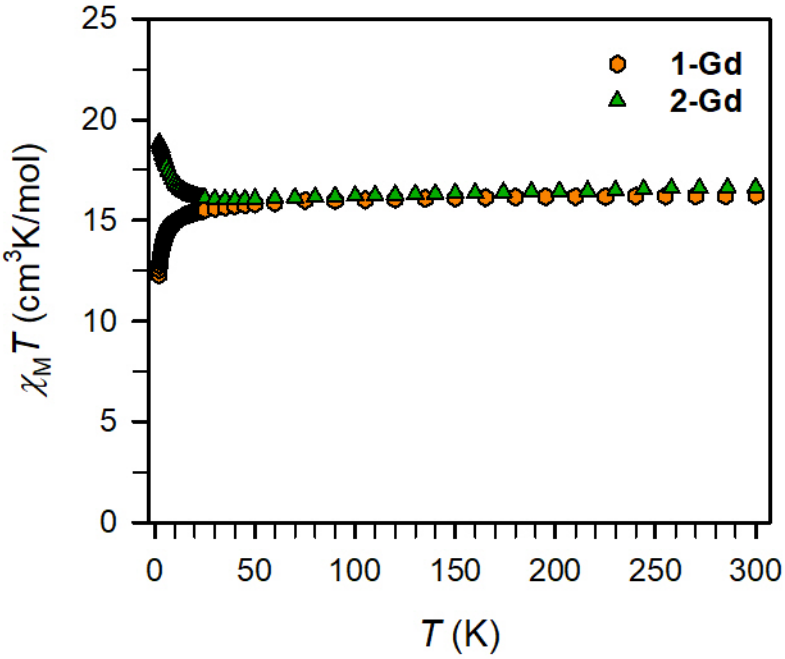

Figure S30. Variable-temperature dc magnetic susceptibility data for restrained polycrystalline samples of **1-Gd** and **2-Gd** collected under a 0.1 T applied dc field.

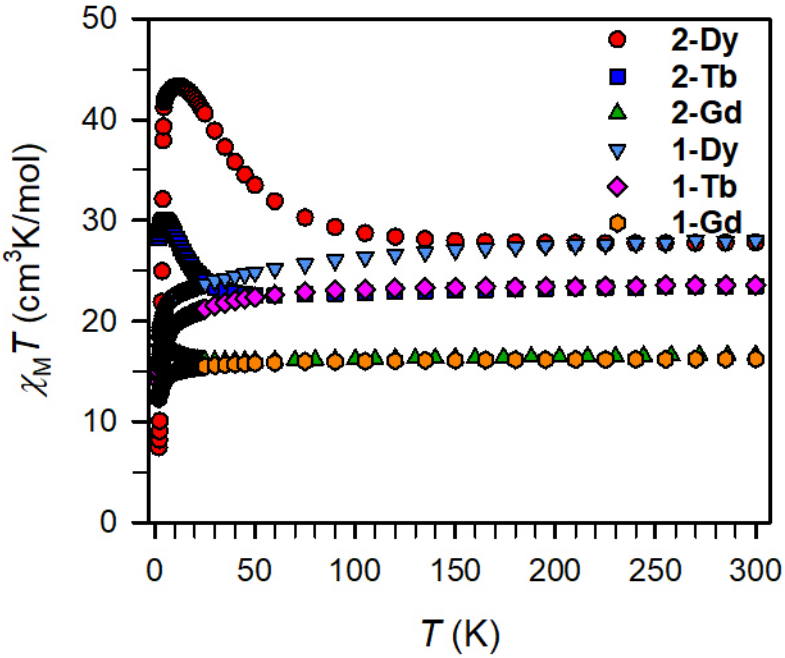

Figure S31. Variable-temperature dc magnetic susceptibility data for restrained polycrystalline samples of **1-Dy**, **1-Tb**, **1-Gd**, **2-Dy**, **2-Tb**, and **2-Gd** collected under a 0.1 T applied dc field.

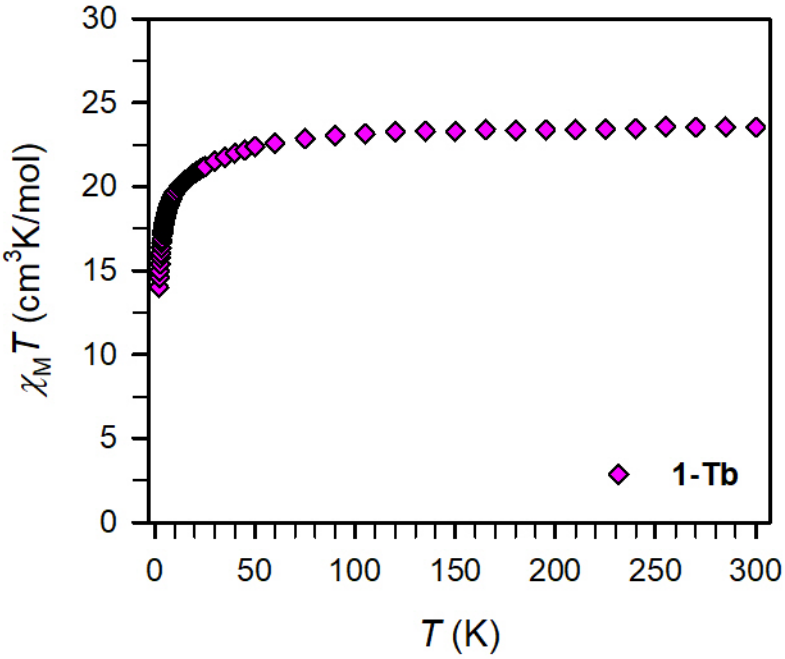

Figure S32. Variable-temperature dc magnetic susceptibility data for a restrained polycrystalline sample of **1-Tb** collected under a 0.1 T applied dc field.

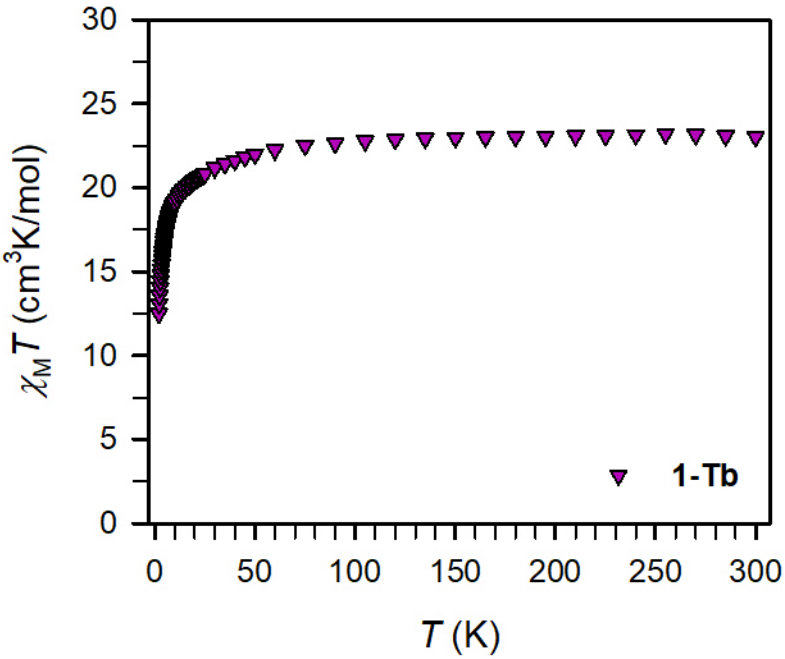

Figure S33. Variable-temperature dc magnetic susceptibility data for a restrained polycrystalline sample of **1-Tb** collected under a 0.5 T applied dc field.

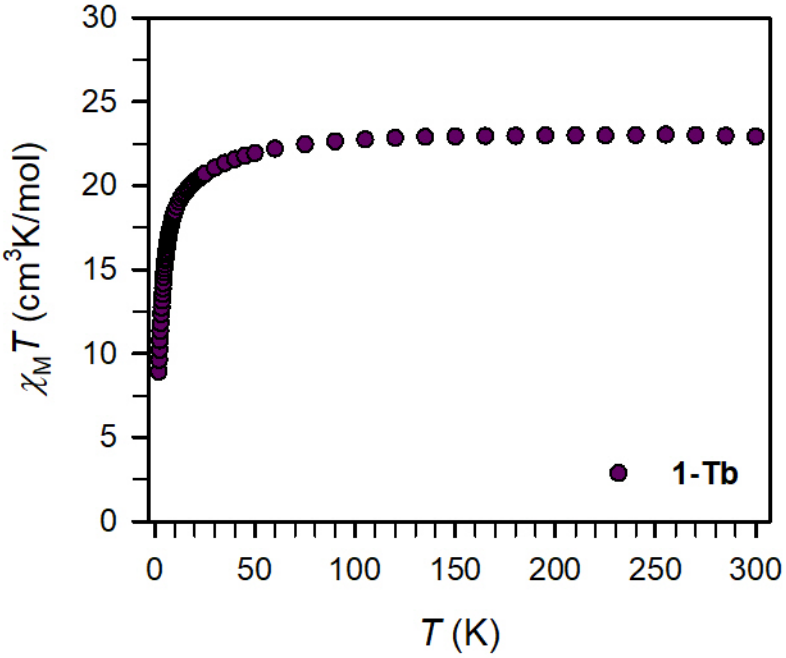

Figure S34. Variable-temperature dc magnetic susceptibility data for a restrained polycrystalline sample of **1-Tb** collected under a 1 T applied dc field.

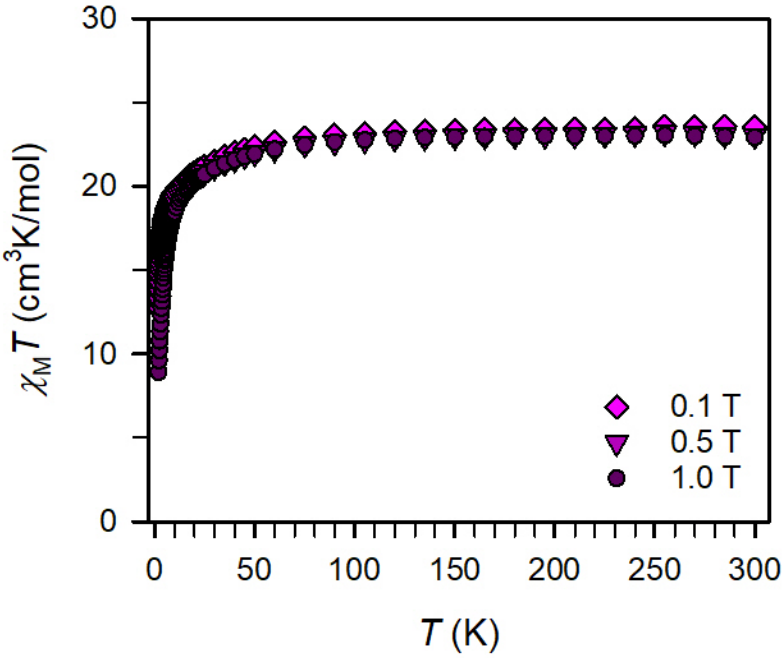

Figure S35. Variable-temperature dc magnetic susceptibility data for a restrained polycrystalline sample of **1-Tb** collected under 0.1, 0.5, and 1 T applied dc fields.

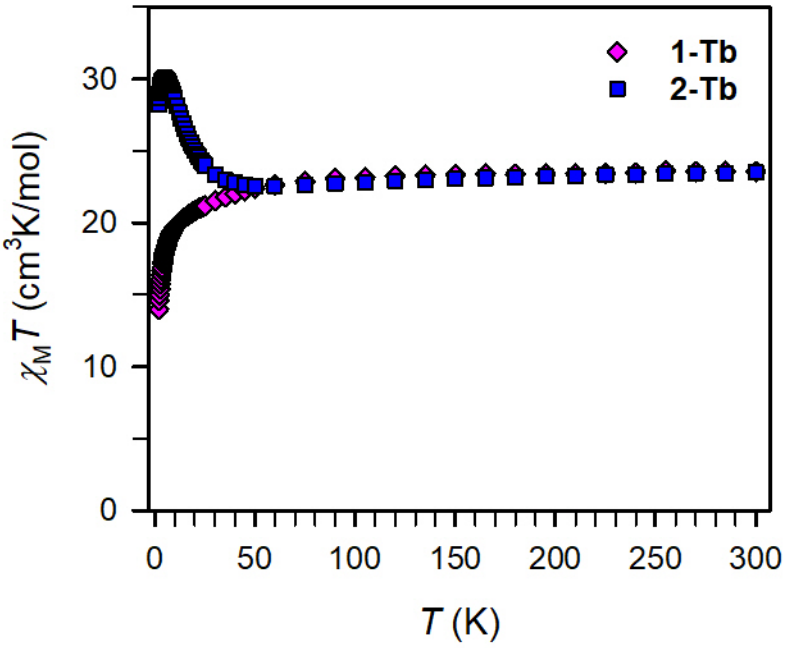

Figure S36. Variable-temperature dc magnetic susceptibility data for restrained polycrystalline samples of **1-Tb** and **2-Tb** collected under a 0.1 T applied dc field.

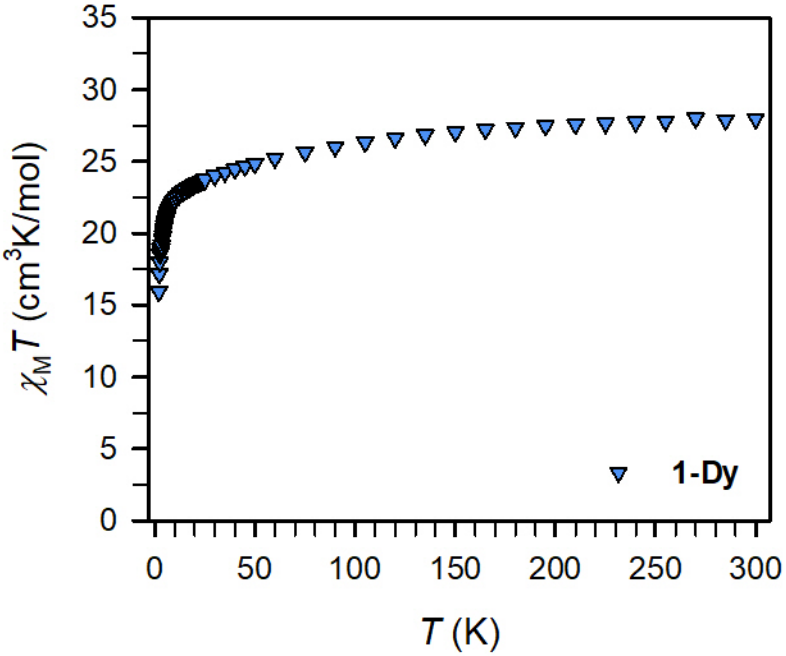

Figure S37. Variable-temperature dc magnetic susceptibility data for a restrained polycrystalline sample of **1-Dy** collected under a 0.1 T applied dc field.

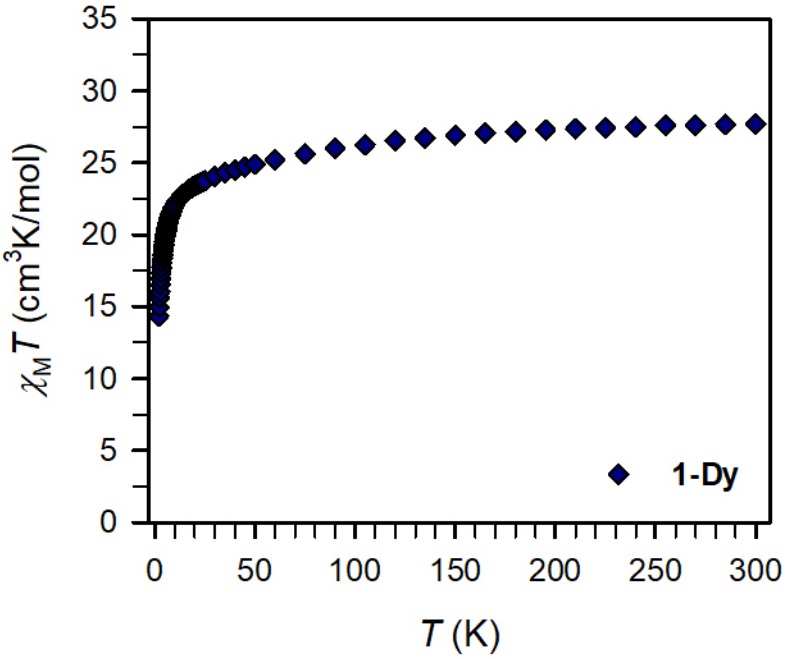

Figure S38. Variable-temperature dc magnetic susceptibility data for a restrained polycrystalline sample of **1-Dy** collected under a 0.5 T applied dc field.

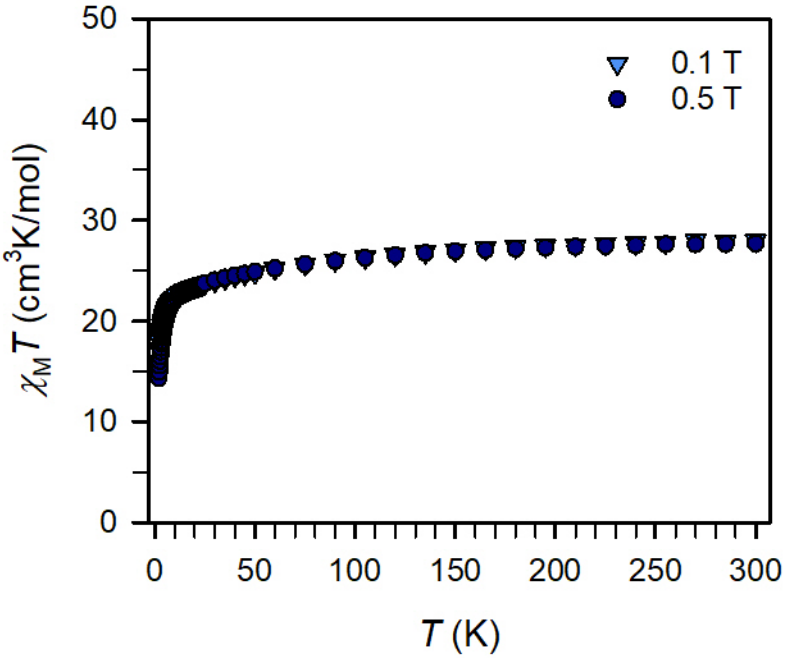

Figure S39. Variable-temperature dc magnetic susceptibility data for a restrained polycrystalline sample of **1-Dy** collected under 0.1 and 0.5 T applied dc fields.

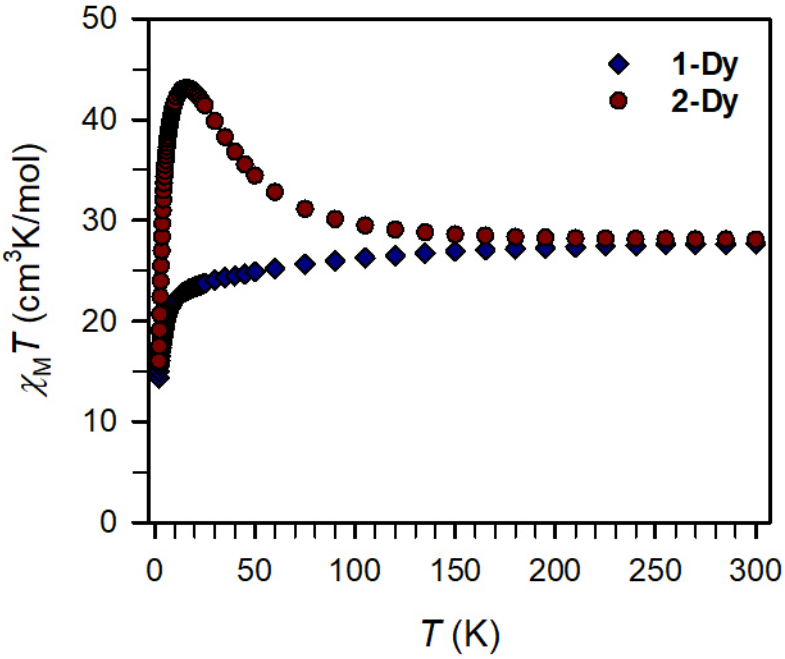

Figure S40. Variable-temperature dc magnetic susceptibility data for restrained polycrystalline samples of **1-Dy** and **2-Dy** collected under a 0.5 T applied dc field.

Data derived from Ac Susceptibility Measurements

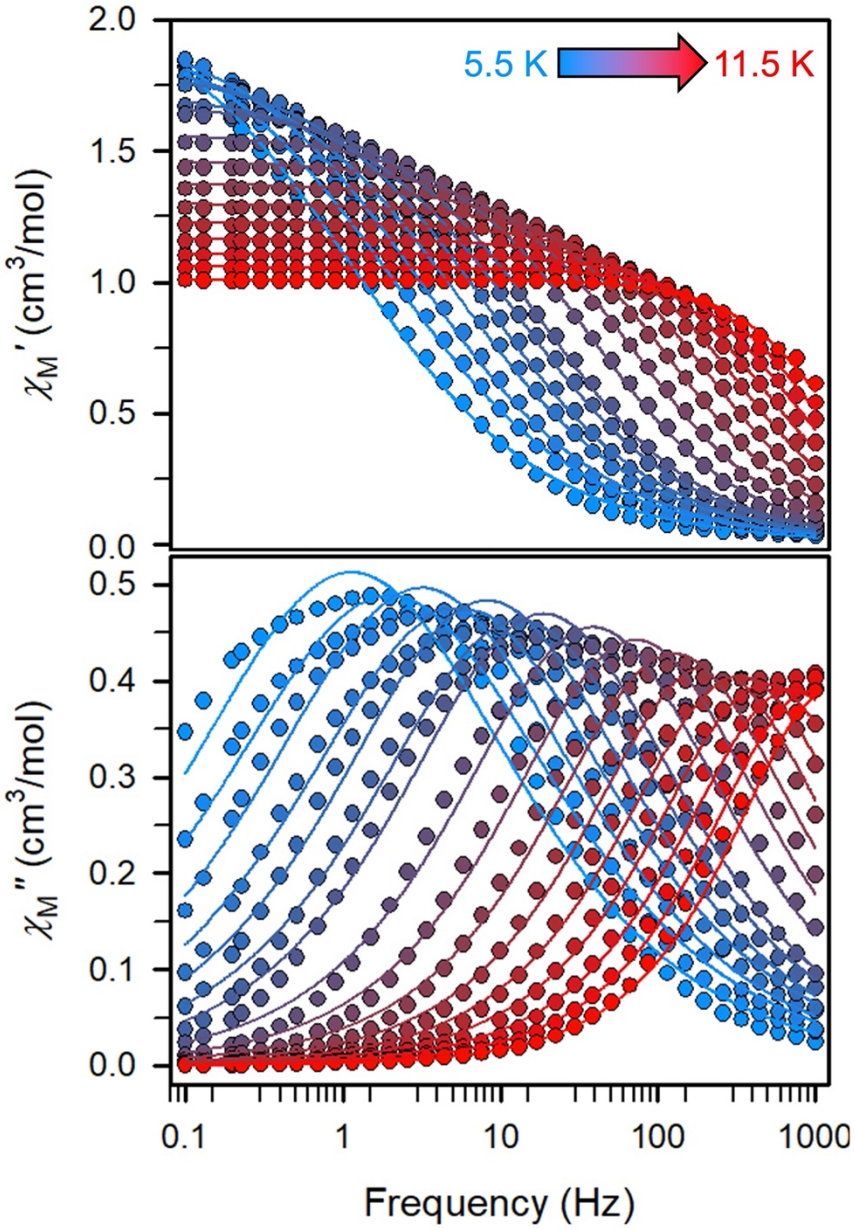

Figure S41. Variable-temperature, variable-frequency in-phase (χ_M') (top) and out-of-phase (χ_M'') (bottom) ac magnetic susceptibility data collected for **2-Dy** under a zero applied dc field from 5.5 to 11.5 K. Solid lines represent fits to the data, as described in the main text. A non-zero χ_M'' out-of-phase signal indicates the presence of an energy barrier to spin reversal.

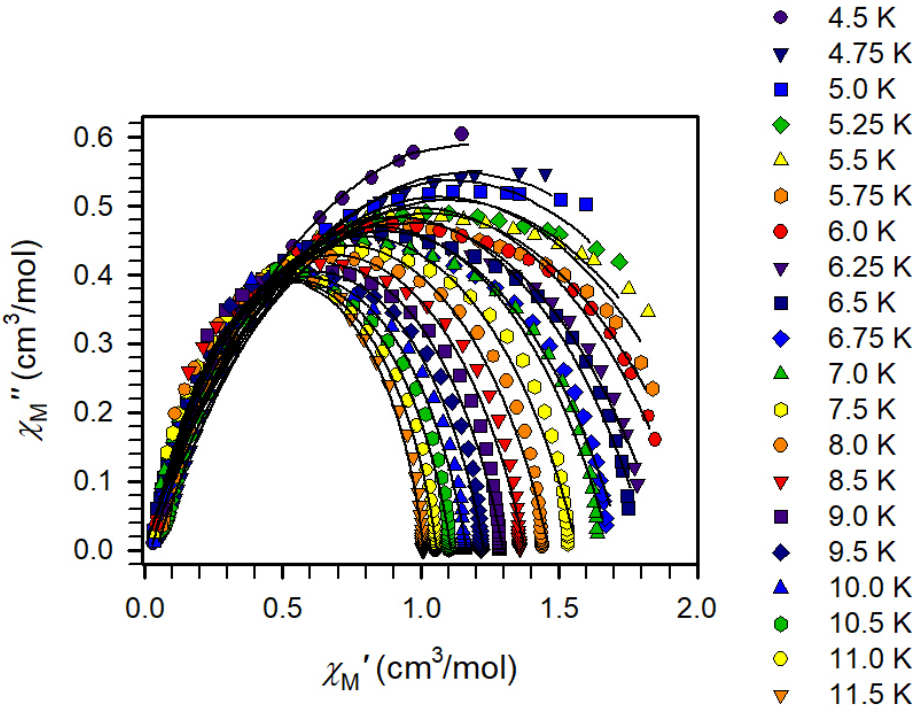

Figure S42. Cole-Cole (Argand) plots for ac susceptibility collected from 4.5 to 11.5 K under zero applied dc field for **2-Dy**. Symbols represent the experimental data points and the points representing the fits are connected by black solid lines.

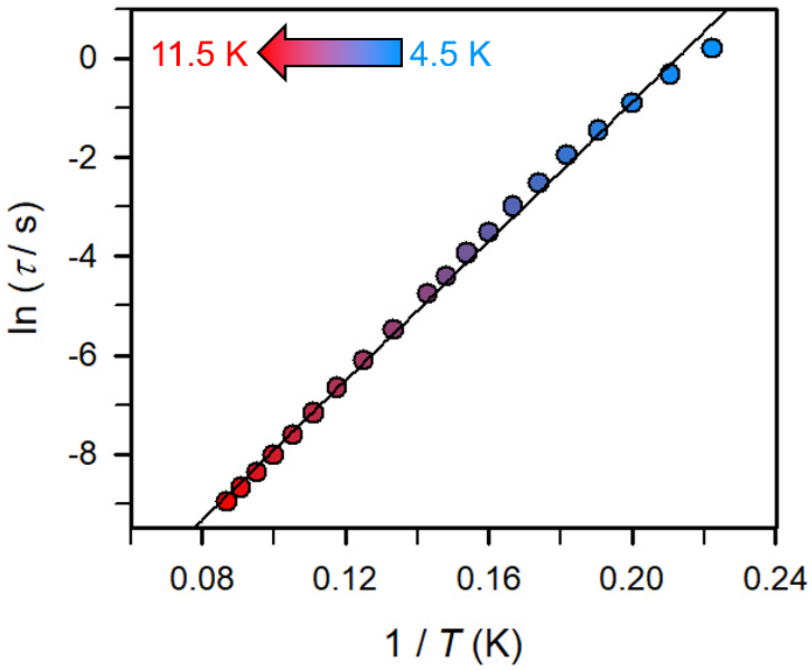

Figure S43. Arrhenius plots of relaxation time data for **2-Dy** obtained between 4.5 and 11.5 K (see Figure 6 in the main text). The black line corresponds to a linear fit to the Arrhenius equation, as described in the main text, yielding U_{eff} = 48.9(1) cm^{-1} and τ_0 = 3.2(1) × 10^{-7} s (all data points between 4.5 and 5.5 K were fitted).

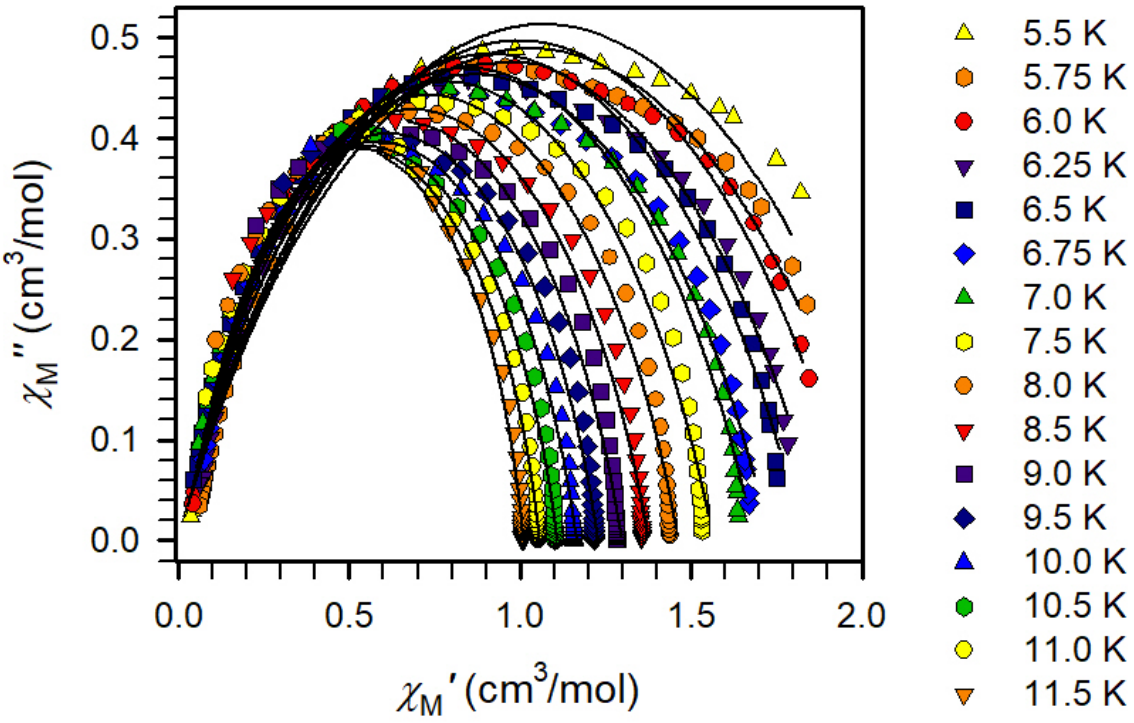

Figure S44. Cole-Cole (Argand) plots for ac susceptibility collected from 5.5 to 11.5 K under zero applied dc field for **2-Dy**. Symbols represent the experimental data points and the points representing the fits are connected by black solid lines.

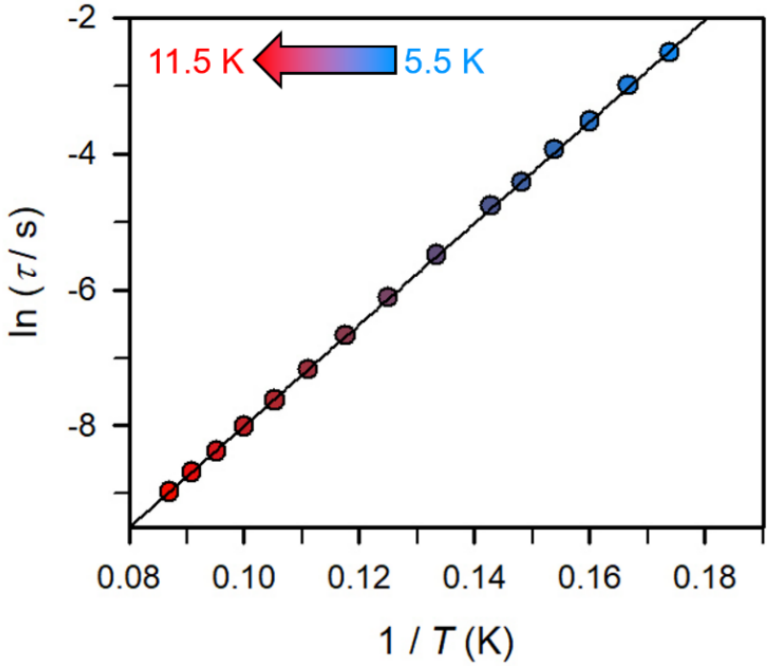

Figure S45. Arrhenius plot of relaxation time data for **2-Dy** obtained between 5.5 and 11.5 K (see Figure S24). The black line corresponds to a linear fit to the Arrhenius equation, as described in the main text, yielding U_{eff} = 51.9(1) cm^{-1} and τ_0 = 1.91(1) × 10^{-7} s. Data points between 5.5 K and 11.5 K were fitted due to the slight curvature in Figure S23 indicating a deviation from linearity of the temperature-dependent τ at the lowest measured temperatures. The obtained values for U_{eff} and τ_0 are similar to those shown in Figure S23

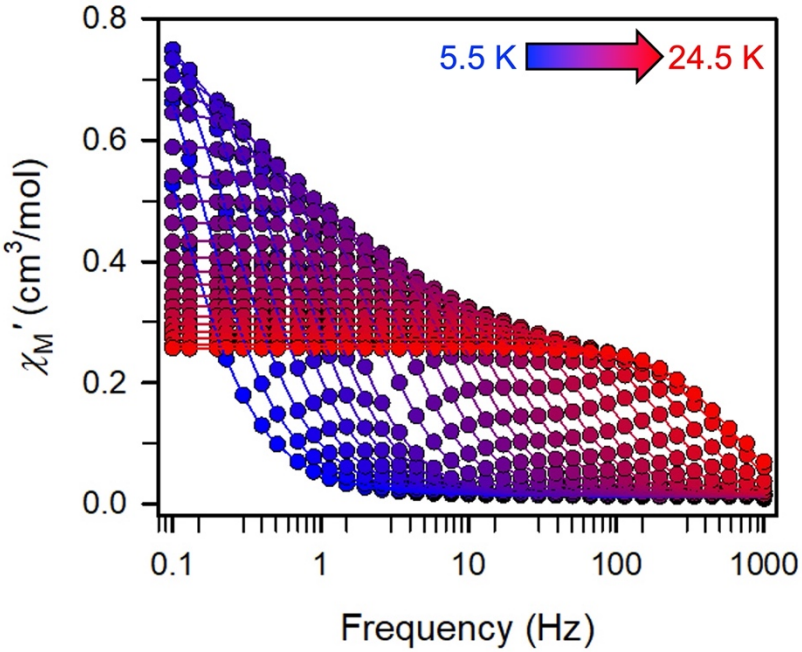

Figure S46. Variable-temperature, variable-frequency in-phase (χ_M') ac magnetic susceptibility data collected for **1-Dy** under a zero applied dc field from 5.5 to 24.5 K. Solid lines represent fits to the data, as described in the main text. A non-zero χ_M'' out-of-phase signal indicates the presence of an energy barrier to spin reversal.

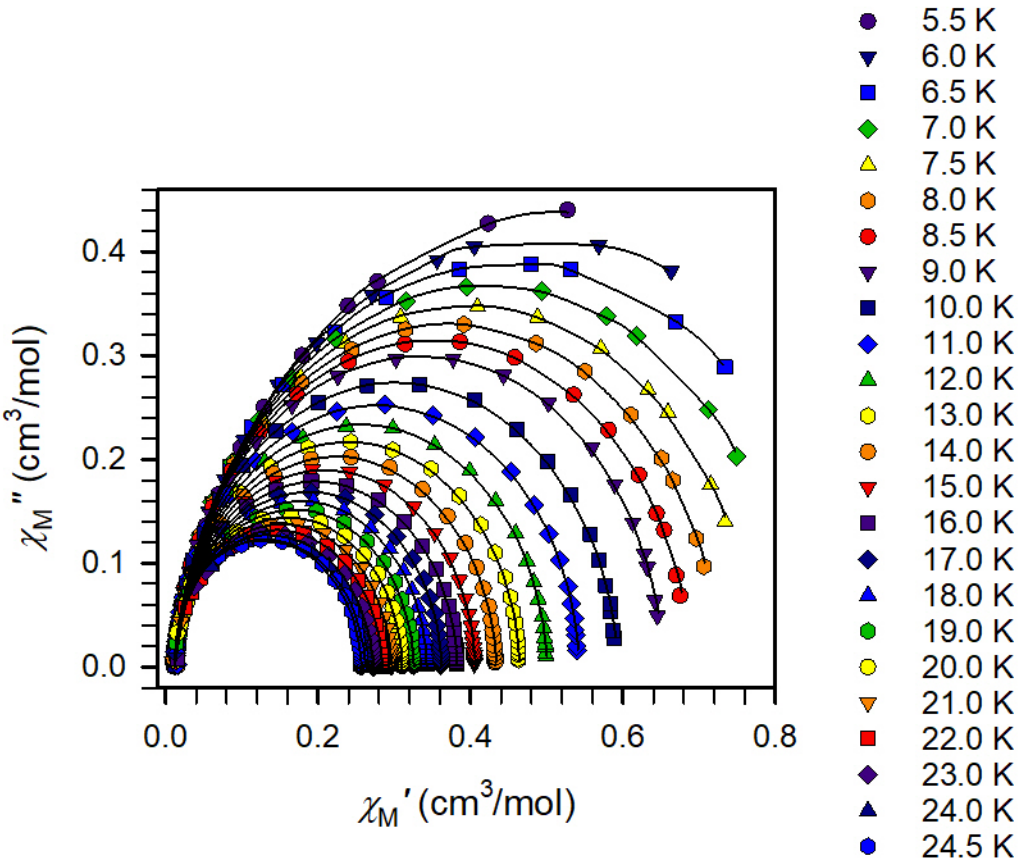

Figure S47. Cole-Cole (Argand) plots for ac susceptibility collected from 5.5 to 24.5 K under zero applied dc field for **1-Dy**. Symbols represent the experimental data points and the points representing the fits are connected by black solid lines.

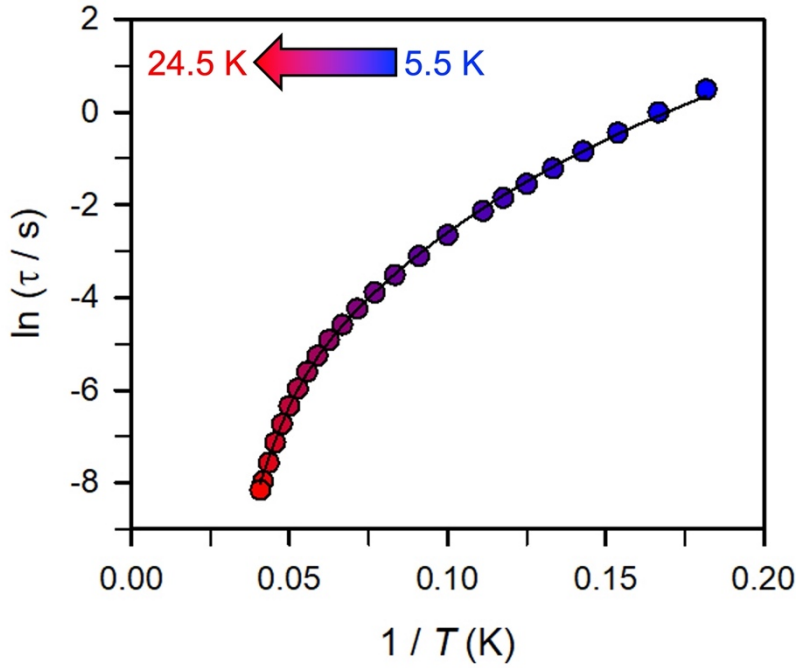

Figure S48. Arrhenius plots of relaxation time data for **1-Dy** obtained between 5.5 and 11.5 K (see Figure 7 in the main text) through ac magnetic susceptibility measurements. The black line corresponds to a fit to Orbach and Raman relaxation processes. as described in the main text, yielding U_{eff} = 185.0(1) cm^{-1} and τ_0 = 1.0(1) × 10^{-8} s.

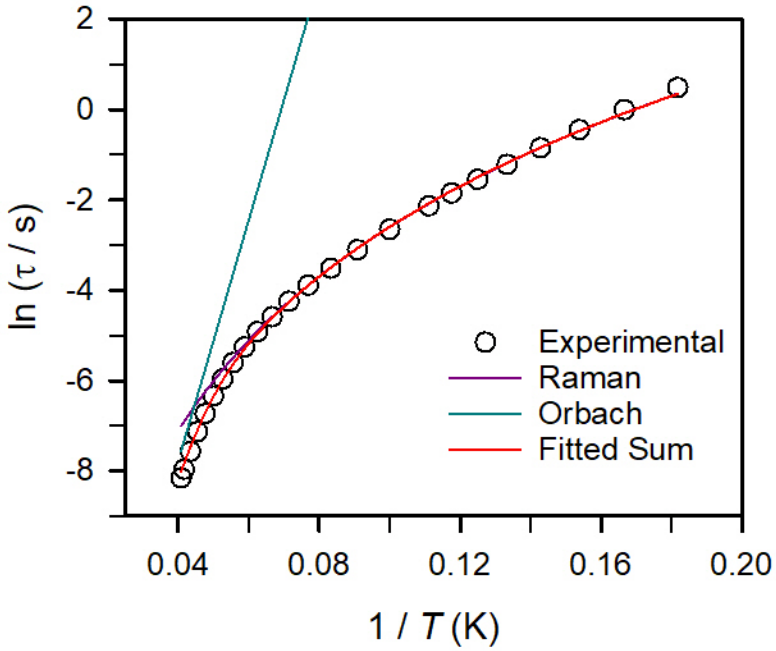

Figure S49. Individual contributions of the multiple magnetic relaxation pathways to the Arrhenius plot of **1-Dy** at 0 Oe shown in Figure S48. The best fit yielded U_{eff} = 185.0(1) cm^{-1} and τ_0 = 1.0(1) × 10^{-8} s. The red line represents a fit to one Orbach relaxation process and a Raman process. Individual parameters used to calculate the contributions are given in Table S6.

Data derived from Dc Relaxation Experiments

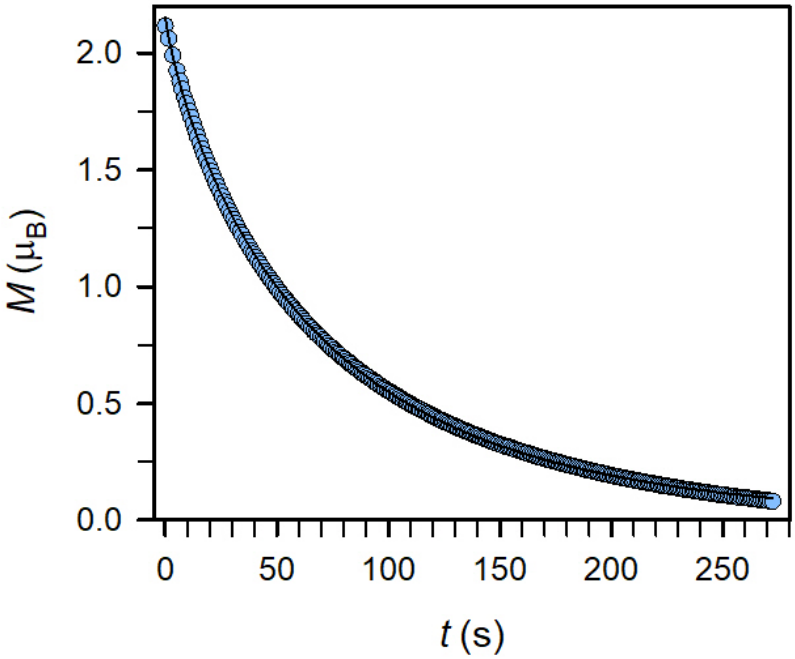

Figure S50. Plot of magnetization vs. time used to derive relaxation times for **2-Dy** at 1.8 K. The data (pale blue circles) were fit to a function of the form y = a · exp (−((t/τ)^b)) where b is a stretch factor (black line). Decay of the magnetization vs. time for **2-Dy**, obtained by applying a magnetic field of 0.1 T to the sample at a temperature of 50 K, cooling the sample to 1.8 K, and then removing the magnetic field.

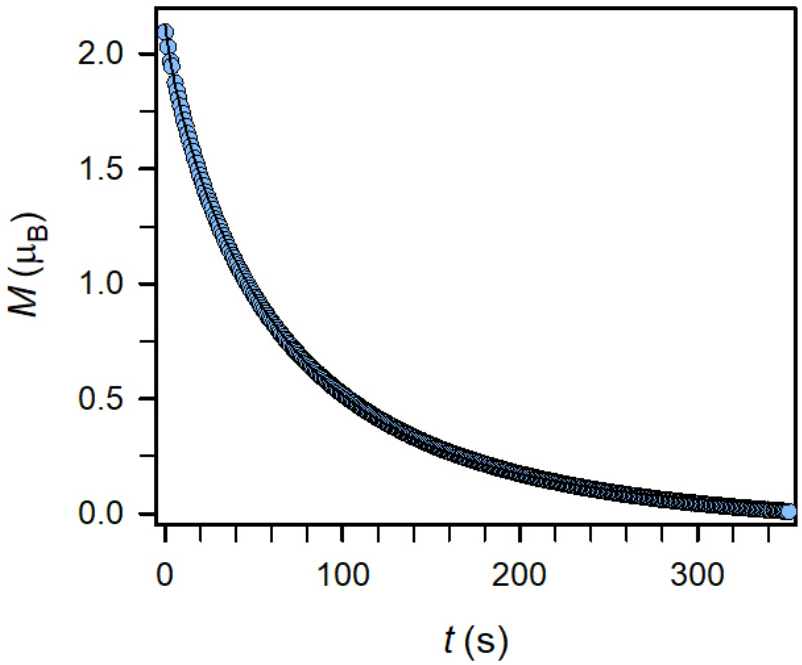

Figure S51. Plot of magnetization vs. time used to derive relaxation times for **2-Dy** at 2.0 K. The data (pale blue circles) were fit to a function of the form y = a · exp (−((t/τ)^b)) where b is a stretch factor (black line). Decay of the magnetization vs. time for **2-Dy**, obtained by applying a magnetic field of 0.1 T to the sample at a temperature of 50 K, cooling the sample to 2.0 K, and then removing the magnetic field.

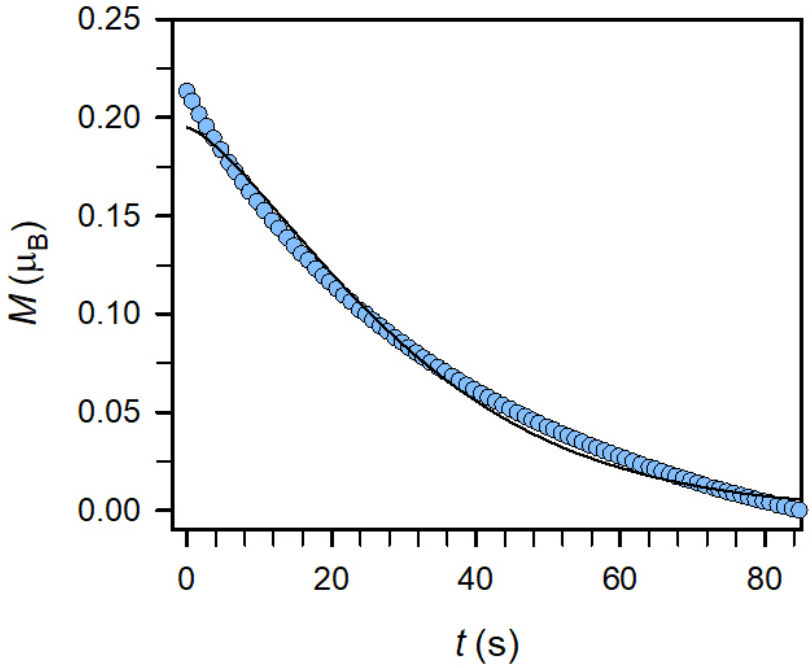

Figure S52. Plot of magnetization vs. time used to derive relaxation times for **2-Dy** at 2.5 K. The data (pale blue circles) were fit to a function of the form y = a · exp (−((*t*/τ)^{b})) where b is a stretch factor (black line). Decay of the magnetization vs. time for **2-Dy**, obtained by applying a magnetic field of 0.1 T to the sample at a temperature of 50 K, cooling the sample to 2.5 K, and then removing the magnetic field.

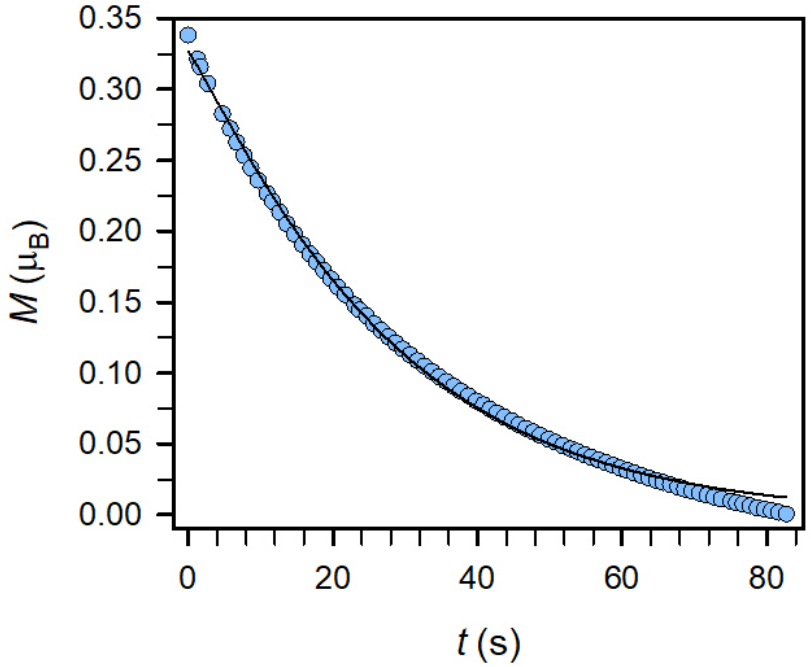

Figure S53. Plot of magnetization vs. time used to derive relaxation times for **2-Dy** at 3.0 K. The data (pale blue circles) were fit to a function of the form y = a · exp (−((*t*/τ)^{b})) where b is a stretch factor (black line). Decay of the magnetization vs. time for **2-Dy**, obtained by applying a magnetic field of 0.1 T to the sample at a temperature of 50 K, cooling the sample to 3.0 K, and then removing the magnetic field.

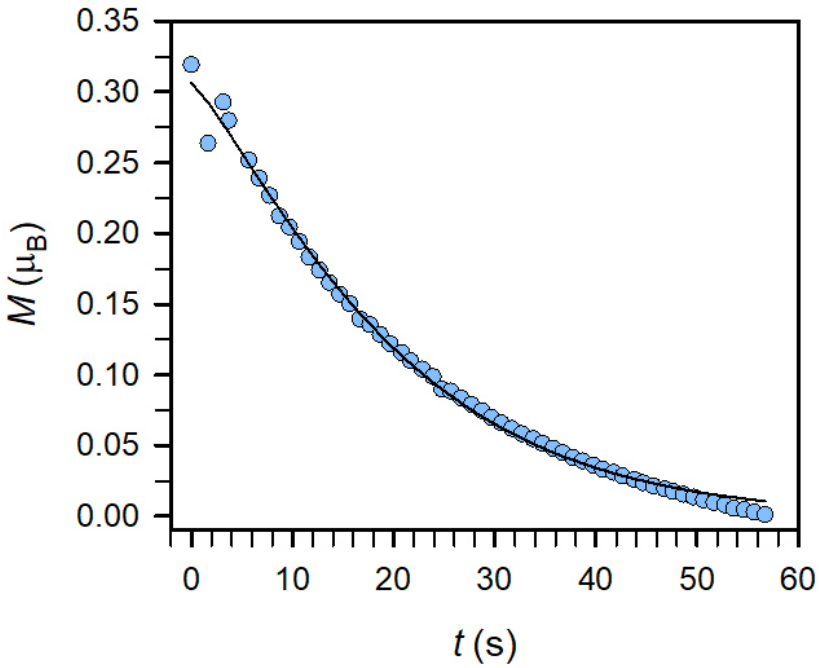

Figure S54. Plot of magnetization vs. time used to derive relaxation times for **2-Dy** at 3.5 K. The data (pale blue circles) were fit to a function of the form y = a · exp (−((t/τ)^b)) where b is a stretch factor (black line). Decay of the magnetization vs. time for **2-Dy**, obtained by applying a magnetic field of 0.1 T to the sample at a temperature of 50 K, cooling the sample to 3.5 K, and then removing the magnetic field.

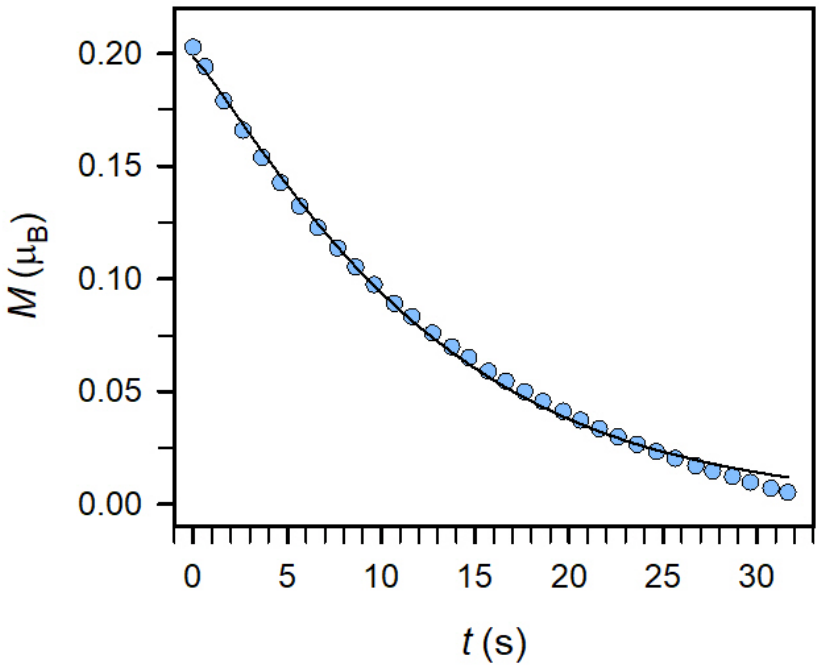

Figure S55. Plot of magnetization vs. time used to derive relaxation times for **2-Dy** at 4.0 K. The data (pale blue circles) were fit to a function of the form y = a · exp (−((t/τ)^b)) where b is a stretch factor (black line). Decay of the magnetization vs. time for **2-Dy**, obtained by applying a magnetic field of 0.1 T to the sample at a temperature of 50 K, cooling the sample to 4.0 K, and then removing the magnetic field.

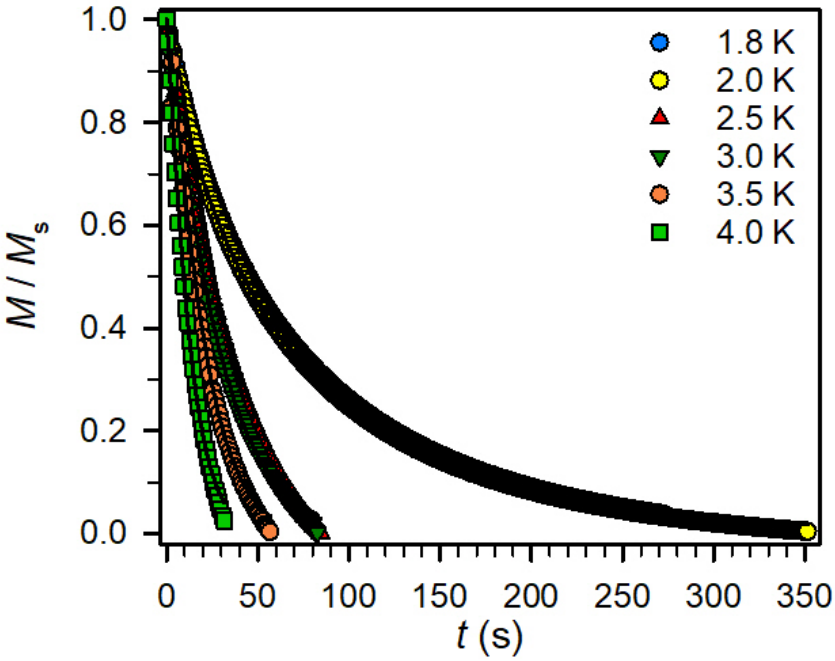

Figure S56. Plot of magnetization (normalized) vs. time used to derive relaxation times for **2-Dy** at different temperatures. The data were fit to a function of the form y = a · exp (−((t/τ)^b)) where b is a stretch factor (black line). Decay of the magnetization vs. time for **2-Dy**, obtained by applying a magnetic field of 0.1 T to the sample at a temperature of 50 K, cooling the sample to a given temperature, and then removing the magnetic field.

Table S3. Relaxation times, τ (s), and stretch factors, b, at various temperatures, T (K) for **2-Dy**.

T (K)	τ (s)	stretch factor
1.8	68.87740572	0.828653282
2.0	65.61476463	0.825878046
2.5	34.00662524	1.388001075
3.0	28.31669823	1.107648596
3.5	20.95021698	1.213686665
4.0	12.89217026	1.148894262

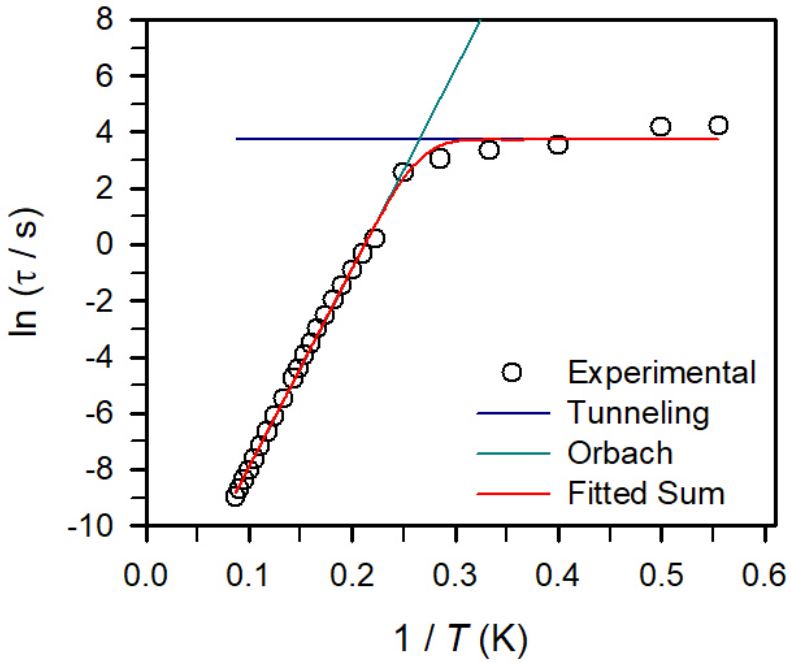

Figure S57. Individual contributions of the multiple magnetic relaxation pathways to the Arrhenius plot of **2-Dy** at 0 Oe shown in Figure 7 of the main text. The best fit yielded U_{eff} = 49.2(1) cm^{-1} and τ_0 = 3.1(1) × 10^{-7} s. The red line represents a fit to one Orbach relaxation process and a tunneling pathway. Individual parameters used to calculate the contributions are given in Table S4.

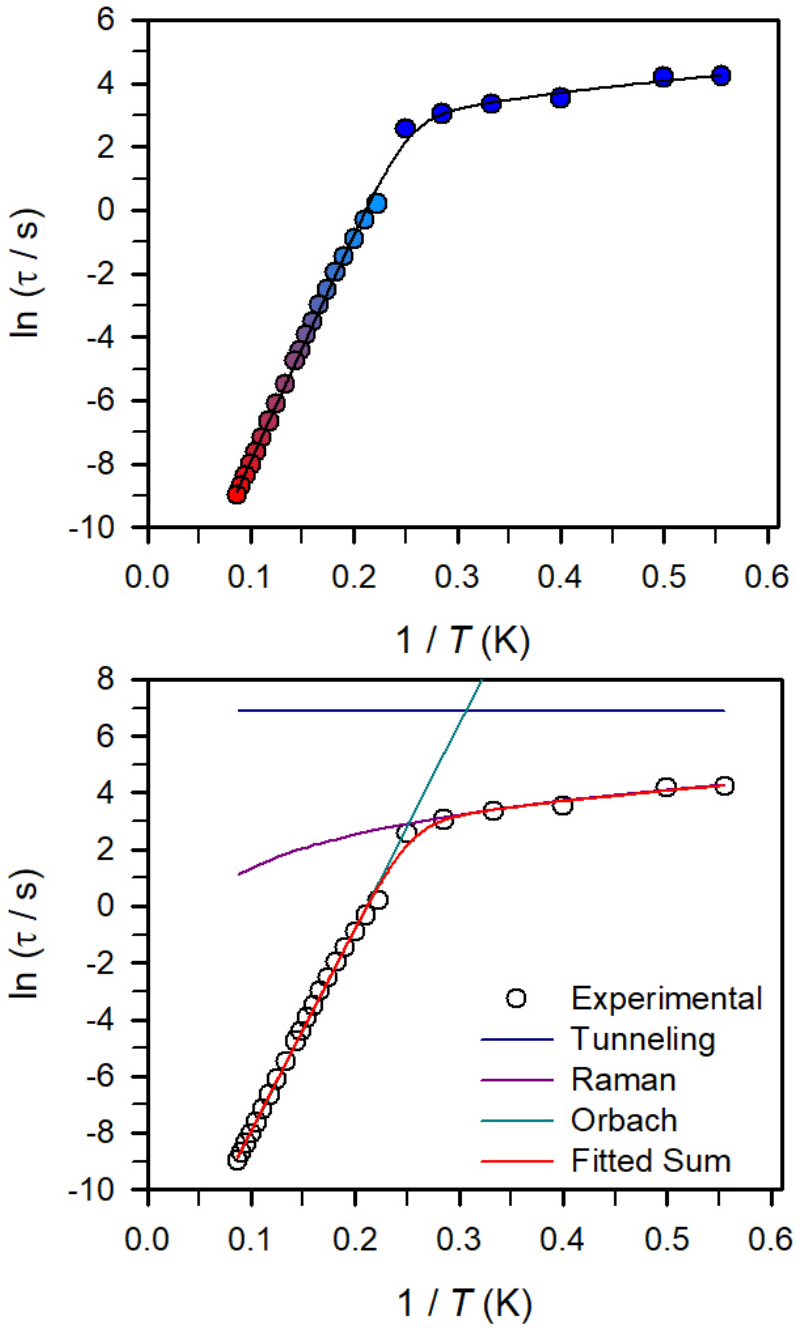

Figure S58. Arrhenius plots of relaxation time data derived from ac magnetic susceptibility measurements at temperatures from 4.5 to 11.5 K (pale blue to red circles) and dc relaxation experiments within the temperature range of 1.8 to 4 K (dark blue circles) for **2-Dy**. The black solid line (top) corresponds to a fit to one Orbach, one Raman, and one QTM process giving rise to U_{eff} = 49.9(1) cm^{-1} and τ_0 = 2.7(1) × 10^{-7} s, where the corresponding individual contributions of the multiple magnetic relaxation pathways are shown on the bottom. Individual parameters used to calculate the contributions are given in Table S4. The inclusion of a Raman process did not improve the quality of the fit.

Table S4. Best-fit parameters for the Arrhenius plot of **2-Dy** at H_{dc} = 0 Oe. Data from 4.5 to 11.5 K and from 5.5 K to 11.5 K were extracted from ac susceptibility measurements. Data from 1.8 to 11.5 K was extracted from ac and dc susceptibility measurements.

	τ_{QTM} (s)	C ($s^{-1}K^{-n}$)	n	τ_0 (s)	U_{eff} (cm^{-1})
4.5 to 11.5 K	-	-	-	$3.2\ (1) \times 10^{-7}$	48.9(1)
5.5 to 11.5 K	-	-	-	$1.91(1) \times 10^{-7}$	51.9(1)
1.8 to 11.5 K	41.7(1)	-	-	$3.1(1) \times 10^{-7}$	49.2(1)
1.8 to 11.5 K	993.8(2)	$4.9(1) \times 10^{-3}$	1.73(2)	$2.7(1) \times 10^{-7}$	49.9(1)

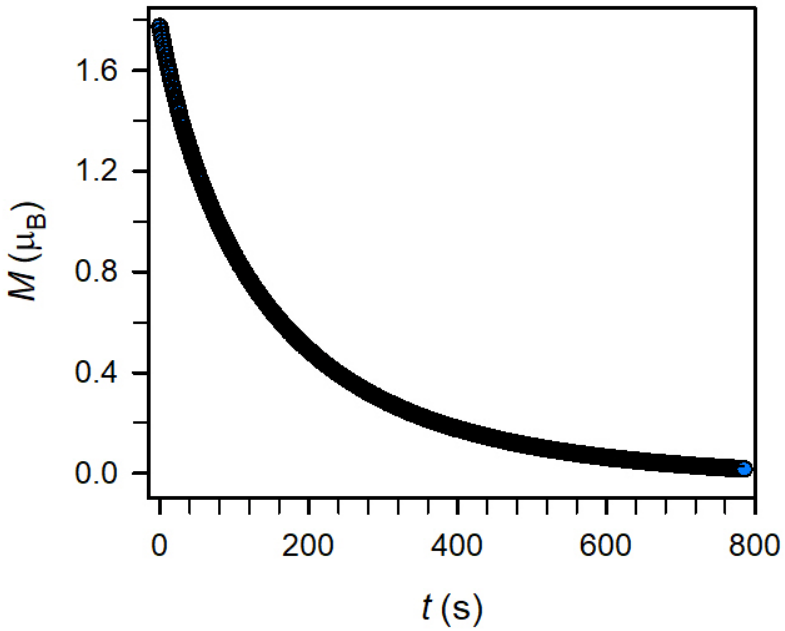

Figure S59. Plot of magnetization vs. time used to derive relaxation times for **1-Dy** at 1.8 K. The data (pale pink circles) were fit to a function of the form y = a · exp (−((t/τ)^b)) where b is a stretch factor (black line). Decay of the magnetization vs. time for **1-Dy**, obtained by applying a magnetic field of 1 T to the sample at a temperature of 50 K, cooling the sample to 1.8 K, and then removing the magnetic field.

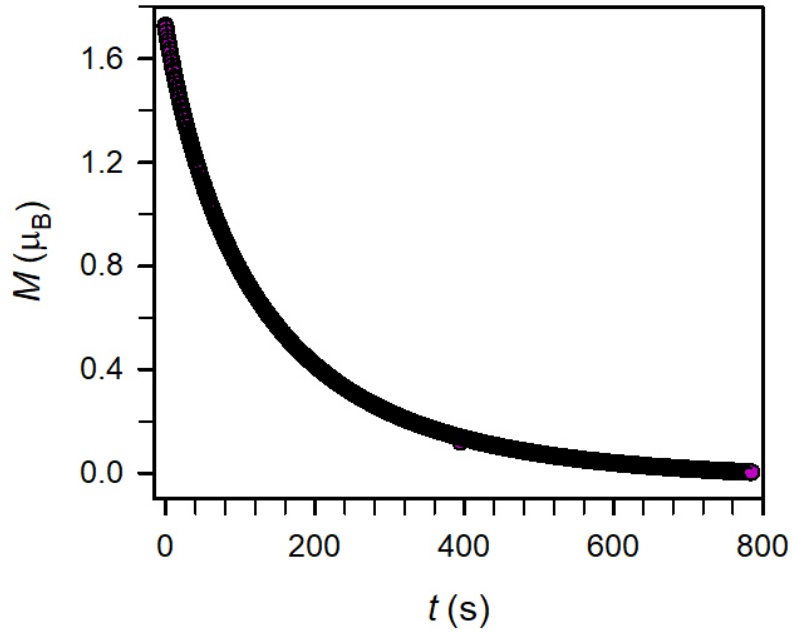

Figure S60. Plot of magnetization vs. time used to derive relaxation times for **1-Dy** at 2 K. The data (pale pink circles) were fit to a function of the form y = a · exp (−((*t*/*τ*)^{b})) where b is a stretch factor (black line). Decay of the magnetization vs. time for **1-Dy**, obtained by applying a magnetic field of 1 T to the sample at a temperature of 50 K, cooling the sample to 2 K, and then removing the magnetic field.

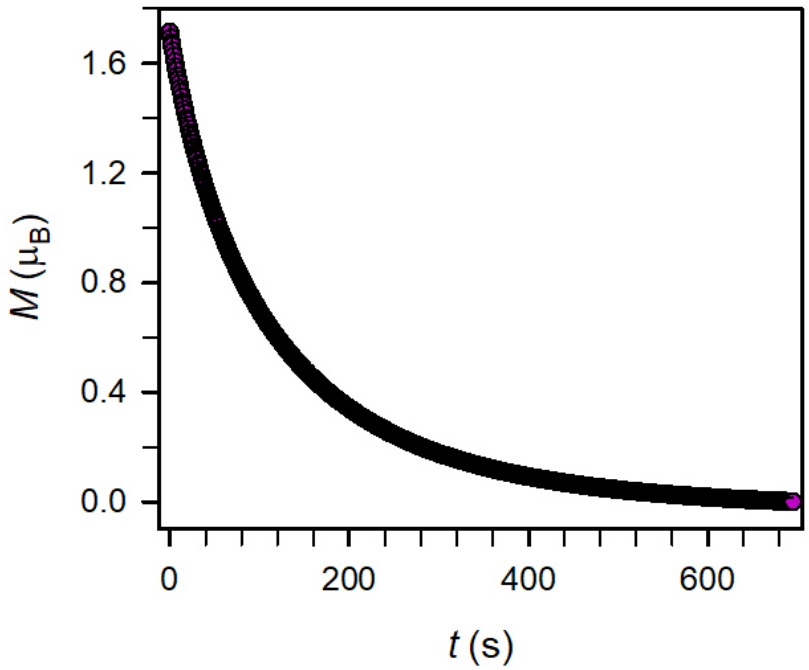

Figure S61. Plot of magnetization vs. time used to derive relaxation times for **1-Dy** at 2.2 K. The data (pale pink circles) were fit to a function of the form y = a · exp (−((*t*/*τ*)^{b})) where b is a stretch factor (black line). Decay of the magnetization vs. time for **1-Dy**, obtained by applying a magnetic field of 1 T to the sample at a temperature of 50 K, cooling the sample to 2.2 K, and then removing the magnetic field.

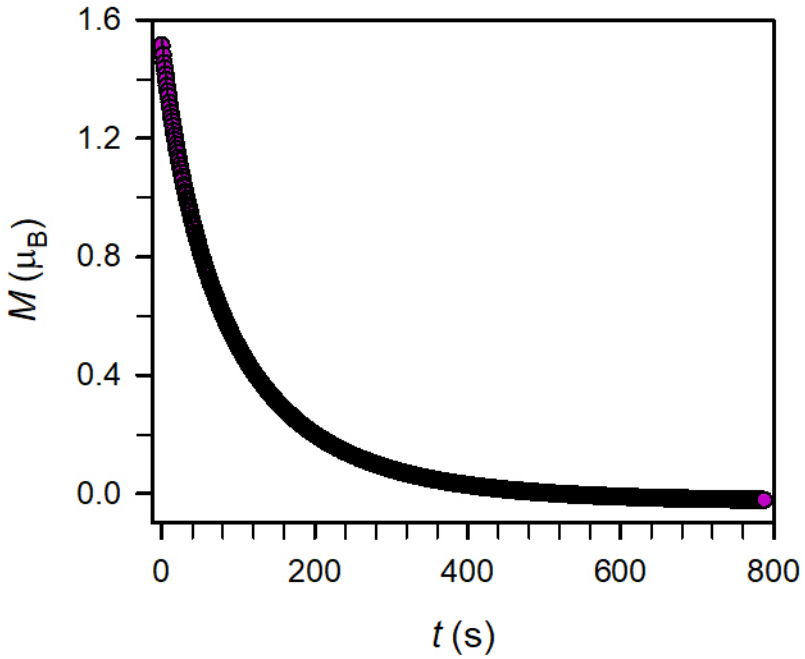

Figure S62. Plot of magnetization vs. time used to derive relaxation times for **1-Dy** at 2.5 K. The data (pale pink circles) were fit to a function of the form y = a · exp (−((t/τ)^b)) where b is a stretch factor (black line). Decay of the magnetization vs. time for **1-Dy**, obtained by applying a magnetic field of 1 T to the sample at a temperature of 50 K, cooling the sample to 2.5 K, and then removing the magnetic field.

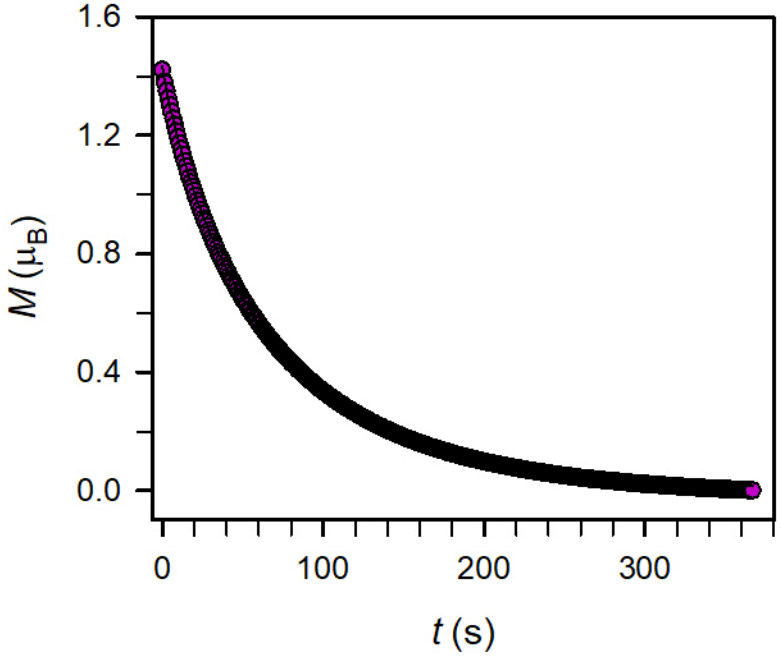

Figure S63. Plot of magnetization vs. time used to derive relaxation times for **1-Dy** at 2.75 K. The data (pale pink circles) were fit to a function of the form y = a · exp (−((t/τ)^b)) where b is a stretch factor (black line). Decay of the magnetization vs. time for **1-Dy**, obtained by applying a magnetic field of 1 T to the sample at a temperature of 50 K, cooling the sample to 2.75 K, and then removing the magnetic field.

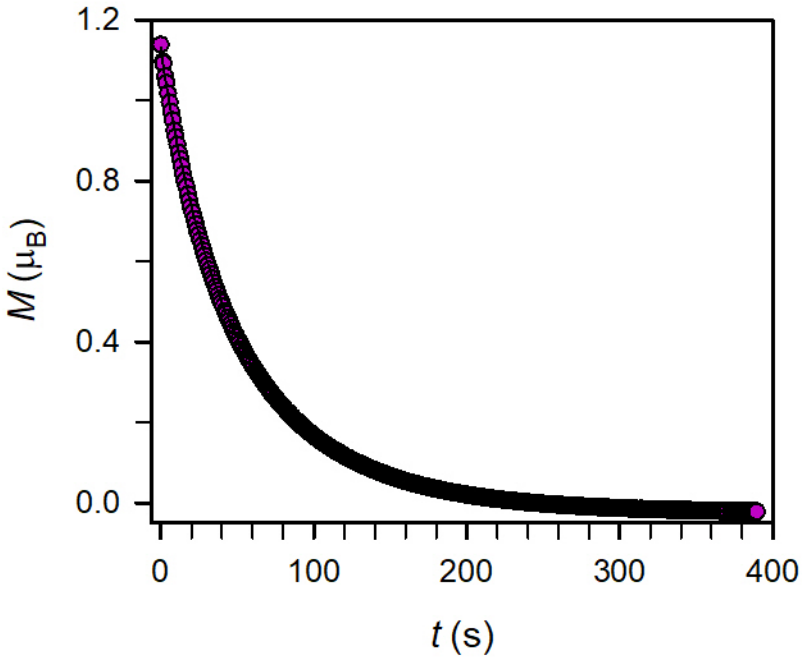

Figure S64. Plot of magnetization vs. time used to derive relaxation times for **1-Dy** at 3 K. The data (pale pink circles) were fit to a function of the form y = a · exp (−((t/τ)^b)) where b is a stretch factor (black line). Decay of the magnetization vs. time for **1-Dy**, obtained by applying a magnetic field of 1 T to the sample at a temperature of 50 K, cooling the sample to 3 K, and then removing the magnetic field.

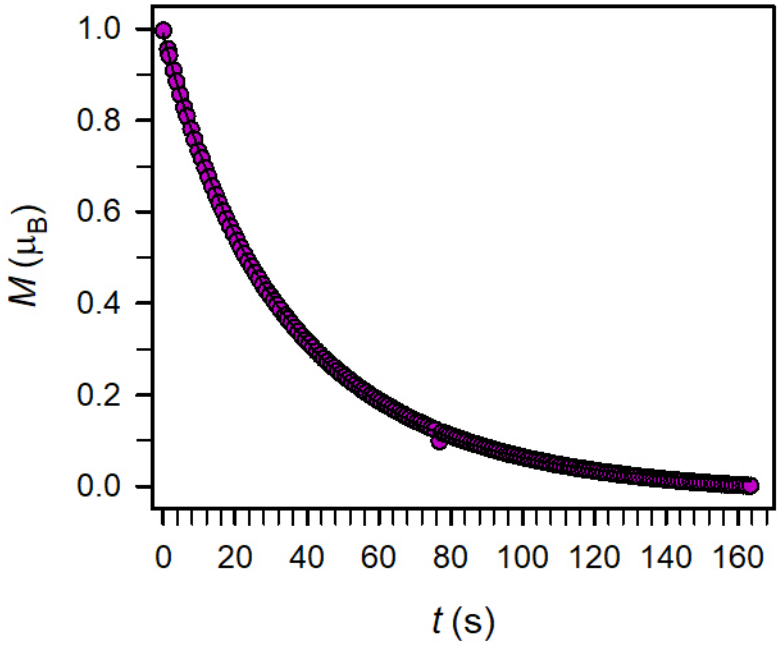

Figure S65. Plot of magnetization vs. time used to derive relaxation times for **1-Dy** at 3.25 K. The data (pale pink circles) were fit to a function of the form y = a · exp (−((t/τ)^b)) where b is a stretch factor (black line). Decay of the magnetization vs. time for **1-Dy**, obtained by applying a magnetic field of 1 T to the sample at a temperature of 50 K, cooling the sample to 3.25 K, and then removing the magnetic field.

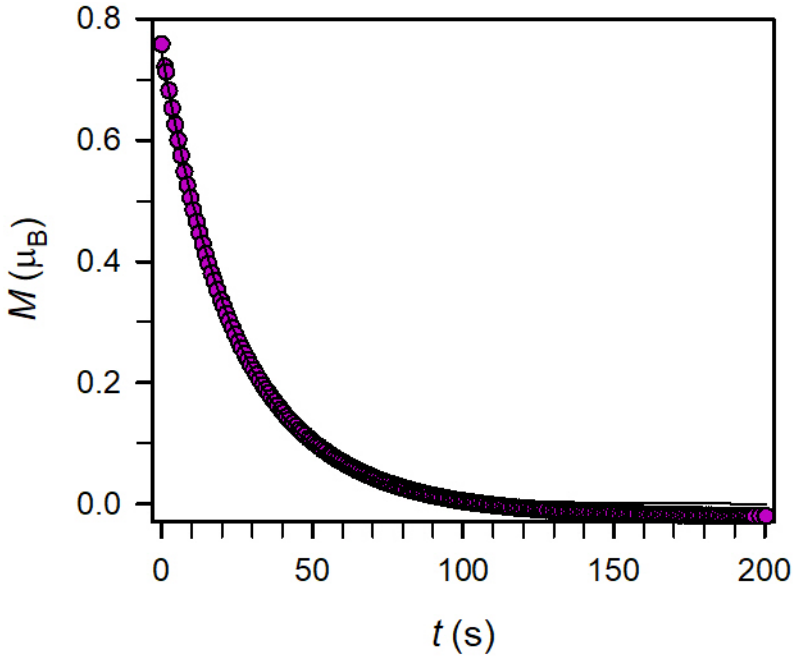

Figure S66. Plot of magnetization vs. time used to derive relaxation times for **1-Dy** at 3.5 K. The data (pale pink circles) were fit to a function of the form y = a · exp (−((t/τ)^b)) where b is a stretch factor (black line). Decay of the magnetization vs. time for **1-Dy**, obtained by applying a magnetic field of 1 T to the sample at a temperature of 50 K, cooling the sample to 3.5 K, and then removing the magnetic field.

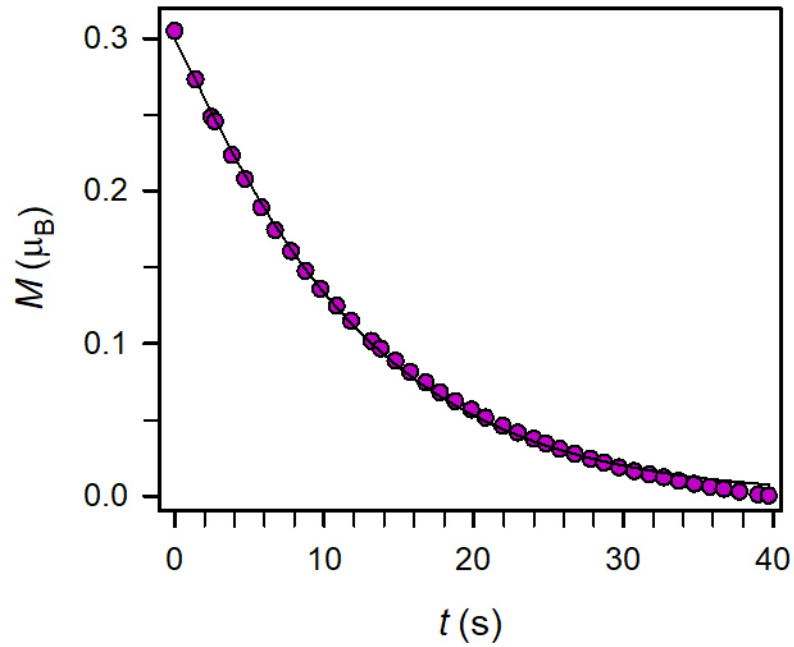

Figure S67. Plot of magnetization vs. time used to derive relaxation times for **1-Dy** at 4 K. The data (pale pink circles) were fit to a function of the form y = a · exp (−((t/τ)^b)) where b is a stretch factor (black line). Decay of the magnetization vs. time for **1-Dy**, obtained by applying a magnetic field of 1 T to the sample at a temperature of 50 K, cooling the sample to 4 K, and then removing the magnetic field.

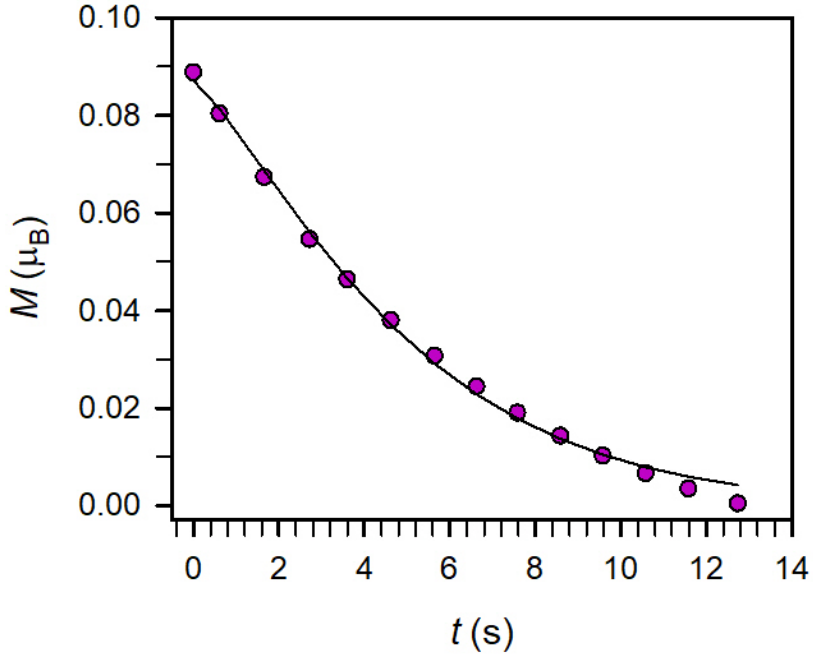

Figure S68. Plot of magnetization vs. time used to derive relaxation times for **1-Dy** at 4.5 K. The data (pale pink circles) were fit to a function of the form y = a · exp (−((*t*/*τ*)^{b})) where b is a stretch factor (black line). Decay of the magnetization vs. time for **1-Dy**, obtained by applying a magnetic field of 1 T to the sample at a temperature of 50 K, cooling the sample to 4.5 K, and then removing the magnetic field.

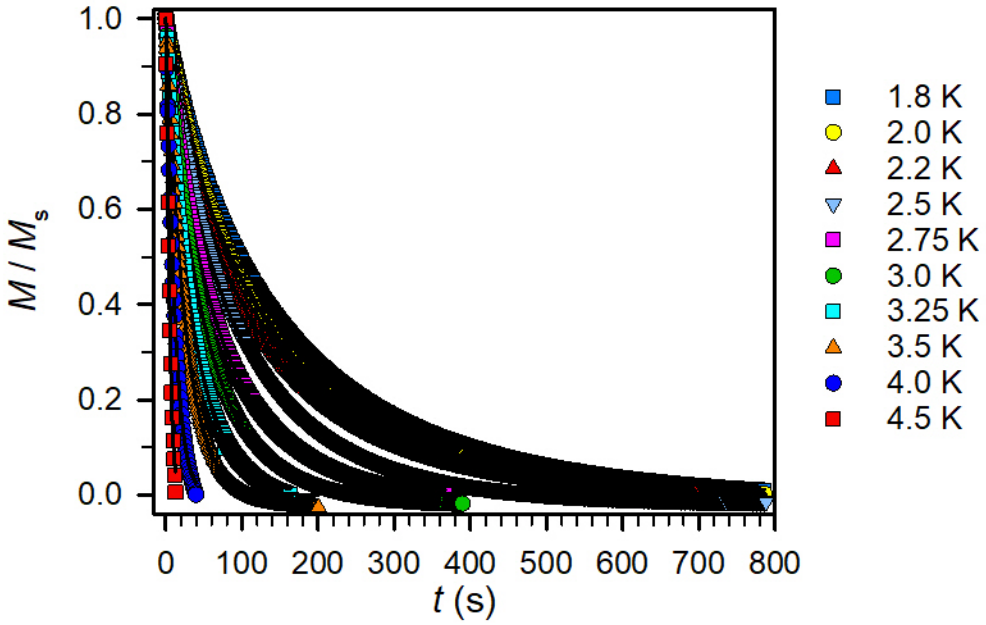

Figure S69. Plot of magnetization (normalized) vs. time used to derive relaxation times for **1-Dy** at different temperatures. The data were fit to a function of the form y = a · exp (−((*t*/*τ*)^{b})) where b is a stretch factor (black line). Decay of the magnetization vs. time for **1-Dy**, obtained by applying a magnetic field of 1 T to the sample at a temperature of 50 K, cooling the sample to a given temperature, and then removing the magnetic field.

Table S5. Relaxation times, τ (s), and stretch factors, b, at various temperatures, *T* (K) for **1-Dy**.

T (K)	τ (s)	stretch factor
1.8	146.1907	0.84552
2.0	130.2492	0.84555
2.2	111.7248	0.841136
2.5	86.93023	0.858337
2.75	65.26766	0.879887
3.0	49.3119	0.939921
3.25	34.76398	0.960858
3.5	24.93626	1.024986
4.0	12.09809	1.10035
4.5	5.240397	1.246521

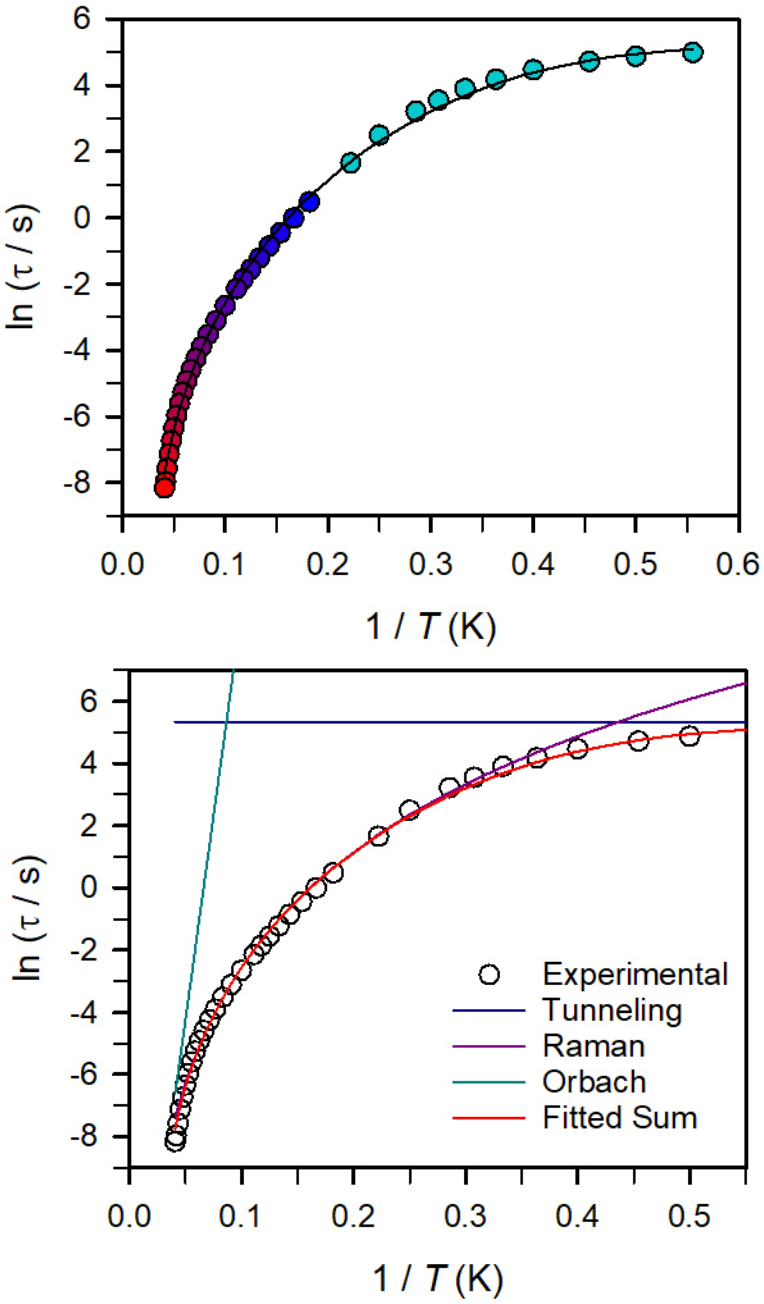

Figure S70. Individual contributions of the multiple magnetic relaxation pathways to the Arrhenius plot of **1-Dy** at 0 Oe shown in Figure 7 of the main text. The best fit yielded U_{eff} = 182.1(1) cm^{-1} and τ_0 = 3.0(1) × 10^{-8} s. The red line represents a fit to one Orbach relaxation process, a Raman process and a tunneling pathway. Individual parameters used to calculate the contributions are given in Table S6.

Table S6. Best-fit parameters for the Arrhenius plot of **1-Dy** at H_{dc} = 0 Oe. Data from 5.5 to 24.5 K was extracted from ac susceptibility measurements. Data from 1.8 to 24.5 K was extracted from ac and dc susceptibility measurements.

	τ_{QTM} (s)	C ($s^{-1}K^{-n}$)	n	τ_0 (s)	U_{eff} (cm^{-1})
5.5 to 24.5 K	-	1.6(1) x 10^{-4}	4.92(2)	1.0 (1) × 10^{-8}	185.0(1)
1.8 to 24.5 K	208.0(1)	5.5(2) x 10^{-5}	5.36(3)	3.0(1) × 10^{-8}	182.1(1)

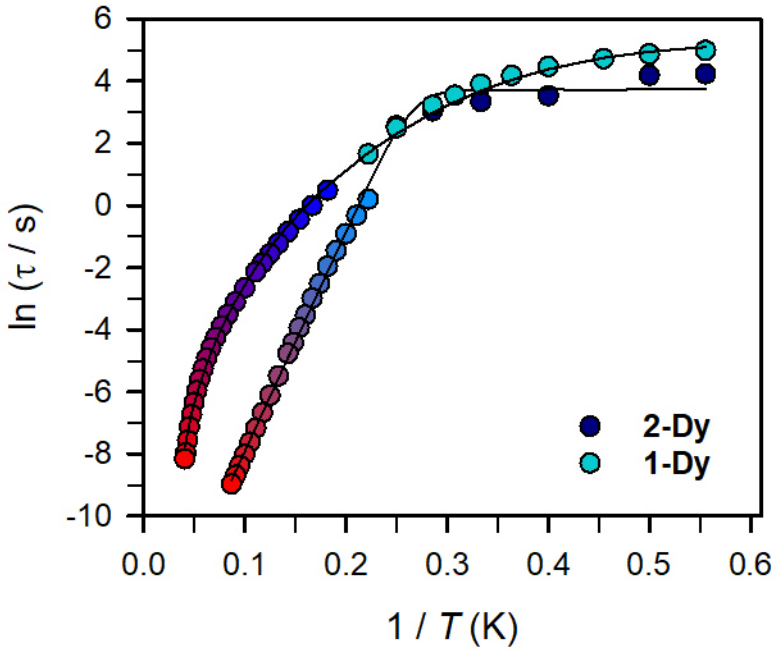

Figure S71. Comparison of all relaxation times data derived from ac magnetic susceptibility measurements and dc relaxation experiments for **1-Dy** and **2-Dy**, respectively.

CASSCF Calculations

Table S7. Computed energy levels (the ground state is set at zero) and main components (>10%) of the wavefunction for each m_J state of the ground-state multiplet $^7F_6$ for first individual Tb center of **2-Tb** at the CAS(8,7)SCF – RASSI-SO level.

	Energy (cm^{-1})	Wavefunction
1	0.0	98.6% | ± 1>
2	2.0	76.9% | ± 0> + 21.4% | ± 2>
3	51.4	95.2% | ± 1>
4	56.5	95.2% | ± 2>
5	66.6	72.4% | ± 2> + 18.7% | ± 0>
6	100.4	92.8% | ± 3>
7	122.9	91.2% | ± 3>
8	198.6	85.8% | ± 4> + 12.4% | ± 6>
9	207.0	80.2% | ± 4> + 12.8% | ± 6>
10	325.6	87.9% | ± 5>
11	326.9	86.0% | ± 5>
12	364.8	81.8% | ± 6> + 11.0% | ± 4>
13	365.3	81.7% | ± 6> + 11.6% | ± 4>

Table S8. Computed energy levels (the ground state is set at zero) and main components (>10%) of the wavefunction for each m_J state of the ground-state multiplet $^7F_6$ for second individual Tb center of **2-Tb** at the CAS(8,7)SCF – RASSI-SO level.

	Energy (cm^{-1})	Wavefunction
1	0	97.0% | ± 1>
2	1.9	74.0% | ± 0> + 22.6% | ± 2>
3	57.1	84.1% | ± 1> + 12.4% | ± 2>
4	60.8	87.7% | ± 2> + 10.5% | ± 1>
5	76.3	69.6% | ± 2> + 20.9% | ± 0>
6	107.2	93.4% | ± 3>
7	130	93.1% | ± 3>
8	208.4	89.1% | ± 4> + 10.1% | ± 6>
9	215.4	84.5% | ± 4> + 10.3% | ± 6>
10	339.1	92.0% | ± 5>
11	340.2	90.9% | ± 5>
12	384	86.8% | ± 6>
13	384.5	86.5% | ± 6>

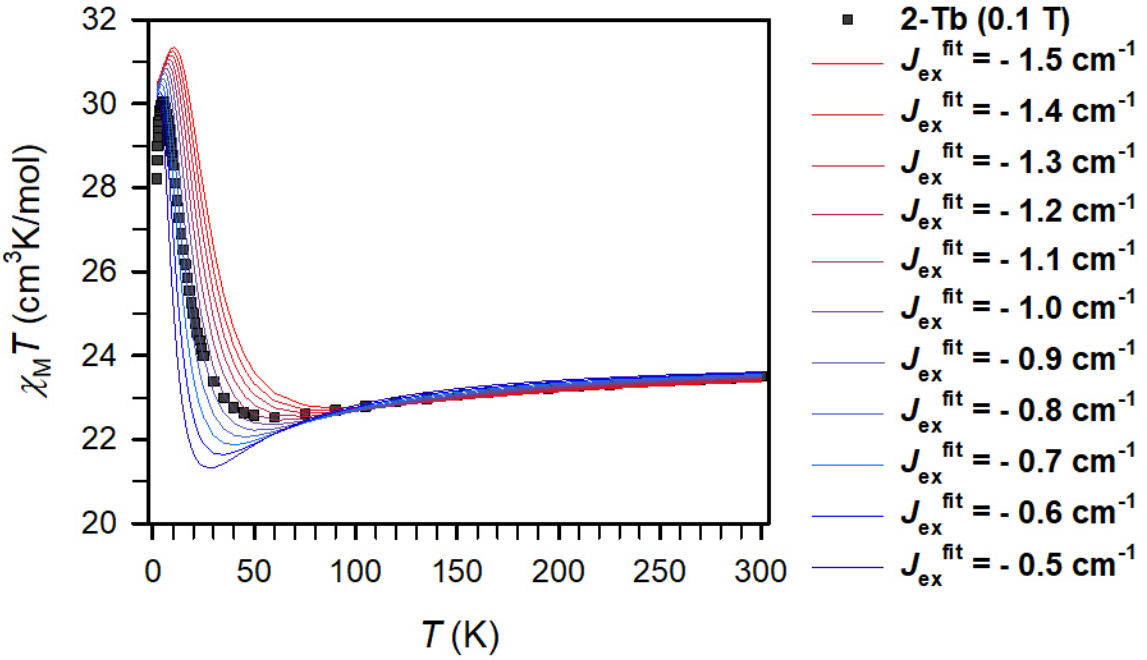

Figure S72. Variable-temperature dc magnetic susceptibility data of **2-Tb** (black squares) and calculated $\chi_M T$ data (coloured lines) for a screening of the J_{ex}^{fit} value from −1.5 cm^{-1} to −0.5 cm^{-1}.

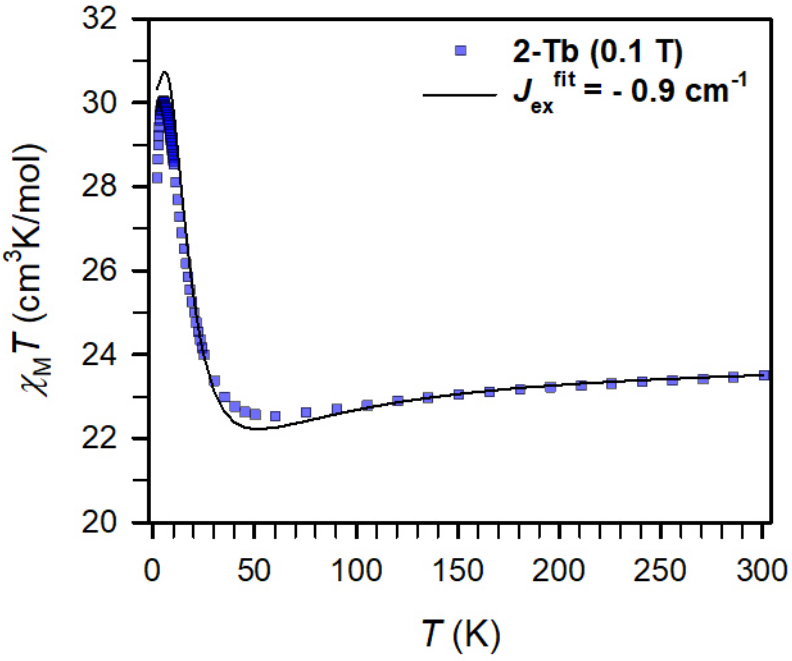

Figure S73. Variable-temperature dc magnetic susceptibility data of **2-Tb** (blue squares) with the best fit (black solid line) for J_{ex}^{fit} = −0.9 cm^{-1}.

Table S9. Computed energy levels (the ground state is set at zero) and composition of the *g*-tensor (g_x, g_y, g_z) of the low-lying exchange energy levels for **2-Tb**.

	Energy (cm^{-1})	*g*		
1	0.0	0.0	0.0	31.0
2	23.8	0.0	0.0	3.3
3	25.3	0.0	0.0	1.5
4	46.9	0.0	0.0	32.1

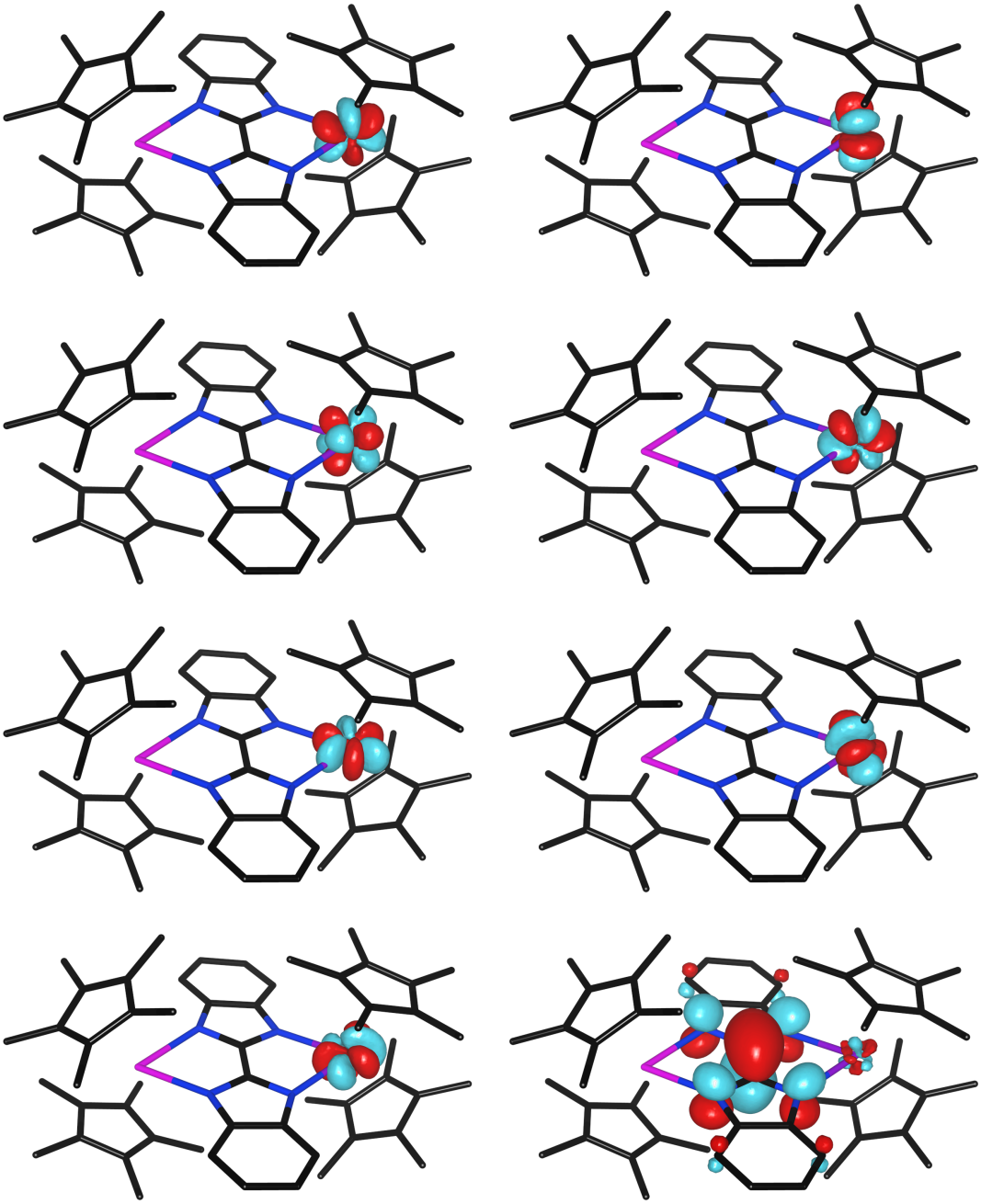

Figure S74. Isosurfaces (±0.045) of computed active molecular orbitals of the sextet state of **2-Tb** at the CAS(9,8)SCF level. Colour codes: Tb, purple; Y, pink; N, blue; C, black. Hydrogen atoms are not represented for clarity.

Table S10. Computed energy levels (the ground state is set at zero), composition of the *g*-tensor (g_x, g_y, g_z) and main components (>10%) of the wavefunction for each m_j state of the ground-state multiplet $^6H_{15/2}$ for first individual Dy center of **2-Dy** at the CAS(9,7)SCF – RASSI-SO level.

KD	Energy (cm^{-1})	*g*			Wavefunction
1	0.0	0.0	0.1	18.6	76.7% | ± 15/2> + 22.3% | ± 11/2>
2	73.4	1.4	3.5	13.3	64.3% | ± 13/2> + 15.4% | ± 9/2> + 11.8% | ± 1/2>
3	95.1	1.7	2.4	14.8	42.5% | ± 1/2> + 31.5% | ± 3/2> + 17.6% | ± 13/2>
4	161.6	0.3	0.5	15.7	36.7% | ± 5/2> + 24.7% | ± 3/2> + 21.7% | ± 7/2>
5	186.7	3.3	6.7	10.4	33.8% | ± 7/2> + 31.8% | ± 11/2> + 11.8% | ± 5/2>
6	214.4	0.7	4.1	11.0	39.1% | ± 9/2> + 24.4% | ± 11/2>
7	268.2	0.4	0.9	16.2	26.7% | ± 7/2> + 26.5% | ± 9/2> + 17.3% | ± 11/2> + 13.7% | ± 5/2>
8	465.6	0.0	0.0	19.8	34.1% | ± 1/2> + 28.5% | ± 3/2> + 19.6% | ± 5/2> + 10.6% | ± 7/2>

Table S11. Computed energy levels (the ground state is set at zero), composition of the *g*-tensor (g_x, g_y, g_z) and main components (>10%) of the wavefunction for each m_j state of the ground-state multiplet $^6H_{15/2}$ for second individual Dy center of **2-Dy** at the CAS(9,7)SCF – RASSI-SO level.

KD	Energy (cm^{-1})	*g*			Wavefunction
1	0.0	0.0	0.1	18.5	75.5% | ± 15/2> + 23.7% | ± 11/2>
2	71.5	1.7	4.3	12.5	58.9% | ± 13/2> + 15.9% | ± 9/2> + 15.6% | ± 1/2>
3	93.5	2.0	3.1	13.7	40.6% | ± 1/2> + 30.2% | ± 3/2> + 23.0% | ± 13/2>
4	159.4	0.1	0.3	15.7	41.0% | ± 5/2> + 28.2% | ± 3/2> + 18.7% | ± 7/2>
5	185.4	3.6	6.6	10.9	41.4% | ± 7/2> + 25.8% | ± 11/2> + 12.5% | ± 5/2>
6	212.0	0.3	3.8	11.0	41.2% | ± 9/2> + 28.4% | ± 11/2>
7	262.8	0.5	1.2	16.0	26.1% | ± 7/2> + 25.8% | ± 9/2> + 18.5% | ± 11/2> + 13.5% | ± 5/2>
8	459.8	0.0	0.0	19.8	34.4% | ± 1/2> + 28.7% | ± 3/2> + 19.5% | ± 5/2> + 10.4% | ± 7/2>

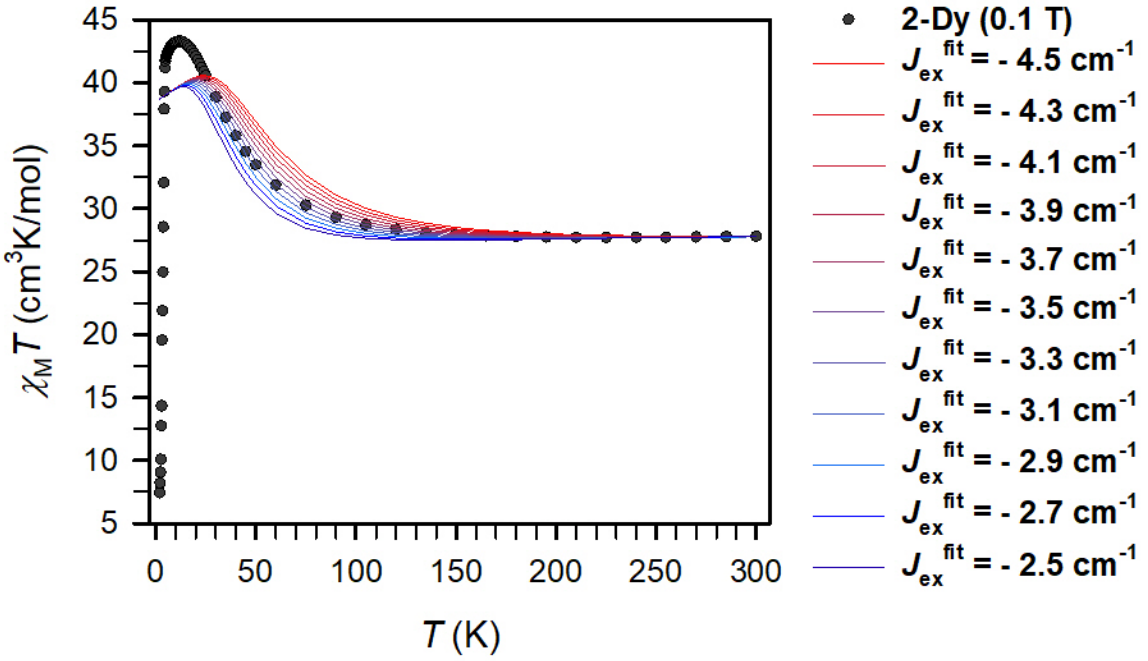

Figure S75. Variable-temperature dc magnetic susceptibility data of **2-Dy** (black circles) and calculated $\chi_M T$ data (coloured lines) for a screening of the J_{ex}^{fit} value from −4.5 cm^{-1} to −2.5 cm^{-1}.

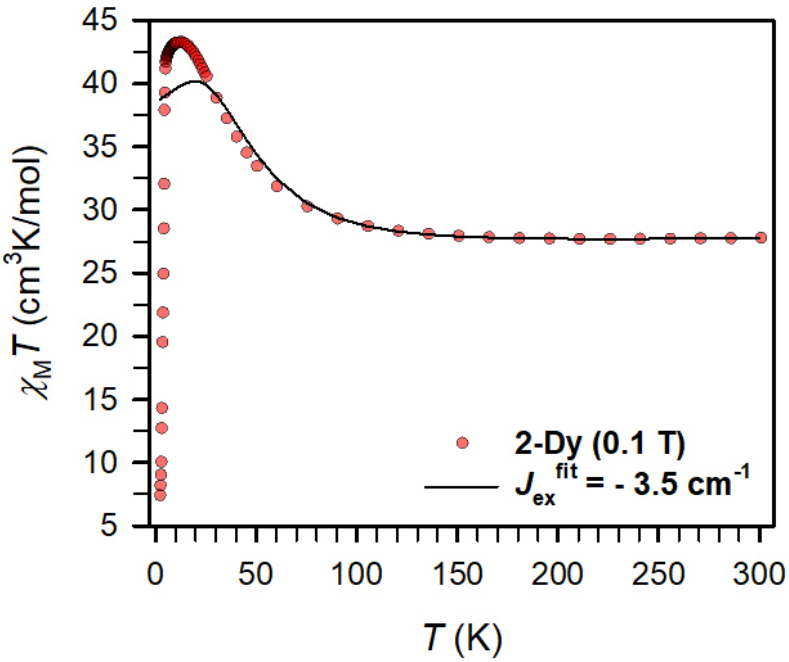

Figure S76. Variable-temperature dc magnetic susceptibility data of **2-Dy** (red circles) with the best fit (black solid line) for J_{ex}^{fit} = −3.5 cm^{-1}.

Table S12. Computed energy levels (the ground state is set at zero) and composition of the *g*-tensor (g_x, g_y, g_z) of the low-lying exchange energy levels for **2-Dy**.

KD	Energy (cm^{-1})	*g*		
1	0.0	0.0	0.0	35.1
2	72.5	0.0	0.3	5.7
3	75.2	0.0	0.6	29.3
4	76.2	0.0	2.0	4.3

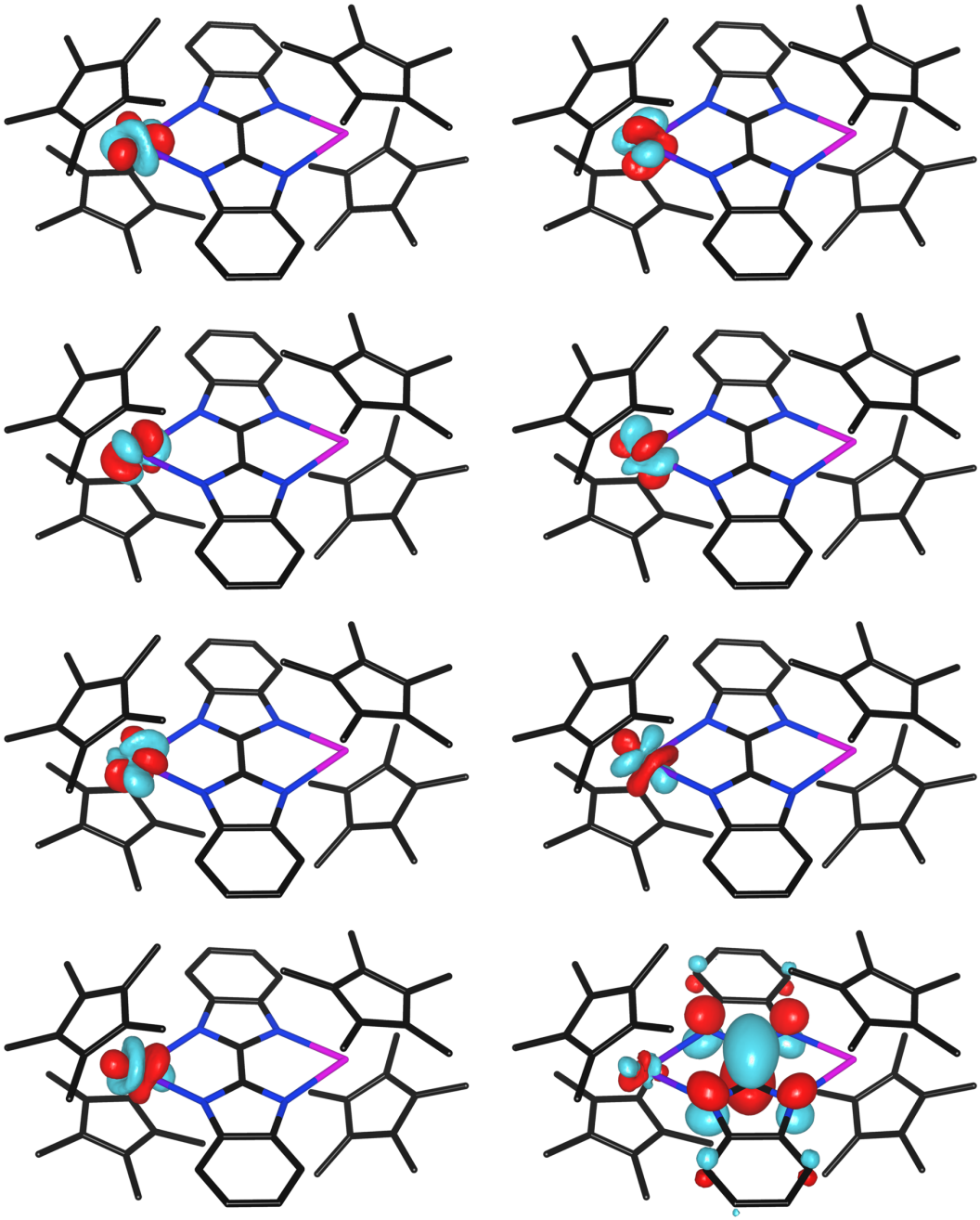

Figure S77. Isosurfaces (±0.045) of computed active molecular orbitals of the quintet state of **2-Dy** at the CAS(10,8)SCF level. Colour codes: Dy, purple; Y, pink; N, blue; C, black. Hydrogen atoms are not represented for clarity.

Table S13. Computed energy levels (the ground state is set at zero) and composition of the *g*-tensor (g_x, g_y, g_z) of the low-lying exchange energy levels for **2-Dy**.

	ΔE (cm^{-1})	J_{ex}^{calc} (cm^{-1})
2-Gd	-71.53	-8.9
2-Tb	−33.8	−4.8
2-Dy	−10.7	−1.8

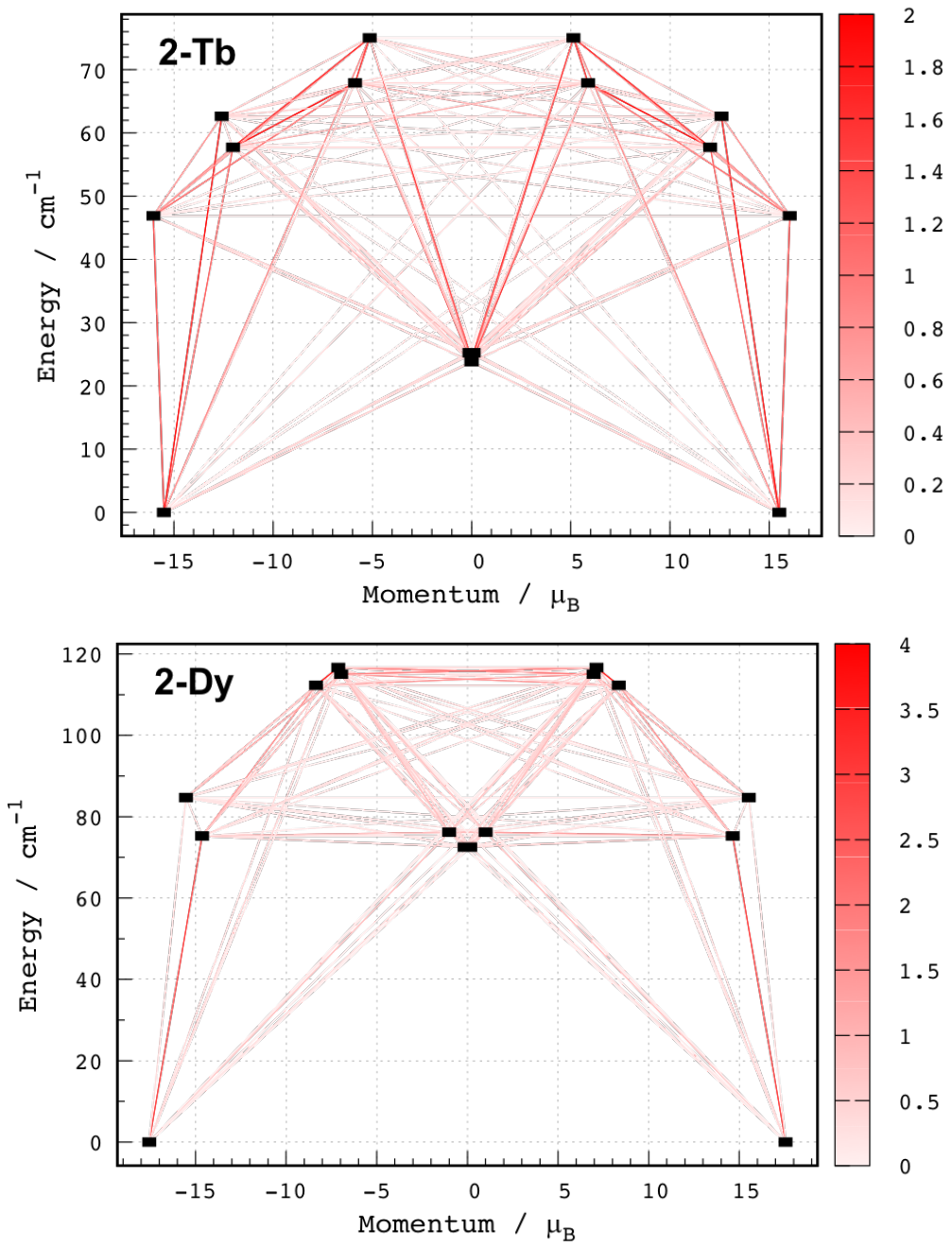

Figure S78. Low-lying exchange spectra calculated in **2-Tb** (top) and **2-Dy** (bottom). Energies of the exchange states (in cm^{-1}) in function of their magnetic moments (in μ_B) are in bold black lines. The red lines correspond to the most probable relaxation pathways. The intensity of the red lines indicates the amplitude of the matrix elements connecting each exchange doublet.

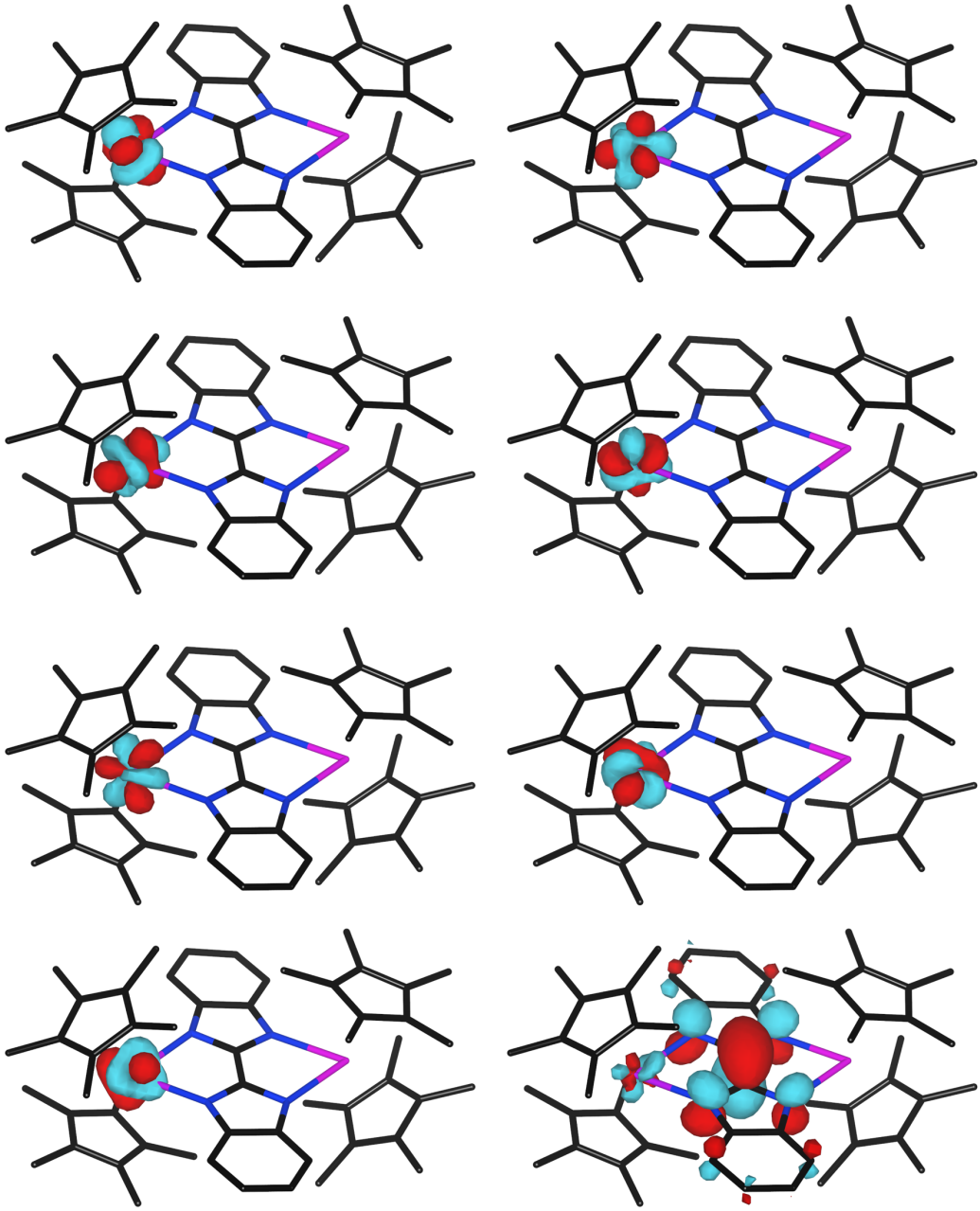

Figure S79. Isosurfaces (±0.045) of computed active molecular orbitals of the sextet state of **2-Gd** at the CAS(8,8)SCF level. Color codes: Gd, purple; Y, pink; N, blue; C, black. Hydrogen atoms are not represented for clarity.

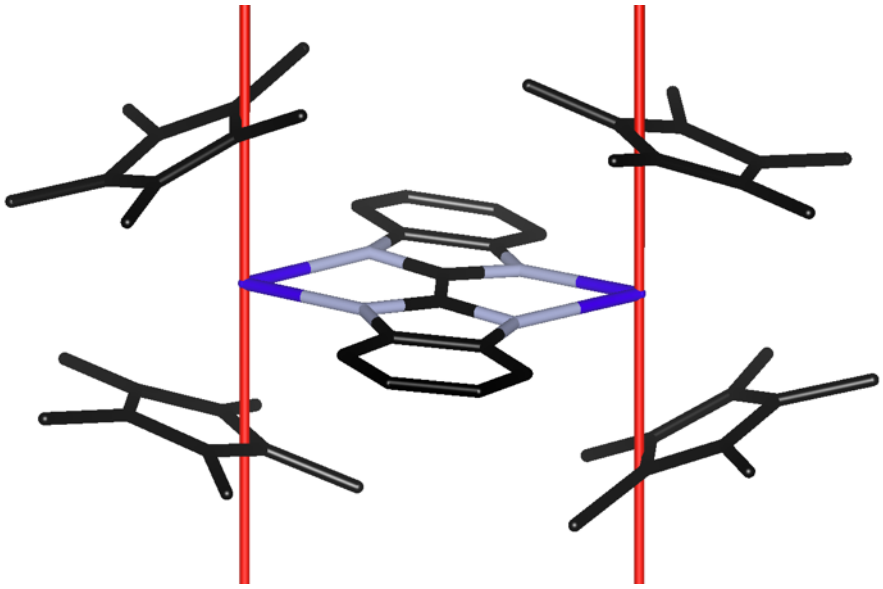

Figure S80. Ground state magnetic anisotropy axes representation projected on molecular structures for **2-Dy** at the CAS(9,7)SCF level. Colour codes: Dy, purple; Y, pink; N, blue; C, black. Hydrogen atoms are not represented for clarity.

Table S14. Computed energy levels (the ground state is set at zero), composition of the *g*-tensor (g_x, g_y, g_z) and main components (>10%) of the wavefunction for each m_j state of the ground-state multiplet $^6H_{15/2}$ for first individual Dy center of **1-Dy** at the CAS(9,7)SCF – RASSI-SO level.

KD	Energy (cm^{-1})	*g*			Wavefunction
1	0.0	0.0	0.0	19.5	91.7% |±15/2>
2	160.3	0.0	0.0	16.7	91.0% |±13/2>
3	298.3	10.4	6.9	1.8	55.5% |±11/2> + 15.5% |±7/2> + 10.0% |±1/2>
4	309.0	2.0	3.8	12.7	30.3% |±1/2> + 26.2% |±11/2> + 25.7% |±3/2> + 13.4% |±5/2>
5	363.2	3.0	3.9	9.7	69.7% |±9/2> + 12.3% |±5/2>
6	387.9	3.4	5.9	11.8	47.9% |±7/2> + 16.0% |±5/2> + 13.5% |±1/2> + 11.3% |±3/2>
7	466.0	0.1	0.2	17.2	34.4% |±5/2> + 26.6% |±7/2> + 19.2% |±3/2> + 10.6% |±9/2>
8	725.1	0.0	0.0	19.8	40.6% |±1/2> + 30.8% |±3/2> + 17.5% |±5/2>

Table S15. Computed energy levels (the ground state is set at zero), composition of the *g*-tensor (g_x, g_y, g_z) and main components (>10%) of the wavefunction for each m_J state of the ground-state multiplet $^6H_{15/2}$ for second individual Dy center of **1-Dy** at the CAS(9,7)SCF – RASSI-SO level.

KD	Energy (cm^{-1})	*g*			Wavefunction
1	0.0	0.0	0.0	19.4	91.2% |±15/2>
2	157.5	0.0	0.0	16.6	90.0% |±13/2>
3	289.3	1.9	5.0	14.2	25.4% |±11/2> + 23.4% |±1/2> + 18.0% |±3/2> + 16.2% |±7/2> + 13.1% |±5/2>
4	300.8	8.9	5.6	2.2	53.5% |±11/2> + 16.9% |±1/2> + 14.0% |±3/2>
5	355.9	4.6	5.5	8.9	62.7% |±9/2> + 15.4% |±5/2>
6	381.9	2.7	4.0	13.1	43.4% |±7/2> + 14.6% |±1/2> + 13.6% |±5/2> + 11.0% |±9/2> + 10.3% |±3/2>
7	462.7	0.2	0.2	17.2	33.3% |±5/2> + 26.8% |±7/2> + 18.5% |±3/2> + 11.5% |±9/2>
8	721.9	0.0	0.0	19.8	40.3% |±1/2> + 30.7% |±3/2> + 17.5% |±5/2>

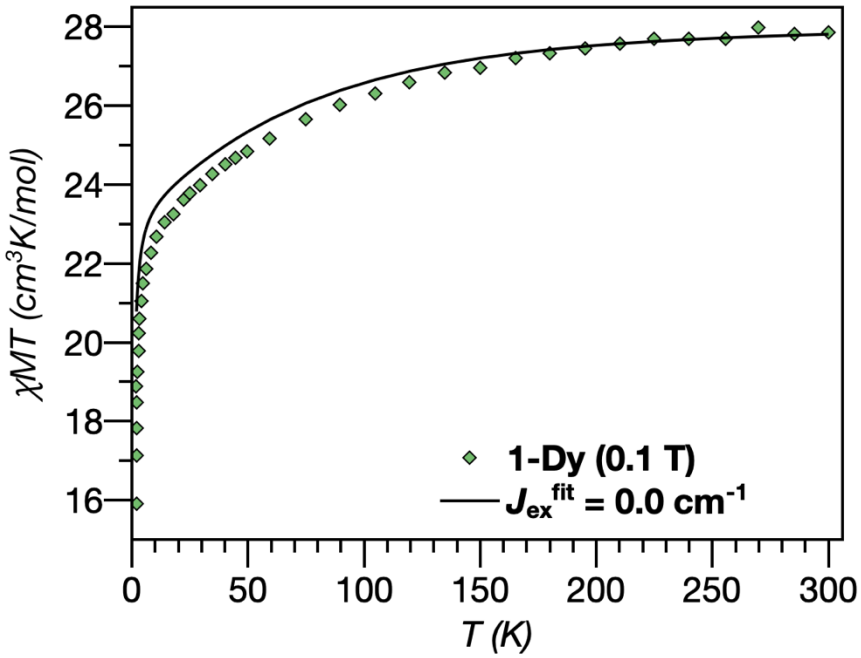

Figure S81. Variable-temperature dc magnetic susceptibility data of **1-Dy** (green diamonds) with the simulated curve (black solid line) for J_{ex}^{fit} = 0.0 cm^{-1}.

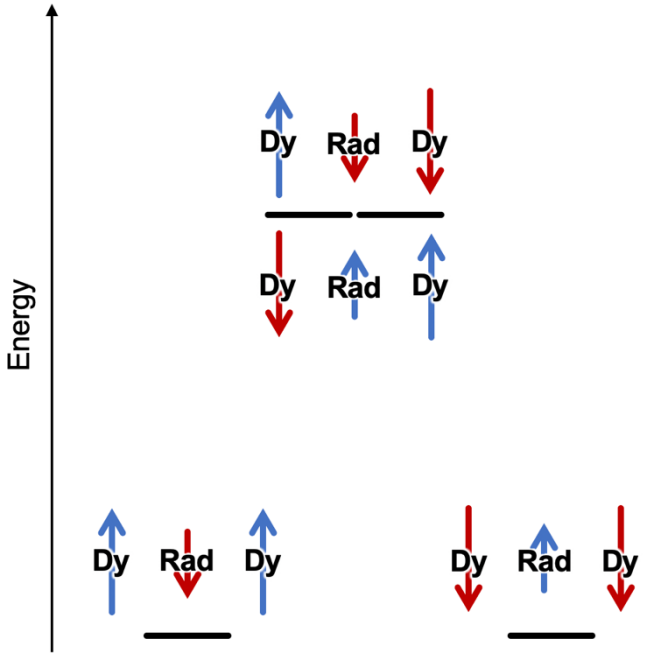

Figure S82. Schematic representation of the first two magnetic exchange energy levels of **2-Dy**. Arrows represent the orientation of the magnetic moments of each individual contribution for the three magnetic centres.

Variable-Field Magnetization Measurements

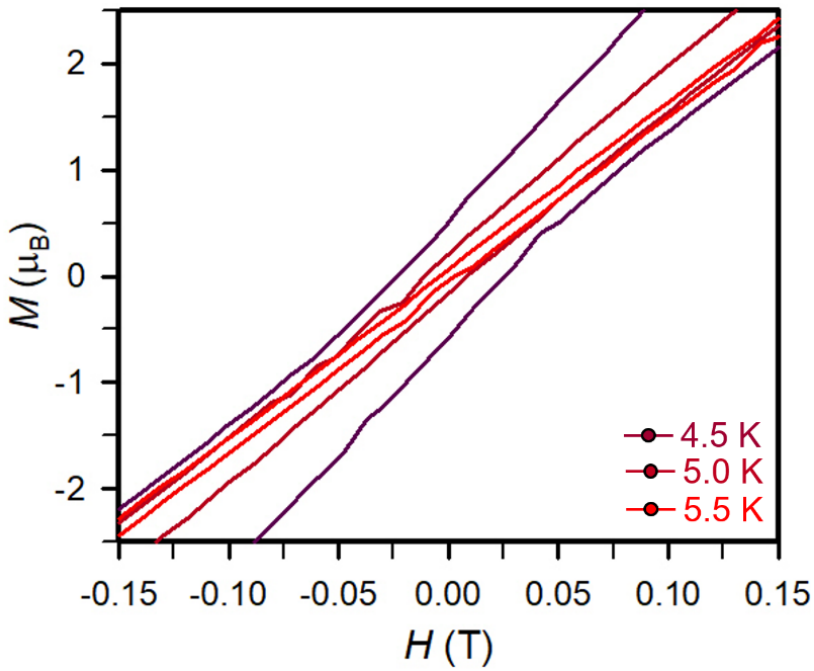

Figure S83. Magnification of variable-field magnetization data for **2-Dy** at an average sweep rate of 100 Oe/s.

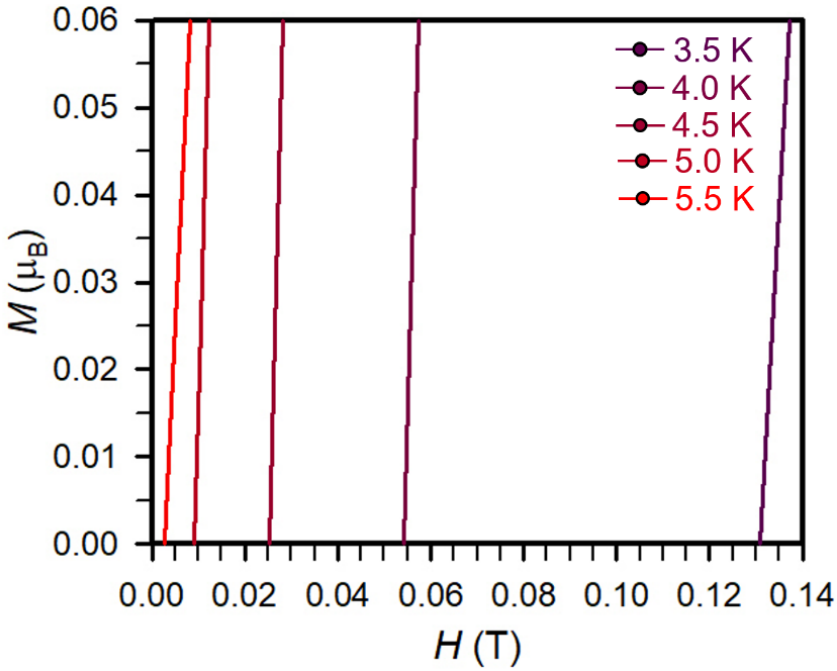

Figure S84. Magnification of variable-field magnetization data for **2-Dy** at an average sweep rate of 100 Oe/s.

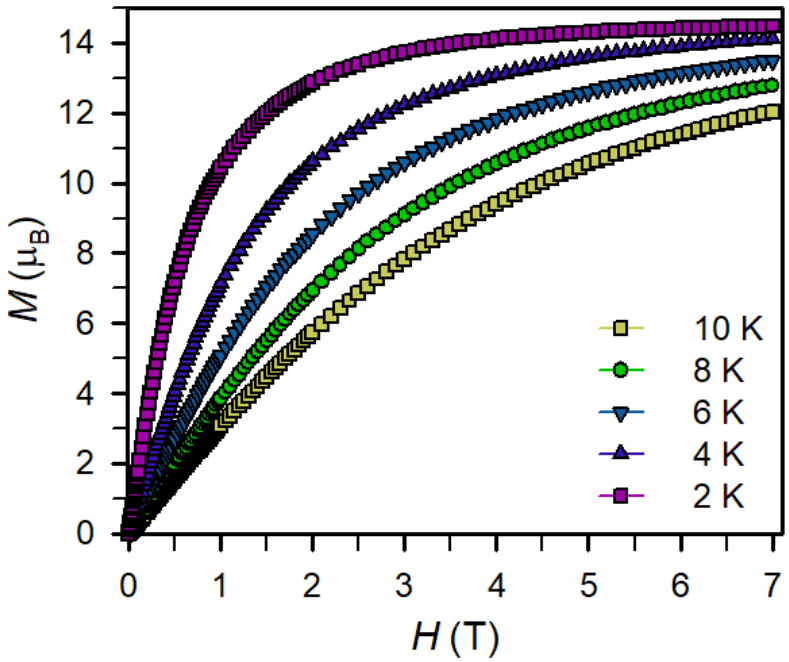

Figure S85. Variable temperature *M*(*H*) curves for **2-Gd** collected from 0 to 7 T.

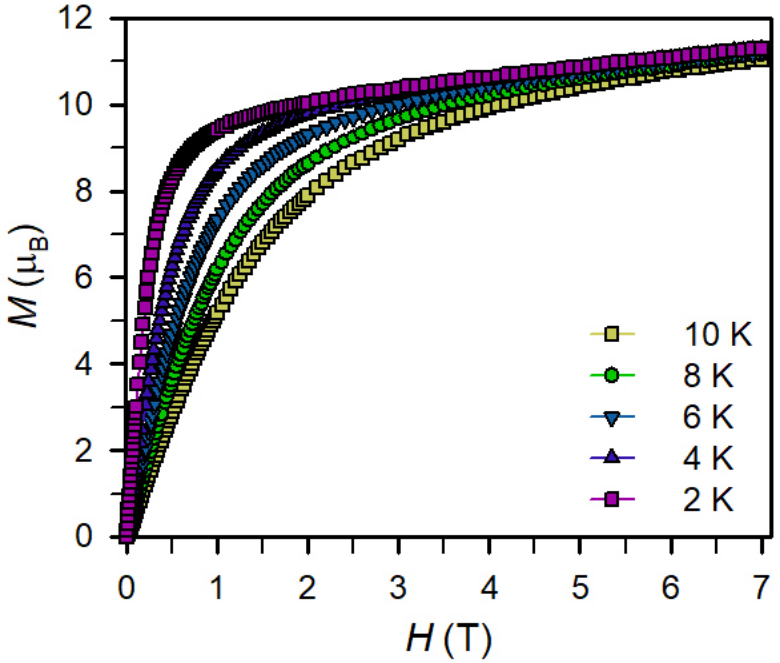

Figure S86. Variable temperature *M*(*H*) curves for **2-Tb** collected from 0 to 7 T.

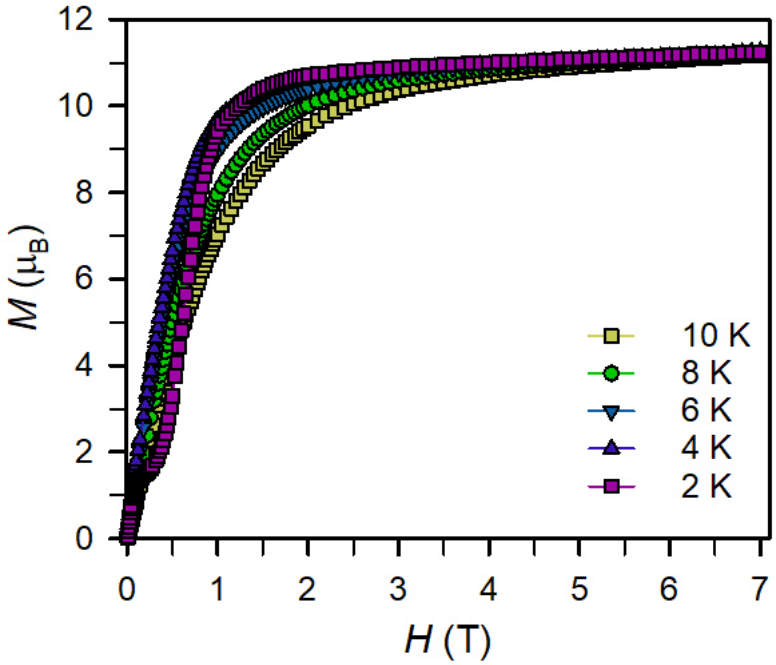

Figure S87. Variable temperature *M*(*H*) curves for **2-Dy** collected from 0 to 7 T.

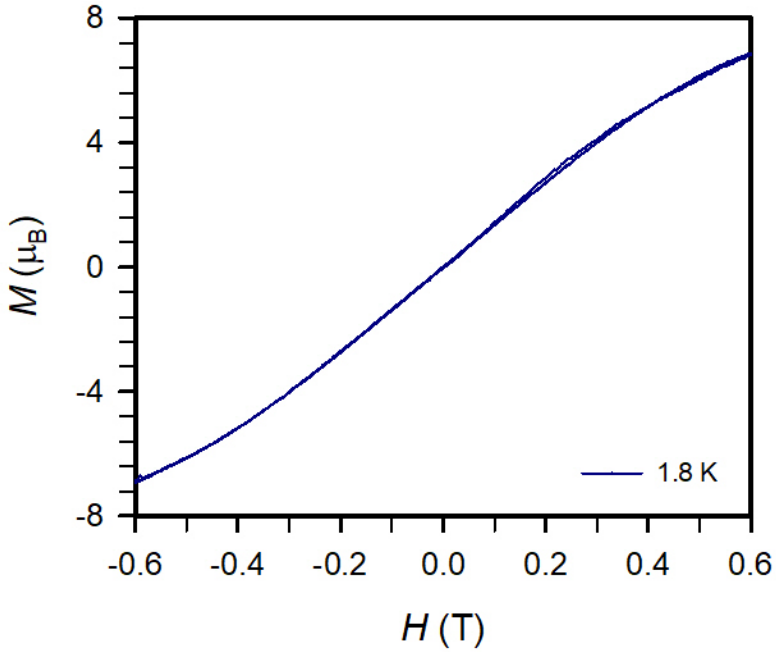

Figure S88. Variable-field magnetization (*M*) data for compound **1-Tb** collected at 1.8 K at an average sweep rate of 0.01 T/s.

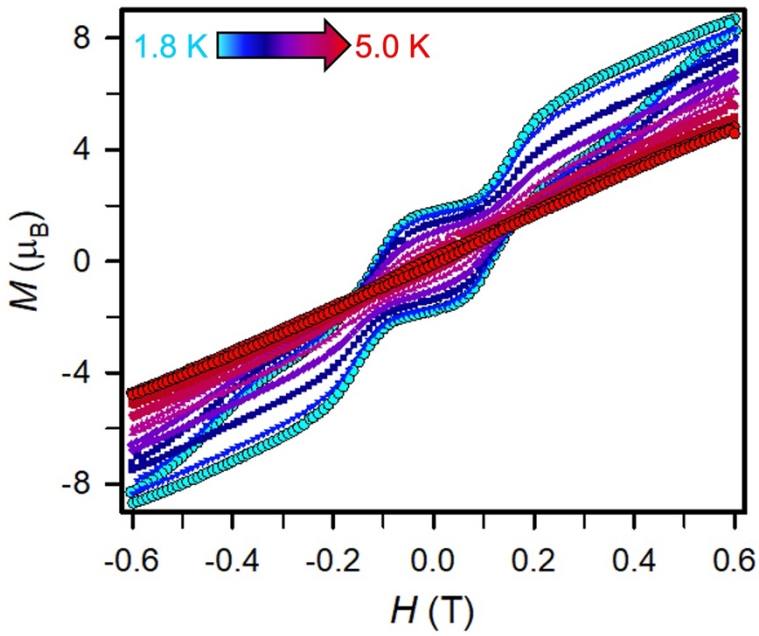

Figure S89. Variable-field magnetization (*M*) data for compound **1-Dy** collected from 1.8 to 5.0 K at an average sweep rate of 0.01 T/s.

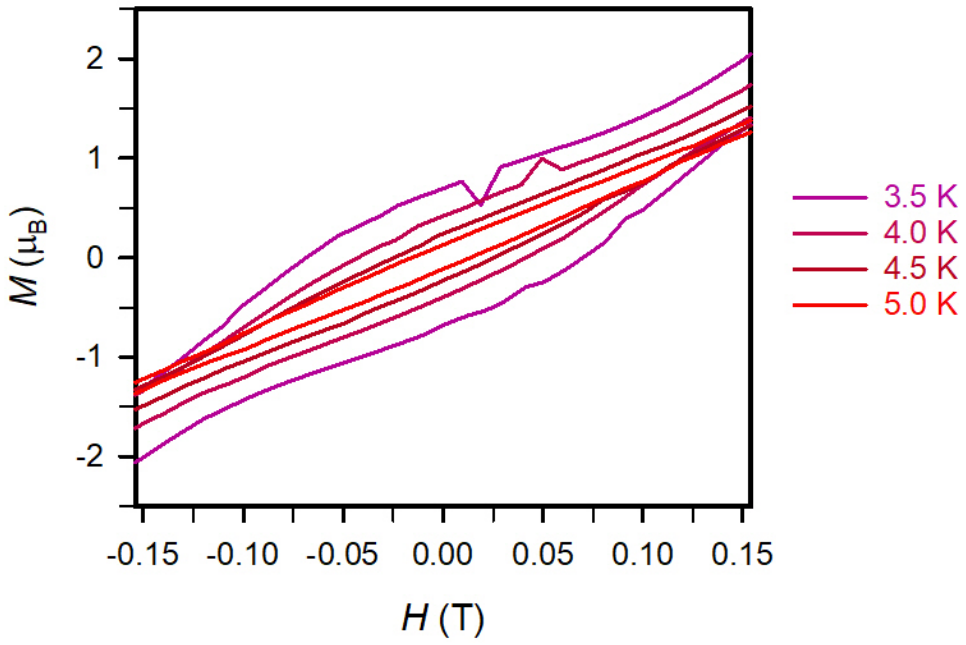

Figure S90. Magnification of variable-field magnetization data for **1-Dy** at an average sweep rate of 100 Oe/s.

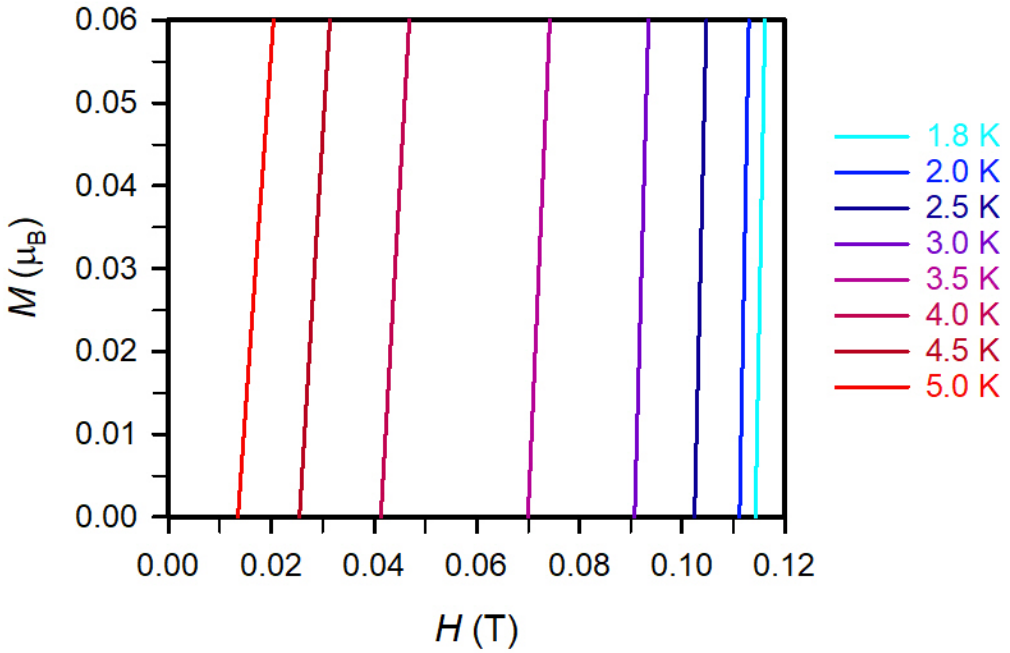

Figure S91. Magnification of variable-field magnetization data for **1-Dy** at an average sweep rate of 100 Oe/s.

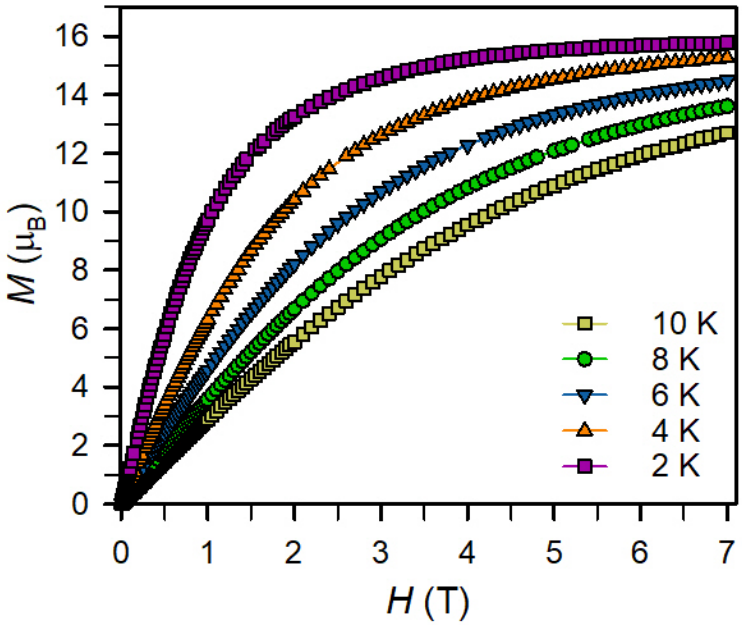

Figure S92. Variable temperature *M*(*H*) curves for **1-Gd** collected from 0 to 7 T.

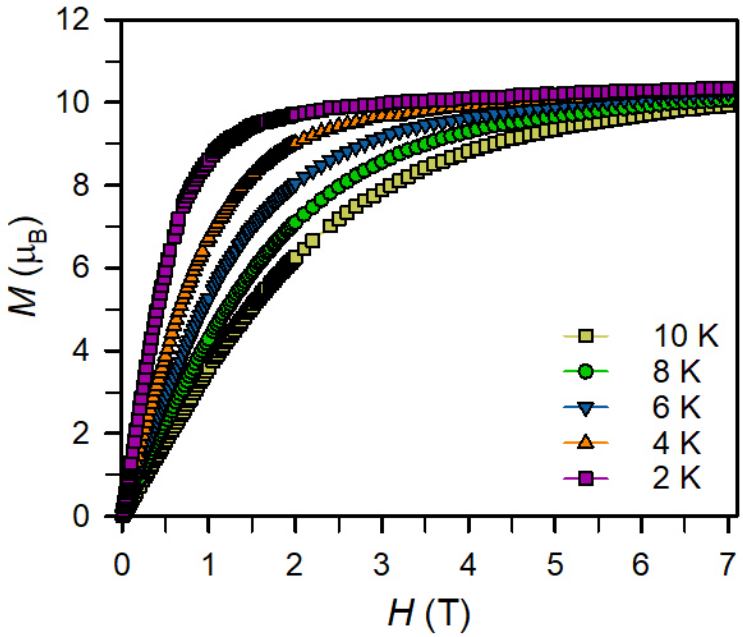

Figure S93. Variable temperature *M*(*H*) curves for **1-Tb** collected from 0 to 7 T.

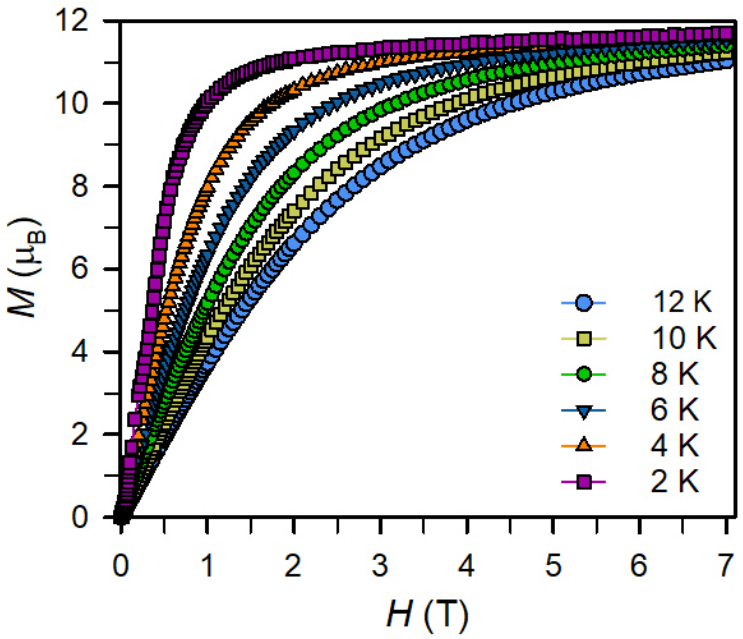

Figure S94. Variable temperature *M*(*H*) curves for **1-Dy** collected from 0 to 7 T.

Additional Structural Comparison

Table S16. Comparison of bond metrics of $[(Cp^*_2Ln)_2(\mu\text{-bpym}^\bullet)]BPh_4$,[2] $[(Cp^*_2Ln)_2(\mu\text{-tppz}^\bullet)]BPh_4$[3] and **2-Dy**.

	Dy bpym	**Dy tppz**	**2-Dy**
C2–C2' (Å)	1.40(1)	n.a.	1.403(7)
Av. Dy–N (Å)	2.420(5)	2.471(4)	2.369(4)
Dy–Dy (Å)	6.425(1)	7.705(3)	6.060(1)
Av. Cnt–Dy–Cnt (°)	138.6(1)	138.6(1)	135.3(2)
Dy1–N1–N2–Dy2 (°)	16.8(7)	69.7(13)/ 69.4(13)	15.5(5)/ 22.8(5)
N1–Dy–N1' (°)	68.4(2)	n.a.	75.4(1)/ 75.6(1)

References

1 F. Benner and S. Demir, Isolation of the Elusive Bisbenzimidazole $Bbim^{3-\bullet}$ Radical Anion and its Employment in a Metal Complex, *Chem. Sci.*, 2022, **13**, 5818–5829.

2 S. Demir, J. M. Zadrozny, M. Nippe and J. R. Long, Exchange Coupling and Magnetic Blocking in Bipyrimidyl Radical-Bridged Dilanthanide Complexes, *J. Am. Chem. Soc.*, 2012, **134**, 18546–18549.

3 S. Demir, M. Nippe, M. I. Gonzalez and J. R. Long, Exchange Coupling and Magnetic Blocking in Dilanthanide Complexes Bridged by the Multi-electron Redox-active Ligand 2,3,5,6-tetra(2-pyridyl)pyrazine, *Chem. Sci.*, 2014, **5**, 4701–4711.